

UNIVERSITÀ DEGLI STUDI DI CATANIA

Ph.D. in Materials Science and Nanotechnology XXXI Cycle

Ph.D. Thesis

**Synthesis of hybrid metalorganic/inorganic
systems and doped halide thin films for
photovoltaics**

Ph.D. Student:

ANNA LUCIA PELLEGRINO

Supervisor:

Prof. Graziella Malandrino

Coordinator:

Prof. Maria Grazia Grimaldi

2016-2018

Contents

Introduction	4
1. Photovoltaic Materials	9
1.1 <u>Photovoltaic technology: state of art</u>	9
1.2 <u>Lanthanide doped fluoride thin films</u>	11
1.3 <u>Hybrid organic/inorganic systems</u>	19
1.4 <u>Inorganic halide perovskites</u>	21
References	24
2. MOCVD fabrication of Ln³⁺ doped fluoride thin films	32
2.1 <u>Introduction</u>	33
2.2 <u>Ln³⁺ doped CaF₂ thin films: MOCVD fabrication and their up- conversion properties</u>	34
2.2.1 Experimental Section	35
2.2.2 Results and discussion	36
2.2.3 Luminescent proprieties	43
2.3 <u>NaYF₄ thin film: MOCVD growth of cubic and hexagonal phases</u>	46
2.3.1 Experimental Section	46
2.3.2 Results and discussion	47
2.4 <u>KYF₄ thin films: MOCVD synthesis through a new β-dichetonate heterobimetallic potassium- yttrium precursor</u>	52
2.4.1 Experimental Section	52
2.4.2 Synthesis and characterization of a novel KY(hfa) ₄ •tetraglyme	53
2.4.3 KYF ₄ MOCVD synthesis: results and discussion	56
2.5 <u>Conclusion</u>	59

References	60
3. Sol-gel approach to the fabrication of Ln³⁺ doped fluoride thin films	63
3.1 <u>Introduction</u>	63
3.2 <u>Ln³⁺ doped β-NaYF₄ thin films: Sol-gel fabrications and their luminescent properties</u>	65
3.2.1 Experimental Section	66
3.2.2 Synthesis and characterization of a novel Na(hfa)•tetraglyme	67
3.2.3 Optimization of the sol-gel process for the formation of β-NaYF ₄ phase films	71
3.2.4 Co-doped Yb ³⁺ /Er ³⁺ and Yb ³⁺ /Tm ³⁺ β-NaYF ₄ phase thin films	77
3.2.5 Upconversion properties and luminescence lifetimes of the co-doped β-NaYF ₄ :Yb ³⁺ , Er ³⁺ and Yb ³⁺ , Tm ³⁺ films	80
3.3 <u>Ln³⁺ doped β-NaGdF₄ thin films</u>	85
3.3.1 Sol- gel process for the formation of β-NaGdF ₄ :Eu ³⁺ phase films	86
3.3.2 β-NaGdF ₄ :Eu ³⁺ thin films: analysis of phase stability vs annealing temperature	87
3.4 <u>Ln³⁺ doped YOF thin films</u>	89
3.4.1 Sol- gel process for the formation of YOF thin films	90
3.4.2 Structural, morphological and compositional characterization of Ln ³⁺ doped YOF thin films	91
3.5 <u>Conclusion</u>	94
References	95
4. Combined MOCVD/MLD approach for hybrid metalorganic-inorganic systems of NiO thin films with a luminescent europium complex monolayer	98
4.1 <u>Introduction</u>	98

4.2 <u>Experimental Section</u>	100
4.2.1 Precursors synthesis	100
4.2.2 MOCVD/MLD synthetic approach	101
4.3 <u>Results and discussion</u>	103
4.3.1 Monolayer characterization	104
4.3.2 Luminescent properties of the monolayer	109
4.4 <u>Conclusion</u>	111
References	111
5. Synthesis of inorganic perovskite CsPbBr₃: study of phase stability	113
5.1 <u>Introduction</u>	113
5.2 <u>Experimental section</u>	115
5.3 <u>Results and discussion</u>	115
5.4 <u>Conclusion</u>	122
References	123
Conclusions	124
Curriculum, publications and conferences	128

Introduction

The current energetic scenario has led the development of systems in which the renewable sources are economically competitive with "traditional" sources, reducing production costs and increasing conversion efficiencies. In this field, the photovoltaic approach is one of the most promising technologies, which allow to exploit the advantages of the solar source and to cover the electricity demand. Nowadays, several research fields are focused on the study of improving the performance of commercial photovoltaic modules through a more efficient exploitation of the solar spectrum. In this context, the aim of the present study is the development of new materials of interest for the photovoltaic (PV) technologies.

The most mature technology to date is based on silicon cells. The conversion efficiency of these solar cells varies from 6% for the amorphous Si up to 24.7% of prototypes obtained in the laboratory.

One possible way to increase the conversion efficiency of silicon solar cells is to shift the incident sunlight spectrum, converting photons poorly exploited by silicon into more effective photons. A better utilization of the solar spectrum can be obtained by converting photons with wavelengths higher or lower compared to the solar cell efficiency range into optimal wavelength range. The three conversion processes of interest are: up-conversion (UC), down-conversion (DC) and energy down-shifting. The materials studied as energy converters, consist of thin film layers integrated in the PV panel and made of two components: a host material and an active luminescent species that allows the conversion. In literature, the materials used as host matrices are polymeric composite layers, inorganic crystalline materials and various kind of glasses. The host material exhibits high transmission in the spectral region where the cell response is high and at the same time it guarantees an optimal environment for the luminescent component. The luminescent species used

in these layers represent the active centers of the energy conversion process. In particular, quantum dots and organic dyes are the most used species applied in PV devices together with ions and rare earth complexes due to their luminescent properties, which cover the ultraviolet (UV), visible and near infrared (NIR) range.

In the present thesis, the energy conversion systems made of lanthanide doped binary and multicomponent fluorides (CaF_2 , NaYF_4 , NaGdF_4 , KYF_4 and YOF) have been synthesized and deeply studied for their potential integration in silicon solar cells, due to the energy conversion processes of Ln ions. Starting from the β -diketonate metal complexes, two different synthetic approaches have been tested: metalorganic chemical vapor deposition (MOCVD) and sol-gel method.

Together with the traditional and well-known silicon PV technology, a new class of PV materials is subject of interest in the last years. In particular, the third generation solar cells represent the new technology with higher efficiency, based on inorganic multi-junction technology, new hybrid and inorganic semiconductor materials such as perovskite ABX_3 ($\text{A} = [(\text{CH}_3)\text{NH}_3]^+$ and Cs^+ ; $\text{B} = \text{Pb}^{2+}, \text{Sn}^{2+}$ and $\text{X} = \text{Cl}, \text{Br}, \text{I}$) and organic dye-sensitized solar cells (DSSC). In particular, the perovskite solar cells (PSCs) attract worldwide attention with always higher record in the power conversion efficiency and with the additional possibility of combining the advantages of mechanical, electrical, magnetic, optical, and transport properties. This recent generation of solar cell technology is of interest for industrial applications because of the advantages of low-cost, low-temperature processing, flexible substrates, and large-area fabrication processes.

In the present thesis, hybrid metalorganic/inorganic systems Eu-complex/ NiO have been synthesized for the DSSC technology and for the potential improvement of the PV material with new functionalities, that combine the semiconductor behavior of the inorganic part to the luminescent properties of the metalorganic component. Nickel oxide has been chosen as the inorganic component of the hybrid system due to its multifunctional properties such as electrochromic and antiferromagnetic properties, high dielectric constant, UV optical transparency and p-type

semiconducting behavior. Lanthanide complexes have been chosen due to their luminescent properties, in particular Eu complexes have attracted growing interest because Eu is one of the most efficient downshifter.

In addition, all-inorganic halide perovskite CsPbBr₃ has been synthesized through a precipitation method using Cs and Pb metal complexes and Br₂ as precipitating agent. The all-inorganic halide perovskite CsPbBr₃ has a semiconductor behavior, with an energy band gap useful in the PV application. Compared to the well-known hybrid perovskite, such as MAPbI₃ (MA: methyl ammonium), the CsPbBr₃ has the advantages to not have any labile or expensive organic components and shows remarkable stability under humidity conditions and extreme temperatures.

In summary, the present PhD thesis is organized in the following chapters and a schematic table (Table 1) is reported to summarize the materials object of the present study:

- Chapter 1 emphasizes the aim of the present study and the main photovoltaic technologies of importance in the recent years. An outlook regarding the materials of interest in the photovoltaic technology field has been described, together with the new strategies to increase the photovoltaic efficiency in solar cells.
- Chapter 2 focuses on the synthesis of CaF₂ films doped with Yb³⁺,Er³⁺ or Yb³⁺,Tm³⁺ through MOCVD route using a molten mixture consisting of the Ca(hfa)₂•diglyme•H₂O and the suitable Ln(hfa)₃•diglyme precursors in an appropriate stoichiometric ratio. In addition, MOCVD approach is applied to the fabrication of the multicomponent fluoride β-NaYF₄ and KYF₄ thin films as well. The fluorinated “third-generation” bimetallic precursors, NaY(hfa)₄tetraglyme, synthesized in a previous work, and the novel KY(hfa)₄tetraglyme, have been the starting point. These final goals have been

achieved through an accurate optimization of the operative parameters, such as deposition temperature, vaporization temperature of the precursors and choice of the substrates.

- Chapter 3 concentrates on an innovative sol-gel process to produce Ln³⁺doped β-NaREF₄ thin films (Ln: Eu³⁺, Yb³⁺, Tm³⁺, Er³⁺ and RE: Gd, Y), using a mixture of a novel β-diketonate sodium precursor Na(hfa)•tetraglyme and a rare earth precursors RE(hfa)₃•diglyme (RE=Y, Gd, Eu, Yb, Tm, Er). Furthermore, the sol gel method has been successful applied for the synthesis of Ln³⁺ doped r-YOF thin films as well. These final goals have been achieved through an accurate optimization of the operative parameters, such as effects of molar ratio of the precursors, aging time of sol and annealing treatment. Their structural and morphological properties are studied in details.
- Chapter 4 highlights a novel full vapor phase approach applied for the synthesis of hybrid metalorganic/inorganic systems. The process is based on the sequential steps of MOCVD of the inorganic NiO thin films and molecular layer deposition (MLD) to link on the activated surface in a covalent way a luminescent Eu(III) complex. An accurate X-ray photoelectron characterization confirmed the optimal parameter condition of the activation step and of the covalent anchoring of the Eu complex on NiO films.
- Chapter 5 reports the successful fabrication of the all-inorganic halide perovskite CsPbBr₃ using the β-diketonate complexes [Pb(hfa)₂diglyme]₂, Cs(hfa) through a precipitation method in ethanol and water solution with Br₂. The control of temperature and aging time for the formation of the pure phase CsPbBr₃ crystals has been deeply investigated.

PHOTOVOLTAIC MATERIALS OF INTEREST					
PV TECHNOLOGY		MATERIAL	PRECURSORS	METHOD	CHAPTER
Energy conversion systems for silicon solar cells	Lanthanide doped binary and multi-component fluorides	CaF₂: Yb³⁺, Er³⁺ / Yb³⁺, Tm³⁺	Ca(hfa) ₂ •diglyme•H ₂ O Ln(hfa) ₃ •diglyme	MOCVD	2.2
		β-NaYF₄	NaY(hfa) ₄ tetraglyme	MOCVD	2.3
		β-NaYF₄: Yb³⁺, Er³⁺ / Yb³⁺, Tm³⁺	Na(hfa)•tetraglyme RE(hfa) ₃ •diglyme (RE=Y, Yb, Tm, Er)	Sol-gel	3.2
		NaGdF₄: Eu³⁺	Na(hfa)•tetraglyme RE(hfa) ₃ •diglyme (RE=Gd, Eu)	Sol-gel	3.3
		KYF₄	KY(hfa) ₄ tetraglyme	MOCVD	2.4
		YOF: Yb³⁺, Er³⁺ / Yb³⁺, Tm³⁺	Y(hfa) ₃ •diglyme Ln(hfa) ₃ •diglyme (Ln: Yb, Tm, Er)	Sol-gel	3.4
Dye-sensitized solar cells	Hybrid metalorganic/inorganic systems	Eu-complex/NiO	Eu(hfa) ₃ phen	MLD	4
Perovskite solar cells	Inorganic halide perovskite	CsPbBr₃	[Pb(hfa) ₂ diglyme] ₂ Cs(hfa)	precipitation method	5

Table 1 Overview of materials synthesized in the present PhD thesis.

CHAPTER 1

Photovoltaic Materials

1.1 Photovoltaic technology: state of art

A photovoltaic system has the property of absorbing photons and generating electrons for electrical conduction. In recent years, the evolution of solar cells, due to technological and economic progress, has developed through the growing of three different photovoltaic generations.

The first generation solar cells are relatively expensive to produce, and have a low efficiency in relation to production costs. The first generation includes single-junction devices made of crystalline silicon (mono and multi-crystalline), which converts directly solar radiation into electrical energy. This kind of cells has two doped silicon layers in order to obtain a p-n junction. This technology achieves a conversion efficiency around 25% for based c-Si cells and about 20% for mc-Si cells.

The second generation is characterized by lower yield than the previous ones but has lower production cost. This technology is based on the production of Si thin film cells, with thickness between 1 and 10 μ m, which yields flexibility properties. However, this kind of cell has slightly lower efficiency with respect to the previous generation. Another aspect of this second generation technology is the use of new materials such as amorphous silicon (a-Si), and composite materials such as indium-copper-gallium diselenide (CuIn(Ga)Se₂ or CIGS) or cadmium telluride (CdTe).

The third generation solar cells represents the new technology and has the higher efficiency, and can be divided into two categories:

- inorganic cells, which use semiconductor materials such as the previous ones and the hybrid or inorganic perovskites ABX_3 ($A = [(CH_3)NH_3]^+$ and Cs^+ ; $B = Pb^{2+}, Sn^{2+}$ and $X = Cl, Br, I$);
- organic cells, which use polymers or organic dyes.

The inorganic third generation cells are based on multi-junction technology, using up to four overlapping cells of semiconducting materials in tandem configuration, and currently show the highest efficiency values. Very recently the new organic–inorganic hybrid halide perovskite materials have become promising candidates for efficient inorganic third generation solar cells.

The organic third generation cells, known as Dye Sensitized solar cells (DSSC), have the advantages of the organic materials in terms of very low costs of material and production, due to the easy processing through deposition on transparent, flexible and large area substrates. However, currently the highest efficiency for this kind of cells is around 11% and they present limits regarding their duration.

In this scenario, an interesting perspective is the possibility to increase the efficiency of a photovoltaic cell, independently on its nature, by collecting the radiation energy outside the absorption range of the photoactive material by shifting its energy to a more suitable optical region through down-conversion (DC) or up-conversion (UC) processes. Down-conversion is the process by which one high energy photon, which is inefficiently absorbed by the photovoltaic cell due to thermalisation losses, is converted into two or more lower energy photons. The DC layer is placed in front of the cell and the generated photons all have sufficient energy to be absorbed by the photovoltaic cell, with negligible thermalisation loss. Up-conversion is the process by which two or more low energy (long wavelength) photons, which are transmitted by the photovoltaic cell, are converted into one high energy photon. Thus an UC layer placed behind a PV device can harvest the solar radiation energy outside the PV absorption range and convert it into useful photons with energy inside the band of the semiconductor used in the PV device.

The aim of the present study is the development of new materials of interest for the photovoltaic technologies. Lanthanide doped fluoride materials CaF_2 , NaYF_4 , NaGdF_4 , KYF_4 and YOF have been synthesized and deeply studied for the possibilities of increasing the efficiency yield in the a-Si and mc-Si cells, due to the energy conversion processes of Ln ions. These systems in fact, could enhance the photovoltaic efficiency and could be easily integrated in the PV panel.

The hybrid metalorganic/inorganic systems Eu-complex/ NiO has been synthesized for the DSSC technology and for the potential improvement of the PV material with new functionalities, that combine the semiconductor behavior of the inorganic component to the properties of the organic component.

Finally, the inorganic halide perovskite CsPbBr_3 has been synthesized through a precipitation method. The all-inorganic halide perovskite CsPbBr_3 shows a semiconductor behavior, with an energy band gap useful in the PV application of the new third generation perovskite solar cells.

1.2 Lanthanide doped fluoride thin films

In the last years, much attention has been focused on luminescent rare-earth (RE)-doped materials, for their large variety of modern technological applications, ranging from phosphors [1-2] to solar cells [3], from flat-panel displays [4], to solid state lasers [5], from photocatalysis [6], to diagnostic tools in nanobiomedicine [7]. Very recently lanthanide doped materials have been proven also interesting in form of homogenous films for microelectronics applications, to map the temperature distribution inside integrated circuits in non-contact mode and with high spatial resolution, using the different luminescent emission of the lanthanides at different temperatures [8]. Lanthanide doped fluoride materials have been deeply studied for their unique properties in the ultraviolet, visible and IR range. In fact, a proper combination of doping ions and host material produces an efficient energy conversion mechanism upon light irradiation [9]. In particular, ternary fluoride

compounds, like the NaYF_4 , NaGdF_4 and KYF_4 and binary fluoride MF_2 (M: Ca, Sr), have been thoroughly studied as host materials for doping luminescent Ln^{3+} (Ln = lanthanide) ions to achieve the desirable down-conversion (DC) or up-conversion (UC) processes [10].

In particular, UC is a process whereby two or more low energy photons are converted into higher energy photons, and DC, on the contrary, is a process in which higher photons are converted into more photons with lower energy. These forms of spectral conversion have been considered as a provision in the area of photovoltaics (PV) [11], to reduce the intrinsic losses associated with the transmission of sub-bandgap photons (fig. 1) [12]. In fact, as shown in fig. 1, down-conversion shifts photons from a high-energy band (blue) to the maximum absorption band of silicon (white); up-conversion shifts photons from a low-energy band (red) to the maximum absorption band of silicon [13, 14].

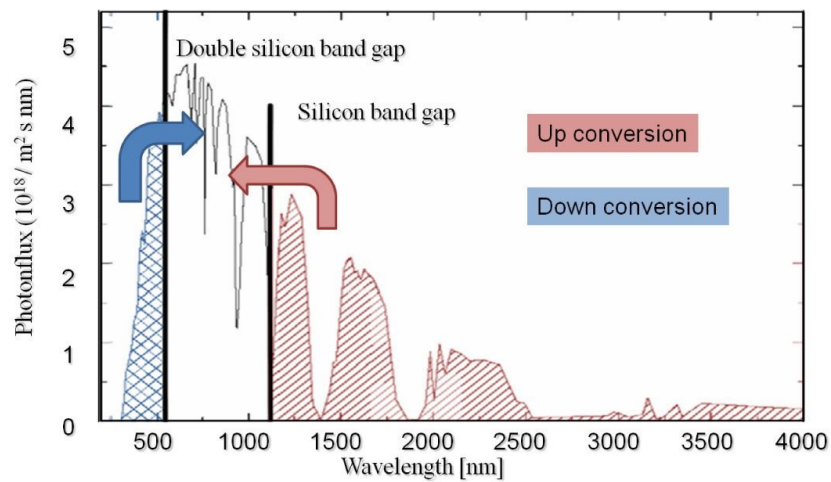


Fig. 1 Solar spectrum showing the band gap and twice the band gap of silicon and the UC and DC shifting [13].

Several mechanisms, originated from transitions within the 4f configuration of Ln-doped nanomaterials, are known to guide the energy conversion emissions.

The DC mechanism is the process where one photon with a high energy is cut to obtain two photons with a lower energy. Cutting of one high energy photon to obtain two lower energy photons on a single lanthanide ion is known as cascade emission (fig. 2a) and has been known to occur for Pr^{3+} [15], Tm^{3+} [16] and Gd^{3+} [17]. Down-conversion with pairs of lanthanide ions can occur through various mechanism, shown in fig. 2b, c, d. For all three mechanisms ion I is first excited into a high energy level. Figure 2b shows the emission of two photons from ion pairs via cross-relaxation between ions I and II followed by energy transfer from ion I to ion II and emission from ion II. Figures 2c, d show mechanisms involving on energy transfer step between ions I and II, and emission of a photon by both ions.

UC is the process where two photons with a smaller energy are added up to obtain one photon with a high energy. Figure 3 gives an overview of the possible up-conversion mechanisms. The most efficient process is the mechanism called Energy Transfer Up-conversion (ETU), in which two ions of type I absorb a photon and give the energy to ion II in two steps via an intermediate level on ion I (fig. 3a). This can also be described as ground state absorption (GSA) followed by an energy transfer step, known as GSA/ETU. Up-conversion on a single ion (fig. 3b) can occur when the ion is already in the excited state and a second photon is absorbed. This mechanism is known as GSA followed by excited state absorption (ESA), and it is the second most efficient mechanism. For UC with these two mechanisms it is necessary that the second excitation step of ion I is faster than both the radiative and non-radiative decay from the intermediate level. Both of these mechanisms involve real intermediate energy levels. The other four mechanisms shown in fig. 3c-f involve one or more virtual energy levels, and therefore have lower efficiencies.

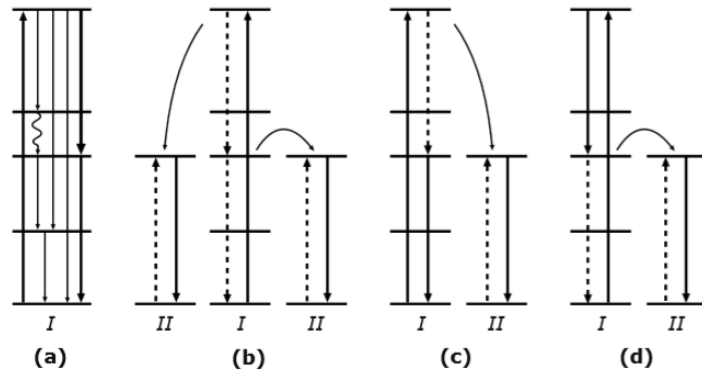


Fig. 2 Schematic representation of several different down conversion mechanisms. Solid vertical arrows indicate radiative transitions. Arrows connecting different ions and dashed arrows indicate energy transfer between ions.

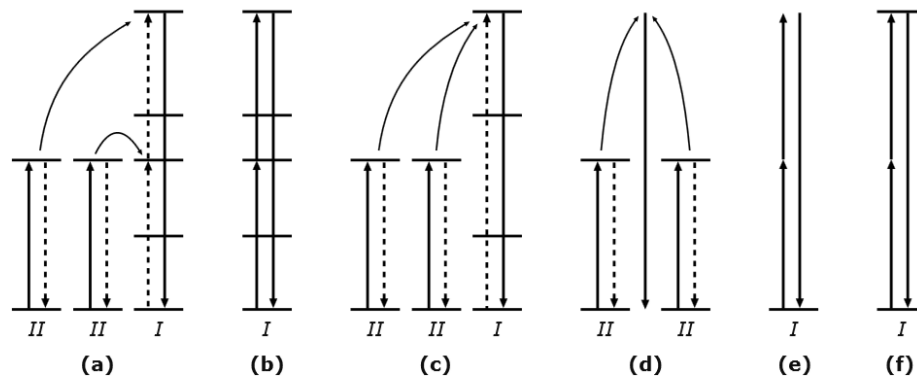


Fig. 3 Energy level schemes for several different 2-photon up-conversion mechanisms. Solid vertical arrows indicate radiative transitions. Arrows connecting different ions and dashed arrows indicate energy transfer between ions [18].

The energy transfer up-conversion (ETU) is the most efficient processes for $\text{Yb}^{3+}/\text{Ln}^{3+}$ co-doped fluoride. Trivalent lanthanide ions, like Er^{3+} , Tm^{3+} , Nd^{3+} or Ho^{3+} , are the most common activator ions for the ETU process due to their peculiar energy level schemes and narrow emission spectral lines, and the Yb^{3+} ion is the useful sensitizer with a large absorption in the IR range [19].

In regard to the host material, fluorescent fluoride hosts, in comparison with conventional oxide luminescent systems, are attractive because of their high optical

transparency from UV through IR, high chemical stability, high refractive index and low phonon energy, which enables the radiative transitions of lanthanide ions to occur with high efficiency [20].

CaF₂

Calcium fluoride has the typical fluorite structure, following the name (fluorite) of the mineral form of CaF₂, which is a simple cubic arrangement of anions with 50% cubic sites filled with Ca²⁺ (fig. 4). Thus, in this structure, calcium is eight coordinated by fluoride ions, a coordination environment suitable for the lanthanide ions, being eight the most common coordination number for lanthanides [21].

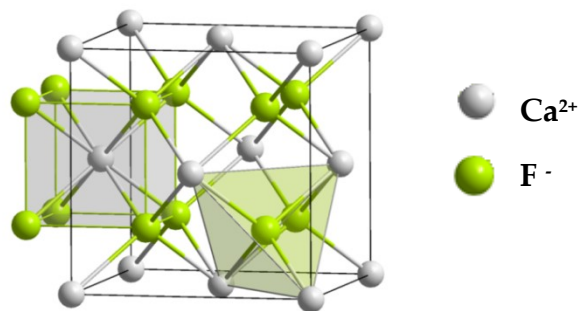


Fig. 4 Fluorite structure.

Most of the above-mentioned applications require the calcium fluoride material in the form of thin films. Several studies are available on the deposition of CaF₂ thin films using physical vapor deposition techniques, such as sputtering [22], electron beam evaporation [23], pulsed laser deposition [24], and molecular beam epitaxy [25]. Calcium fluoride films have also been deposited through sol-gel chemical routes using spin coating or dip coating [26]. Among the chemical vapor deposition approaches, atomic layer deposition has been applied to the deposition of CaF₂ films [27]. Nevertheless, even though various deposition methods have been applied to the

fabrication of CaF₂ films, a more versatile, easily scalable, fast, and industrially appealing approach is highly desirable [28].

MOCVD has been also applied to the deposition of the fluorite films; nevertheless, most of these reports used a fluorine-free calcium source, thus a second precursor is needed as the fluorine source. The first report on the deposition of CaF₂ with MOCVD dates back to 1989 when the bis(pentamethyl-cyclopentadienyl)calcium was applied as calcium source together with SiF₄ or NF₃ as fluorine source [29]. More recently, fluorine free β -diketonate has been applied as calcium source combined with the use of ammonium hydrogen fluoride as the fluorine source [30]. A few reports are described in the application of fluorinated precursors to the fabrication of thin films where polyether adducts of the Ca bis-hexafluoroacetylacetonate have been applied, namely, the Ca(hfa)₂•tetraglyme [31] and the Ca(hfa)₂•diglyme•H₂O [32].

NaREF₄

The crystal structure of NaREF₄ exhibits two polymorphic forms, namely, cubic (α) and hexagonal (β) phases (fig. 5). The cubic α -NaYF₄ structure is isostructural to fluorite. The hexagonal β -NaYF₄ structure, of interest in this work due to its efficient host behavior, presents instead a distribution of cations in the lattice controversial [33]. The X-ray diffraction patterns of this phase do not fit well the crystalline structure, reported for the known NaNdF₄ [33]. The Na:M ratio (M = Y, Nd, Er, Tm, Yb) of the hexagonal phase deviates from the expected 1: 1 value, and it depends on the M species and the preparation temperature. Therefore, it is proposed that the β -NaYF₄ phase is isostructural with chloride phases of Na_{3x}M_{2-x}Cl₆ stoichiometry (M = La - Sm). This structure, characteristic of gagarinite, contains only one M³⁺ site which is occupied by Na⁺ and M³⁺ ions in non-stoichiometric ratios with the final formula Na_{3x}M_{2-x}F₆ (x = 0.45 - 0,5). Therefore, the hexagonal phase is known as Na_{1.5}Y_{1.5}F₆ as well [34].

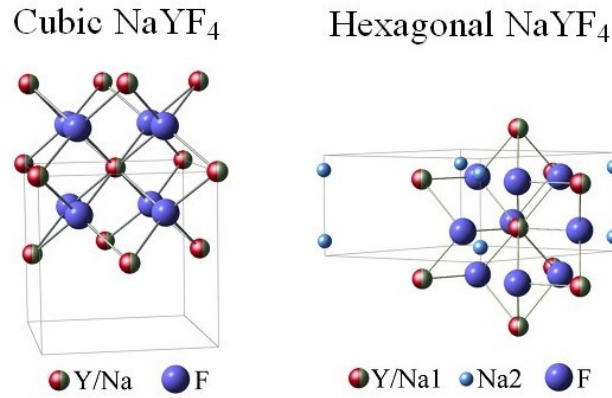


Fig. 5 Cubic (α) and hexagonal (β) phases of NaYF_4 crystal structure.

Several investigations have shown that the hexagonal phase is a much better host lattice than the cubic one for energy conversion applications [35]. Therefore, an accurate control for the selective and reproducible fabrication of the β - $\text{NaREF}_4:\text{Ln}^{3+}$ single phase is a stringent requirement for high energy conversion performance. At the same time, a controlled dispersion of the luminescent Ln species in the host matrices plays a key role, since the local environment around the luminescent ions strongly affects the emission performances of the materials [36]. Until now, several methods have been employed to obtain Ln doped β - NaREF_4 nanocrystals, including co-precipitation [37], solvothermal [38], thermal evaporation [39], and molten salt method [40]. Recently, few studies have been reported on the fabrication of complex core-shell architectures and their up-conversion performances [41]. Only a few reports are available, to the best of our knowledge, about NaYF_4 thin films and the study of their energy conversion properties [42].

YOF

Oxyfluorides' crystal structures (YOF and LaOF) exhibit three different crystal lattices: cubic, rhombohedral and tetragonal, which is usually nonstoichiometric ($\text{REO}_n\text{F}_{3-2}$, $0.7 < n < 1$) [43]. The rhombohedral structure (r-YOF) is the stable one, and it

is strictly stoichiometric ($n=1$) (fig. 6). The cubic YOF structure occurs as the result of the phase transition from the rhombohedral phase at temperature of 560–570°C [44]. Tetragonal crystal form has been observed usually in nonstoichiometric compounds, but additional studies have shown that these materials are more complex than it was previously assumed; for example compound with general formula $RE_nO_{n-1}F_{n+2}$, $5 \leq n \leq 9$ such as $Y_5O_4F_7$, $Y_6O_5F_8$ and $Y_7O_6F_9$, which crystallize in an orthorhombic form [45-47].

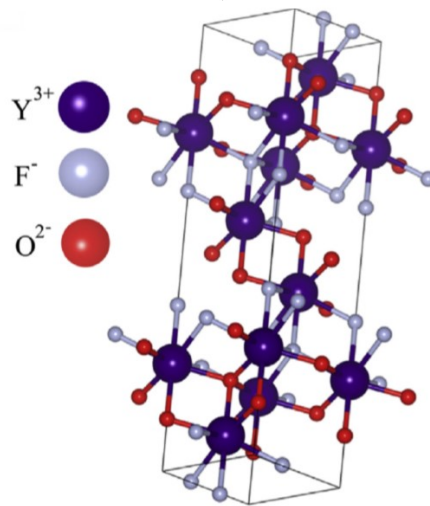


Fig. 6 Rhombohedral structure of YOF.

Lanthanide doped oxyfluorides have been a matter of interest for their utilization in many important technologies, such as lasers, electronics, therapeutics, displays, solar cells, catalysis, medicine [48–51]. In addition, there is a growing interest for their use as bio-markers or nano-sensors [52]. These materials are promising hosts for preparation of phosphors due to their attractive chemical and physical properties which may be classified as in between characteristics of fluorides and oxides [44,53]. Alike fluorides, oxyfluorides have low phonon energy and high ionicity which leads to the efficient luminescence, while, on the other hand, these compounds have great

chemical and thermal stabilities which resemble properties of oxides [48,49]. In addition, oxyfluoride nanomaterials are biocompatible and nearly nontoxic to live cells so they can be used for biomedical applications [51,54].

To prepare oxyfluorides, several methods can be employed: thermolysis method, fluorolytic sol-gel, hydrothermal method, co-precipitation method, solid state synthesis [50,55]. To our knowledge, only one study has been reported on the synthesis of YOF thin film [56].

1.3 Hybrid organic/inorganic systems

Nowadays the organic-inorganic hybrid systems made of inorganic thin film with surfaces functionalized by covalent attachment of organic molecules have attracted great attention because of their potential applications in several fields of material science [57–58] such as sensors [59], dye sensitized solar cells (DSSCs) [60], optoelectronic devices [61], and heterogeneous catalysis [62]. In these systems, transition metal oxides thin films are the most promising inorganic materials [63], due to their wide spectrum of magnetic, electrical, and optical properties [64]. In this context the anchoring of organic luminescent complexes on the oxide surface [65] leads to a new multifunctional materials with a wide range of modular properties [66], and therefore a broad range of applications [67].

Among transition metal oxides, nickel oxide has been chosen as the inorganic component of the hybrid system due to its multifunctional properties such as high dielectric constant, low resistivity and UV optical transparency [68]. Nickel oxide has also electrochromic and antiferromagnetic properties and a p-type semiconducting behavior. For these wide range of properties NiO has been studied as material for organic light-emitting diodes (OLED) [69], tandem photocathodes for dye-sensitized solar cells (DSSC) [70], smart windows [71], Schottky devices [72], and chemical sensors [73].

In regard to the synthesis approach for NiO thin films many methods have been reported in the literature such as thermal evaporation [74], pulsed-laser-deposition (PLD) [75], reactive magnetron sputtering [76], metal organic chemical vapor deposition (MOCVD) [77], intermittent spray pyrolysis [78] and sol-gel deposition [79]. Among these strategies, MOCVD has been chosen in this work as synthetic method because of its reliable and reproducible production in large scale and highly uniformity in thickness and composition.

In relation with the nature of inorganic film, the most common functional organic moieties chosen for the hybrid approach are the molecules having silane [80], thiol [81], and carboxylic functionalities [82] as anchoring groups. As alternatives, also organophosphorus compounds were tested as linkers for the functionalization of metal oxide surfaces [83]. Among these wide families of functional molecules the attention has been devoted to luminescent lanthanide complexes due to the exceptional photophysical properties such as high quantum yields, long excited-state lifetimes, large Stokes shifts and sharp emission profiles related to f-f electronic transitions. Eu(III) complexes have attracted growing interest as efficient downshifter, probe to sense the chemical environment and for its luminescent behavior.

For a variety of applications, the possibility of a fast, high efficient and reproducible assembly method of molecules into nanostructured solid substrates is of a great importance. Up to date, most of the synthetic approach to prepare hybrid systems have applied solution routes such as sol-gel procedure [84], Langmuir-Blodgett techniques, self-assembly procedures and gas-phase route such as atomic layer deposition, and very recent molecular layer deposition [85].

Molecular layer deposition is a solvent free method to create conformal coating organic molecular layers with self-limiting reactions on the surface and an excellent molecular-level control of thickness and composition [86].

Recently, organic-inorganic hybrid systems were reported by E. Smecca et al. [87]. They applied a multistep process with the NiO surface activated by Ar⁺ ions sputter

process and functionalized using a solution route with a phosphonic linker, followed by the coordination of the $\text{Eu}(\text{tta})_3\text{phen}$ ($\text{tta} = 2\text{-thenoyltrifluoroacetato}$), (fig. 7) to form the self-assembled monolayer.

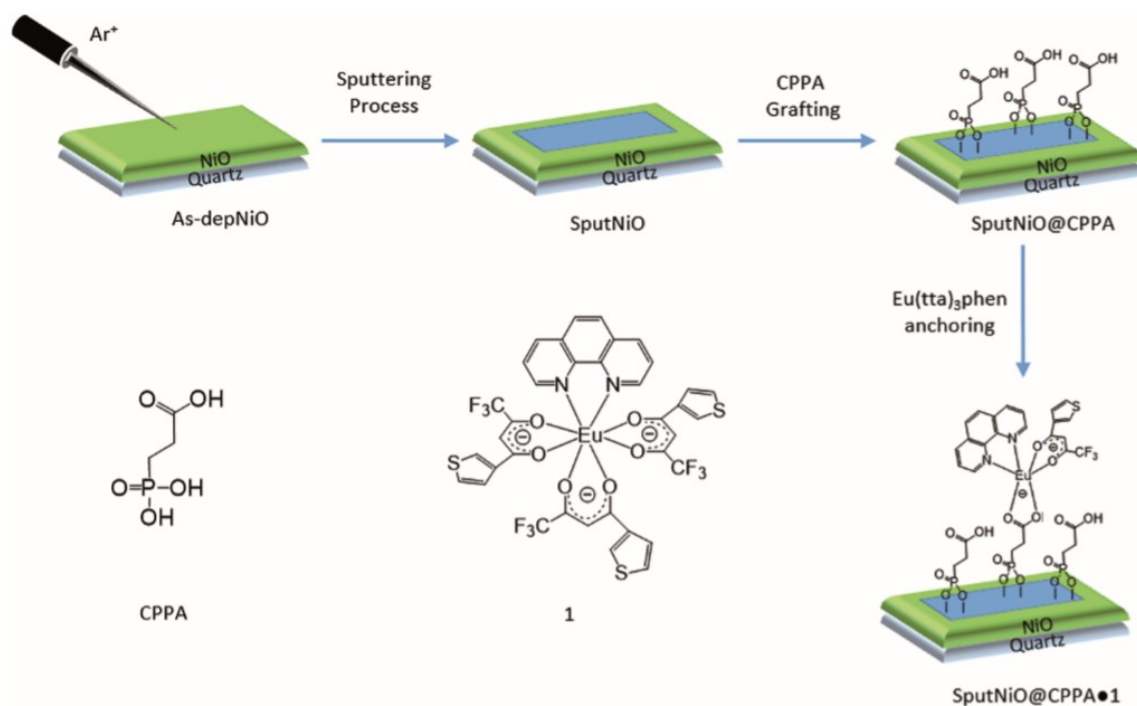


Fig. 7 Grafting steps and compounds used for the preparation of functionalized NiO in ref. [87].

1.4 Inorganic halide perovskite

The compounds belonging to the family of perovskites show a variety of mechanical, electrical, magnetic, optical, and transport properties [88-91], and for these reasons are nowadays key materials for many technologies. A few examples include piezoelectrics [88], photovoltaic absorbers [89], and multiferroic magnetoelectrics [90]. In the last years, inorganic halide perovskite and organic-inorganic halide perovskite materials (e.g., MAPbI_3 , FAPbI_3 , etc.; where $\text{MA} = \text{CH}_3\text{NH}_3^+$, $\text{FA} = \text{CH}(\text{NH}_2)^{2+}$) have been studied intensively for photovoltaic applications. Since the first demonstration of their use in solar cells [92], the research field on perovskite

solar cells (PSCs) attracts worldwide attention, as shown by a rapid increase in the number of publications [93], and together with a record in the power conversion efficiency. In fact, the power conversion efficiencies of perovskite solar cells have exhibited an increase and has reached the highest value of 22.1% [94]. For these reasons, perovskite solar cells are considered the most promising candidate for the next generation solar cell technology with low-cost, low-temperature processing, flexible substrates, and large-area fabrication processes [95-96].

An ideal perovskite lattice structure with formula ABX_3 has the simple cubic crystal structure of $CaTiO_3$, consists of octahedrons of X anions with B cations in their center, and A cations occupying the 12-fold coordinated site located in the middle of the cube constituted by eight octahedra (fig. 8). However, this cubic structure is rather uncommon, and many distorted variants are observed in natural and synthetic materials. The reason for the large range of possible compositions and material properties is due to the fact that the perovskite crystal structure is able to accommodate atoms A, B, and X of different sizes and with different oxidation states.

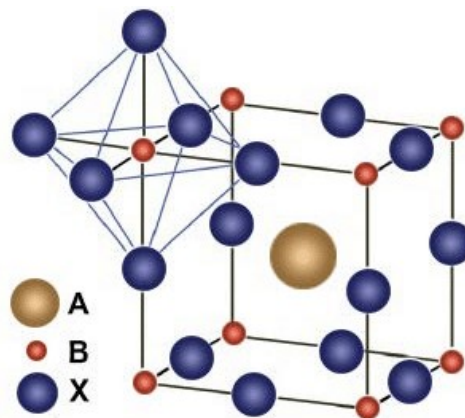


Fig. 8 Perovskite structure.

Highly efficient perovskite solar cells are composed of a structure with an organic/inorganic monovalent cation, A = methylammonium MA: $CH_3NH_3^+$; formamidinium FA: $CH(NH_2)_2^+$, Cs^+ , Rb^+ ; a divalent metal cation, B = Pb^{2+} , Sn^{2+} ; and

an halide anion $X = I^-; Br^-; Cl^-$. In 2012, Kim et al. [97] reported the introduction of an all solid-state lead-based perovskite such as $CH_3NH_3PbI_3$ Methylammonium lead iodide (MAPbI₃). Since then, the study of perovskite solar cells has been increasing and higher and higher energy conversion efficiency records are being reported [98]. These hybrid lead-based materials have excellent properties and contain elements that are both cheap and abundant. However, the presence of lead leads to several problems due to its toxicity, and they tend to partially decompose when exposed to air, water, ultra-violet light, or heat [99]. For these reasons, several substitutions have been attempted to improve the properties and performances of these material. For example lead in MAPbI₃ has been successfully replaced by Sn, and I⁻ by other combination of halide ions [98-100]. Another route to improve the stability of PSCs is to explore novel perovskite materials and find alternatives to replace organic component. In this field, there was a growing development of all-inorganic PSCs by excluding the organic species sensitive to the ambient environment. The all-inorganic PSCs do not have any labile or expensive components and show remarkable stability under high-humidity conditions (90–95% relative humidity, 25 °C) and extreme temperatures (100 or -22 °C) even without encapsulation, and therefore, the instability of traditional hybrid PSCs can be avoided [101]. Unlike the hybrid PSCs, the entire fabrication process of all-inorganic PSCs can be operated in ambient atmosphere without humidity control. Recently, Akbulatov et al. [102] in their work report a study on thermal and photochemical degradation of a series of systems APbX₃ ($X = I, Br$) with hybrid organic ($A^+ = CH_3NH_3$) and inorganic ($A^+ = Cs^+$) cations under anoxic conditions. They show that the hybrid materials are intrinsically unstable with respect to the heat- and light-induced stress and, therefore, can hardly sustain the real solar cell operation conditions. On the contrary, the cesium-based all-inorganic complex CsPbX₃ lead halides show superior stability and, therefore, potentially achieve the creation of highly efficient and stable perovskite solar cells, also considering that no degradation products with lead are present after the tests.

References

- [1] Y.Cho, S.W. Song, S.Y. Lim, J.H. Kim, C.Park, H.M. Kim, *Phys. Chem. Chem. Phys.*, 2017, 19, 7326-7332.
- [2] M. Back, R. Marin, M. Franceschin, N. Sfar Hancha, F. Enrichi, E. Trave, S. Polizzi, *J. Mater. Chem. C*, 2016, 4, 1906-1913.
- [3] a) Y. Mei, X. Ma, Y. Fan, Z. Bai, F. Cheng, Y. Hu, Q. Fan, S. Chen, W. Huang, *J. Nanosci. Nanotechnol.*, 2016, 16, 73807387; b) H. Jia, Z. Chen, P. Chen, C. Xu, C. Liu, Z. Zhao, X. Liu, J. Qiu, *J. Am. Ceram.Soc.*, 2017, 100, 697-704; c) Y. Li, K. Pan, G. Wang, B. Jiang, C. Tian, W. Zhou, Y. Qu, S. Liu, L. Feng, H. Fu, *Dalton Trans.*, 2013, 42, 7971-7979.
- [4] K. N. K. B. Adusumalli, M. V. S. R. M. Koppiseti, V. Mahalingam, *J. Mater. Chem. C*, 2016, 4, 2289-2294.
- [5] L.M. Jin, X. Chen, C.K. Siu, F. Wang, S.F. Yu, *ACS Nano*, 2017, 11, 843-849.
- [6] X. Guo, W. Di, C. Chen, C. Liu, X. Wang, W. Qin, *Dalton Trans.*, 2014, 43(3), 1048-1054.
- [7] I.X. Cantarelli, M. Pedroni, F. Piccinelli, P.Marzola, F. Boschi, G.Conti, A. Sbarbati, P. Bernardi, E.Mosconi, L. Perbellini, L. Marongiu, M. Donini, S.Dusi, L. Sorace, C. Innocenti, E. Fantechi, C. Sangregorio, A. Speghini, *Biomater Sci-Uk*, 2014, 2, 1158-1171.
- [8] a) D. Jaque and F. Vetrone, *Nanoscale*, 2012,4, 4301-4326; b) M.Quintanilla, I.X. Cantarelli, M. Pedroni, A. Speghini, F.Vetrone, *J. Mater. Chem. C*, 2015, 3, 3108-3113; c) M. Quintanilla, L. M. Liz-Marzána, *Nanotoday*, 2018, 19, 126145.
- [9] A. L. Pellegrino, P. Cortelletti, M. Pedroni, A. Speghini, G. Malandrino, *Adv. Mater. Interfaces*, 2017, 4(18), 1700245/11700245-6.
- [10] B. del Rosal, A. Perez-Delgado, M. Misiak, A. Bednarkiewicz, A. S. Vanetsev, Y. Orlovskii, D. J. Jovanovic, M.D. Dramicanin, U.Rocha, K. Upendra Kumar, C. Jacinto, E.Navarro, E. M. Rodriguez, M. Pedroni, A. Speghini, G. A. Hirata, I. R. Martín, and D. Jaque, *J. Appl. Phys.*, 2015, 118, 143104-143111.

- [11] a) P. Gibart, F. Auzel, J.-C. Guillaume, and K. Zahraman, *Jpn. J. Appl. Phys.*, 1996, 35, 4401–4402; b) J. C. Goldschmidt, and S. Fischer, *Adv. Opt. Mater.*, 2015, 3, 510-535.
- [12] W. Shockley and H. J. Queisser, *J. Appl. Phys.*, 1961, 32, 510– 519.
- [13] G. Alombert-Goget, D. Ristic, A. Chiasera, S. Varas, M. Ferrari, G.C. Righini, B. Dieudonne and B. Boulard, *SPIE Newsroom - Solar & Alternative Energy*, 2011. DOI: 10.1117/2.1201105.003701
- [14] H. Jia, Z. Chen, P. Chen, C. Xu, C. Liu, Z. Zhao, X. Liu, J. Qiu, *J. Am. Ceram. Soc.*, 2017, 100(2), 697-704.
- [15] W. Piper, J. DeLuca, and F. Ham, *J. Lumin.* 1974, 8, 344.
- [16] R. Rappalardo, *J. Lumin.*, 1976, 14, 159.
- [17] R. Wegh, H. Donker, A. Meijerink, R. Lamminmäki, and J. Hölsä, *Phys. Rev. B.* 1997, 56, 13841.
- [18] F. Auzel, *J. Lumin.*, 1990, 45, 341.
- [19] F. Auzel, *Chem. Rev.*, 2004, 104, 139–174.
- [20] a) D. Lu, C. Mao, S.K. Cho, S. Ahn, W. Park, *Scientific Reports*, 2016, 6, 18894 1-11; b) L.T.K. Giang, L. Marciniak, D. Hreniak, T.K. Anh, L.Q. Minh, *J. Electr. Mater.*, 2016, 45, 4790-4795; c) V. N. K. B Adusumalli, H. V. S. R. Koppiseti, S. Ganguli, S. Sarkar, V. Mahalingam, *Chemistry - A European Journal*, 2017, 23, 994-1000.
- [21] G. Malandrino, I. L. Fragalà, *Coord. Chem. Rev.* 2006, 250, 1605.
- [22] N. J. Dudley, *J. Vac. Sci. Technol.*, A 1998, 16, 615.
- [23] R. K. Pandey, M. Kumar, S. A. Khan, T. Kumar, A. Tripathi, D. K. Avasthi, A. C. Pandey, *Appl. Surf. Sci.* 2014, 289, 77.
- [24] A. De Bonis, A. Santagata, A. Galasso, M. Sansone, R. Teghil, *Appl. Surf. Sci.* 2014, 302, 145.
- [25] C. Deiter, M. Bierkandt, A. Klust, C. Kumpf, Y. Su, O. Bunk, R. Feidenhans'l, J. Wollschläger, *Phys. Rev. B* 2010, 82, 085449.
- [26] T. Jiang, W. Qin, F. Ding, *J. Nanosci. Nanotechnol.* 2010, 10, 2013.

- [27] a) M. Ylilampi, T. Ranta-aho, *J. Electrochem. Soc.* 1994, 141, 1278; b) T. Pilvi, K. Arstila, M. Leskela, M. Ritala, *Chem. Mater.* 2007, 19, 3387.
- [28] F. Meillaud, M. Boccard, G. Bugnon, M. Despeisse, S. Hänni, F.-J. Haug, J. Persoz, J.-W. Schüttauf, M. Stuckelberger, C. Ballif, *Mater. Today* 2015, 18, 378.
- [29] M. J. Benac, A. H. Cowley, R. A. Jones, A. F. Tasch Jr., *Chem. Mater.* 1989, 1, 289.
- [30] A. V. Blednov, O. Yu Gorbenko, S. V. Samoilenkov, V. A. Amelichev, V. A. Lebedev, K. S. Napol'skii, A. R. Kaul, *Chem. Mater.* 2010, 22, 175.
- [31] G. Malandrino, F. Castelli, I. L. Fragala', *Inorg. Chim. Acta* 1994, 224, 203.
- [32] A. M. Makarevich, P. P. Semyannikov, N. P. Kuzmina, *Russian J. Inorg. Chem.* 2010, 55, 1940.
- [33] K. W. Kramer, D. Biner, G. Frei, H. U. Gudel, M. P. Hehlen, S. R. Luthi, *Chem. Mater.*, 2004, 16, 1244-1251.
- [34] J.H. Burns, *Inorg. Chem.*, 1965, 4, 881.
- [35] H. Liu, J. Han, C. McBean, C.S. Lewis, P. Kumar Routh, M. Cotlet, S.S. Wong, *Phys. Chem. Chem. Phys.*, 2017, 19, 21532167.
- [36] L. Armelao, G. Bottaro, M. Pascolini, M. Sessolo, E. Tondello, M. Bettinelli, A. Speghini, *J. Phys. Chem. C*, 2008, 112, 40494054.
- [37] a) C.Cao, X. Zhang, M. Chen, W. Qin, J. Zhang, *J. Alloy Compd.*, 2010, 505 ,6-10; b) W. Yu, W. Xu, H. Song, S. Zhang, *Dalton Trans.*, 2014, 43(16), 6139-6147.
- [38] M. Lin, Y. Zhao, M. Liu, M. Qiu, Y. Dong, Z. Duan, Y. H. Li, B. Pingguan-Murphy, T. J. Lu and F. Xu, *J. Mater. Chem. C*, 2014, 2, 3671-3676.
- [39] Z.Jia, K. Zheng, D. Zhang, D. Zhao, W. Qin, *J. Nanosci. Nanotechnol.*, 2011, 11, 9690-9692.
- [40] D. T. Klier and M. U. Kumke, *J. Mater. Chem. C*, 2015, 3, 11228-11238.
- [41] a) D. Chen, M. Xu, M. Ma, P. Huang, *Dalton Trans.*, 2017, 46, 15373-15385; b) D. Chen, P. Huang, *Dalton Trans.*, 2014, 43, 11299-11304.
- [42] a) H. Jia, C. Xu, J. Wang, P. Chen, X. Liu, J. Qiu, *CrystEngComm*, 2014, 16, 4023-4028; b) H. Park, G.Y. Yoo, M.S. Kim, K. Kim, C. Lee, S. Park, W. Kim, *J. Alloys Comp.*, 2017, 728, 927-935.

- [43] W.H. Zachariasen, *Acta Crystallogr.*, 1951,4,231–6.
- [44] T.Grzyb, M. Weclawiak, J. Rozowska, S. Lis, *J Alloy Comp*,2013, 576, 345–9.
- [45] W. Yang, S.H. Kim, S. Park, *J Alloy Comp*, 2016,673,1–7.
- [46] S. Park, W. Yang, C.Y. Park, M. Noh, S. Choi, D. Park, et al., *Mater Res Bull* 2015,71,25–9.
- [47] a) W.Yang, S. Park, *RSC Adv* 2016,6,12652–6; b) C.Y. Park, S. Park, *J Lumin* 2016, 178, 463–9.
- [48] W. Yang, X. Li, D. Chi, H. Zhang, X. Liu, *Nanotechnology*, 2014,25,482001.
- [49] H. He, Q. Liu, D. Yang, Q. Pan, J. Qiu, G. Don, *Sci Rep* 2016,6:35348.
- [50] G. Chen, H. Qiu, P.N. Prasad, X. Chen, *Chem Rev* 2014; 114:5161–214.
- [51] Y. Zhang, X. Li, Z. Hou, J. Lin, *Nanoscale* 2014:6763–71.
- [52] M. Wang, G. Abbineni, A. Clevenger, C. Mao, S. Xu, *Nanomed Nanotechnol Biol Med*, 2011,7,710–29.
- [53] T. Grzyb, M. Weclawiak, J. Rozowska, S. Lis, *J Alloy Comp*, 2013,576,345–9.
- [54] S. Park, W. Yang, C.Y. Park, M. Noh, S. Choi, D. Park, et al., *Mater Res Bull* 2015, 71, 25–9.
- [55] a) N. Rakov, R.B. Guimarães, B.W.Lozano, G.S. Maciel, *J Appl Phys*, 2013,114; b) G. Scholz, M. Dreger, R. Bertram, E. Kemnitz, *Dalton Trans*, 2015,44,13522–9.
- [56] S.T. Zhang, M. Modreanu, H. Roussel, C. Jiménez, J.L. Deschanvres, *Dalton Trans*. 2018, 47, 2655-2661.
- [57] M. Mannini, F. Pineider, C. Danieli, F. Totti, L. Sorace, P. Saintavit, M. A. Arrio, E. Otero, L. Joly, J. C. Cezar, A. Cornia, R. Sessoli, *Nature* 2010, 468, 417–421.
- [58] N. Bahlawane, K. Kohse-Höinghaus, T. Weimann, P. Hinze, S. Röhe, M. Bäumer, *Angew. Chem. Int. Ed.* 2011, 50, 9957–9960; *Angew. Chem.* 2011, 123, 10131.
- [59] E. Biavardi, C. Tudisco, F. Maffei, A. Motta, C. Massera, G. G. Condorelli, E. Dalcanale, *Proc. Natl. Acad. Sci. USA* 2012, 109, 2263–2268
- [60] S. A. DiBenedetto, A. Facchetti, M. A. Ratner, T. J. Marks, *Adv. Mater.*, 21, (2009), 1407-1433.

- [61] P. J. Hotchkiss, S. C. Jones, S. A. Paniagua, A. Sharma, B. Kippelen, N. R. Armstrong, S. R. Marder, *Acc. Chem. Res.* 2012, 45, 337–347.
- [62] D. Hueber, M. Hoffmann, B. Louis, P. Pale, A. Blanc, *Chem. Eur. J.* 2014, 20, 3903–3907
- [63] J. Meyer, S. Hamwi, M. Kröger, W. Kowalsky, T. Riedl, A. Kahn, *Adv. Mater.* 2012, 24, 5408–5427.
- [64] P. Poizot, S. Laruelle, S. Grugeon, L. Dupont, J.-M. Tarascon, *Nature* 2000, 407, 496–499.
- [65] a) X. Qian, K. Fuku, Y. Kuwahara, T. Kamegawa, K. Mori, H. Yamashita, *Chem Sus Chem* 2014, 7, 1528–1536; b) G. Pellegrino, G. G. Condorelli, V. Privitera, B. Cafra, S. Di Marco, A. Alberti, *J. Phys. Chem. C* 2011, 115, 7760–7767.
- [66] B.H. Farnum, K.-R Wee, T. J. Meyer, *Nature Chemistry*, 8, (2016), 845-852.
- [67] M. Colombo, S. Carregal-Romero, M. F. Casula, L. Gutiérrez, M. P. Morales, I. B. Böhm, J. T. Heverhagen, D. Prospero, W. J. Parak, *Chem. Soc. Rev.* 2012, 41, 4306–4334.
- [68] I. Sugiyama, N. Shibata, Z. Wang, S. Kobayashi, T. Yamamoto, Y. Ikuhara, *Nature Nanotechnol.* 2013, 8, 266–270.
- [69] a) J. M. Caruge, J. E. Halpert, V. Bulovic, M. G. Bawendi, *Nano Lett.* 2006, 6, 2991–2994; b) J. Huang, G. Natu, Z. Q. Ji, P. Hasin, Y. Y. Lu, *J. Phys. Chem. C* 2011, 115, 25109–25114.
- [70] A. Nattestad, A. J. Mozer, M. K. R. Fischer, Y.-B. Cheng, A. Mishra, P. Bäuerle, U. Bach, *Nat. Mater.* 2010, 9, 31–35
- [71] F. Decker, S. Passerini, R. Pileggi, B. Scrosati, *Electrochim. Acta* 1992, 37, 1033–1038.
- [72] R. Lo Nigro, S. Battiato, G. Greco, P. Fiorenza, F. Roccaforte, G. Malandrino, *Thin Solid Films* 2014, 563, 50–55.
- [73] J. Fu, C. Zhao, J. Zhang, Y. Peng, E. Xie, *ACS Appl. Mater. Interfaces* 2013, 5, 7410–7416.

- [74] A. Echresh, M. Echresh, V. Khranovskyy, O. Nur, M. Willander, *Journal of Luminescence* 2016, 178, 324-330.
- [75] P. Misra, V.K. Sahu, R.S. Ajimsha, A.K. Das, B. Singh, *Journal of Physics D: Applied Physics*, 2017, 50, 415106/1-415106/6.
- [76] P. Naderi Asrami, M. Saber Tehrani, P. Aberoomand Azar, S.A. Mozaffari, *Journal of Electroanalytical Chemistry* 2017, 801, 258-266.
- [77] P. A. Premkumar, M. Toeller, C. Adelman, J. Meersschant, A. Franquet, O. Richard, H. Tielens, B. Brijs, A. Moussa, T. Conard, H. Bender, M. Schaekers, J. A. Kittl, M. Jurczak, S. Van Elshocht, *Chem. Vap. Deposition* 2012, 18, 61–69.
- [78] B.A. Reguig, A. Khelil, L. Cattin, M. Morsli, J.C. Bernede, *Applied Surface Science* 2007, 253, 4330-4334.
- [79] S. Benramache, M. Aouassa, *Journal of Chemistry and Materials Research* 2016, 5, 119-122.
- [80] A. Gulino, F. Lupo, D. A. Cristaldi, S. Pappalardo, C. Capici, G. Gattuso, A. Notti, M. F. Parisi, *Eur. J. Inorg. Chem.* 2014, 3, 442–449.
- [81] L. Newton, T. Slater, N. Clark, A. Vijayaraghavan, *J. Mater. Chem. C* 2013, 1, 376–393.
- [82] M. Klaumünzer, A. Kahnt, A. Burger, M. Mackovic, C. Münzel, R. Srikantharajah, E. Spiecker, A. Hirsch, W. Peukert, D. M. Guldi, *ACS Appl. Mater. Interfaces* 2014, 6, 6724–6730.
- [83] G. Guerrero, J. G. Alauzun, M. Granier, D. Laurencin, P. H. Mutin, *Dalton Trans.* 2013, 42, 12569–12585.
- [84] a) C. Sanchez, F. Ribot, *New J. Chem.* 1994, 18, 1007; b) J.Y.Wen, G.L. Wilkes, *Chem. Mater.* 1996,8, 1667.
- [85] Do Han Kim, Mark D. Losego, Qing Peng, and Gregory N. Parsons, *Adv. Mater. Interfaces* 2016, 3, 1600354.
- [86] George, S. M. *Chem. Rev.* 2009, 110, 111–131.
- [87] E. Smecca, C. Tudisco, A. E. Giuffrida, M. R. Catalano, A. Speghini, G. Malandrino, G. G. Condorelli, *Eur. J. Inorg. Chem.*, 2015, 1261-1268.

- [88] B. Jaffe, *Piezoelectric ceramics*, Elsevier, 2012, vol. 3.
- [89] A. Kojima, K. Teshima, Y. Shirai and T. Miyasaka, *J. Am. Chem. Soc.*, 2009, 131, 6050–6051.
- [90] J. Wang, J. B. Neaton, H. Zheng, V. Nagarajan, S. B. Ogale, B. Liu, D. Viehland, V. Vaithyanathan, D. G. Schlom, U. V. Waghmare, N. A. Spaldin, K. M. Rabe, M. Wuttig and R. Ramesh, *Science*, 2003, 299, 1719–1722.
- [91] S. Aharon, A. Dymshits, A. Rotem and L. Etgar, *J. Mater. Chem. A*, 2015, 3, 9171–9178.
- [92] Kojima, A.; Teshima, K.; Shirai, Y.; Miyasaka, T. *J. Am. Chem. Soc.* 2009, 131, 6050.
- [93] L. K. Ono, E. J. Juarez-Perez, and Y. Qi, *ACS Appl. Mater. Interfaces* 2017, 9, 30197–30246
- [94] (a) H. Zhou, Q. Chen, G. Li, S. Luo, T. Song, H. Duan, Z. Hong, J. You, Y. Yang; *Science* 2014, 345, 542. (b) N. Jeon, J. Noh, W. Yang, Y. Kim, S. Ryu, J. Seo, S. Seok; *Nature*, 2015, 517, 476. (c) W. Chen, Y. Wu, Y. Yue, J. Liu, W. Zhang, X. Yang, H. Chen, E. Bi, I. Ashraf, M. Gratzel, L. Han; *Science* 2015, 350, 944.
- [95] a) J. Bisquert, Y.B. Qi, T. Ma, Y. Yan, *ACS Energy Lett.*, 2017, 2, 520–523. b) N. G. Park, M. Gratzel, T. Miyasaka, K. Zhu, K. Emery, *Nat. Energy* 2016, 1, 16152. c) T.B. Song, Q. Chen, H.P. Zhou, C.Y. Jiang, H. Wang, Y. Yang, Y.S. Liu, J.B. You, Y. Yang, *J. Mater. Chem. A*, 2015, 3, 9032–9050.
- [96] a) P. Docampo, T. Bein, *Acc. Chem. Res.* 2016, 49, 339–346. b) M. Remeika, S.R. Raga, S. Zhang, Y.B. Qi, *J. Mater. Chem., A* 2017, 5, 5709–5718. c) M.R. Leyden, Y. Jiang, Y.B. Qi, *J. Mater. Chem. A*, 2016, 4, 13125–13132.
- [97] H.S. Kim, C. R. Lee, J.H. Im, K.B. Lee, T. Moehl, A. Marchioro, S.J. Moon, R. Humphry-Baker, J.H. Yum, J.E. Moser, *Sci. Rep.* 2012, 2, 591.
- [98] S. D. Stranks and H. J. Snaith, *Nat. Nanotechnol.*, 2015, 10, 391–402.
- [99] a) G. Niu, X. Guo and L. Wang, *J. Mater. Chem. A*, 2015, 3, 8970–8980. b) Y.-Y. Zhang, S. Chen, P. Xu, H. Xiang, X.-G. Gong, A. Walsh and S.-H. Wei, *AIP Adv.*, 2015, 01301.

[100] a) G. Giorgi, J.-I. Fujisawa, H. Segawa and K. Yamashita, *J. Phys. Chem. Lett.*, 2013, 4, 4213–4216. b) W.-J. Yin, J.-H. Yang, J. Kang, Y. Yan and S.-H. Wei, *J. Mater. Chem. A*, 2015, 3, 8926–8942. c) K.P. Marshall, R.I. Walton and, R.A. Hatton, *J. Mater. Chem. A*, 2015, 3, 11631–11640.

[101] J. Liang, C. Wang, Y. Wang, Z. Xu, Z. Lu, Y. Ma, H. Zhu, Y. Hu, C. Xiao, X. Yi, G. Zhu, H. Lv, L. Ma, T. Chen, Z. Tie, Z. Jin, and J. Liu, *J. Am. Chem. Soc.* 2016, 138, 15829–15832.

[102] A. F. Akbulatov, S. Y. Luchkin, L. A. Frolova, N. N. Dremova, K.L. Gerasimov, I. S. Zhidkov, D. V. Anokhin, E. Z. Kurmaev, K.J. Stevenson, and P. Troshin, *J. Phys. Chem. Lett.* 2017, 8, 1211–1218.

CHAPTER 2

MOCVD fabrication of Ln³⁺ doped fluoride thin films

A simple metal organic chemical vapor deposition approach is applied to the fabrication of CaF₂ nanostructured thin films using the fluorinated “second-generation” β -diketonate compound Ca(hfa)₂•diglyme•H₂O as a Ca-F single-source precursor. The versatility of the process is demonstrated for the fabrication of up-converting Yb/Er and Yb/Tm codoped CaF₂ films on Si, quartz, and glass substrates. The Ln(hfa)₃•diglyme (Ln = Tm, Er, Yb) precursors are used as sources of the doping ions.

In addition, metal organic chemical vapor deposition method has been successfully applied for the synthesis of NaYF₄ and KYF₄ thin films. The fluorinated “third-generation” bimetallic precursors NaY(hfa)₄•tetraglyme, synthesized in a previous work (vide infra), and the novel KY(hfa)₄•tetraglyme have been the starting point and the preliminary results confirm that the MOCVD approach yields reproducibly and selectively the synthesis of films of the pure KYF₄ phase and of the pure hexagonal NaYF₄ phase, which show the best host behavior for the Ln doping ions compared to the cubic structure, and without any impurity.

These final goals have been achieved through an accurate optimization of the operative parameters, such as the deposition temperature, the vaporization temperature of the precursors, the choose of the substrates and their positions inside the reactor.

Structural, morphological, and compositional characterization of the films shows the formation of polycrystalline thin films with a very uniform surface and suitable doping. In fact, an appropriate tuning of the mixture composition for the lanthanide

doped CaF₂ system, i.e. the Ca:Ln ratio in the multicomponent source, permits the deposition of films with the desired stoichiometry. The Ln³⁺ doped CaF₂ films show promising up-conversion properties in the visible and near infrared regions upon laser excitation for different doping mixtures.

2.1 Introduction

Alkaline earth fluoride materials have attracted great attention due to a wide variety of applications in dielectrics, optics, optoelectronics, and photonics [1–4]. In particular, alkaline earth fluoride such as MF₂ (M: Ca, Sr) and MREF₄ (M: Na, K; RE: Y, Gd) has been regarded as the most efficient hosts for up-conversion (UC) or down-conversion emissions, also due to their low phonon energy, which minimize non-radiative de-excitation processes [5–8]. UC and DC processes could enhance the efficiency of photovoltaic devices since it makes possible to collect the radiation energy outside the absorption range of the photoactive material (usually silicon) by shifting its energy to a more suitable optical region. In addition, rare-earth doped fluoride compounds are promising luminescent materials as phosphors and in technological applications as micro- and nanoscale thermometry for microelectronics and for biomedical assays [9–11].

Several studies are available on the deposition methods applied for fabrication of alkaline earth fluoride films such as sputtering [12,13], atomic layer deposition [14], molecular beam epitaxy [15,16], sol-gel chemical routes [17]. Nevertheless, the metal organic chemical vapor deposition (MOCVD) has the potential advantage of being a very reliable and reproducible method for the fast production of films with high uniformity degree in both thickness and composition over large areas.

MOCVD has been already applied to the deposition of the fluorite films; nevertheless, most of these reports used a fluorine-free calcium source, thus a second precursor is needed as the fluorine source [18].

2.2 Ln³⁺ doped CaF₂ thin films: MOCVD fabrication and their up-conversion properties

In this study, we report for the first time the synthesis of CaF₂ films doped with Yb³⁺,Er³⁺ or Yb³⁺,Tm³⁺ through a simple MOCVD route on various substrates using a molten mixture consisting of the Ca(hfa)₂•diglyme•H₂O and the suitable Ln(hfa)₃•diglyme [Ln = Yb, Er, Tm; Hhfa = 1,1,1,5,5,5-hexafluoro-2,4-pentanedione; diglyme = 2-methoxyethyl ether] precursors in an appropriate stoichiometric ratio (structures in fig. 1).

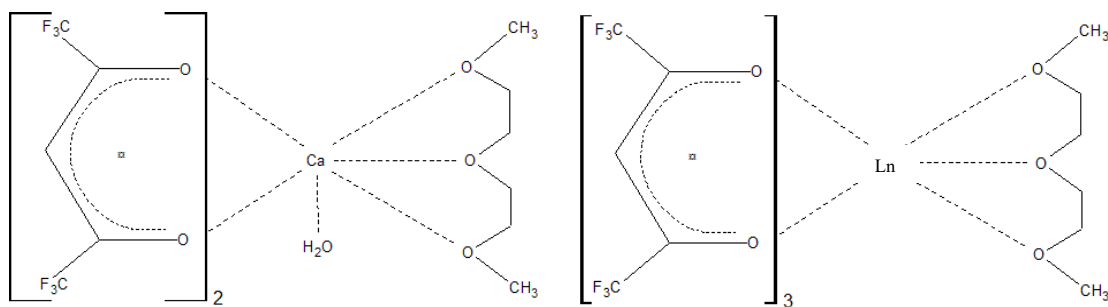


Fig. 1 Ca(hfa)₂•diglyme•H₂O and Ln(hfa)₃•diglyme structures.

The advantages of the present approach are various:

- I. the metal precursors represent also a source of fluorine, thus avoiding the use of harmful hydrogen fluoride (HF) or other fluorine sources during the deposition step;
- II. the application of all the required metal precursors in a unique multicomponent mixture allows for an easy control of the precursor source by simply adjusting the stoichiometric ratio;

- III. the use of the same polyether (diglyme) to complete the coordination sphere of calcium and lanthanide ions avoids the undesirable potential ligand exchange.

The structural, morphological, compositional, and luminescent properties point to the formation of good quality CaF₂ films with promising up-conversion properties reflecting the correct stoichiometry of the films. The films were deposited on glass, quartz, and Si (100) substrates.

Given the same nature of the ligand and similar vaporization temperature ranges of the single precursors [19-21], no ligand exchange occurs and an efficient vaporization without thermal degradation takes place.

2.2.1 Experimental Section

The Ln(hfa)₃•diglyme precursors were synthesized as previously reported in refs. [19] and [22]. The Ca(hfa)₂•diglyme•H₂O adduct has been prepared through a one-step reaction from the calcium oxide, Hhfa and diglyme ligands in dichloromethane under refluxing. The synthesis has been carried out starting from the CaO (0,40 gr; 0.71×10⁻²mol) suspended in dichloromethane (40 ml) with diglyme (0,770 ml, 0,71×10⁻² mol) and H-hfa (1ml, 1.42×10⁻²mol). The mixture was refluxed, under stirring, for 90 min. The solution was collected by filtration under vacuum and the excess of CaO was filtered off. White crystals were obtained upon evaporation of the solvent, were washed two times in pentane and recovered by filtration.

The films were deposited on glass, quartz, and Si (100) under low-pressure in a horizontal hot-wall reactor, in the 450–550 °C temperature range. An appropriate ratio of the Ca, Yb, and Er (or Tm) complexes were used at 120°C, a suitable temperature for an efficient vaporization without thermal degradation. Under this condition the source is a molten mixture, since the Ca(hfa)₂•diglyme•H₂O and Ln(hfa)₃•diglyme melt in the 106–109 °C and 72–76 °C ranges, respectively. Heating rates of 40 and 8 °C min⁻¹ were used for the reactor chamber and the vaporization

reservoir, respectively. Argon was used as a carrier gas, while oxygen as the reactant gas was introduced in the main flow into close proximity to the reaction zone.

Film structure was analyzed by XRD in glancing incidence mode (0.5°) using a Smartlab Rigaku diffractometer, equipped with a rotating anode of Cu $K\alpha$ radiation operating at 45 kV and 200 mA. Film morphology was analyzed by FE-SEM using a ZEISS SUPRA 55 VP field emission microscope. The films deposited on Si were analyzed as-dep, while films deposited on glass or quartz were Au-coated prior FE-SEM characterization. The EDX spectra were recorded using an INCA-Oxford windowless detector, having a resolution of 127 eV as the full width half maximum (FWHM) of the Mn $K\alpha$.

For the luminescence characterization, the samples were excited at 980 nm using a diode laser as the source (CNI Optoelectronics Tech), with an intensity of 3.2 W mm^{-2} . The emission spectra were detected by a Black Comet SR Spectrometer (StellarNet Inc), with optical spectral resolution of 1 nm.

2.2.2 Results and discussion

XRD analysis

The X-ray diffraction (XRD) analysis of the samples CaF_2 : Yb 18%, Er 2% (mol % with respect to the total metal content) deposited at 500°C on Si (100) exhibits patterns associated with a cubic CaF_2 phase (ICDD No. 35-0816) (fig. 2). The diffraction features observed at 2θ values of 28.25° , 32.75° , 47.00° and 55.75° are associated with the 111, 200, 220, and 311 reflections, respectively. The XRD measurements of films deposited at lower and higher temperatures and on different substrates show similar patterns. A closer look to the patterns, recorded with a 0.02° resolution, of films containing different amounts of Yb^{3+} ions reveals a small shift of the peak positions with respect to those found for the undoped CaF_2 film (fig. 3). A magnification of the 220 reflection is reported in fig. 4. The red line indicates the position of the ICDD

CaF₂ 220 peak; a slight shift toward higher angles is found for all the Yb³⁺ doped CaF₂ films.

This behavior may be correlated on the one side to the ionic radii of the involved doping ions and on the other hand to the need of charge balance due to the different charge 2+ of calcium and 3+ of lanthanide ions, which can be compensated with additional fluoride ions.

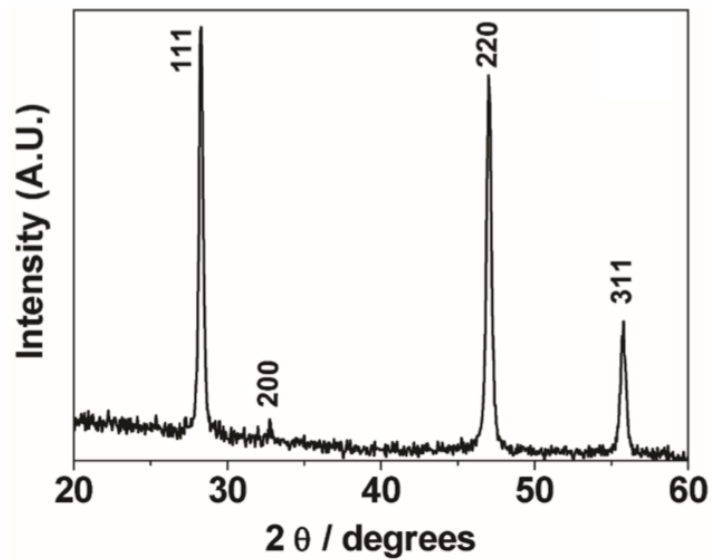


Fig. 2 XRD pattern of the CaF₂: Yb(18%), Er(2%) film deposited at 500 °C on Si.

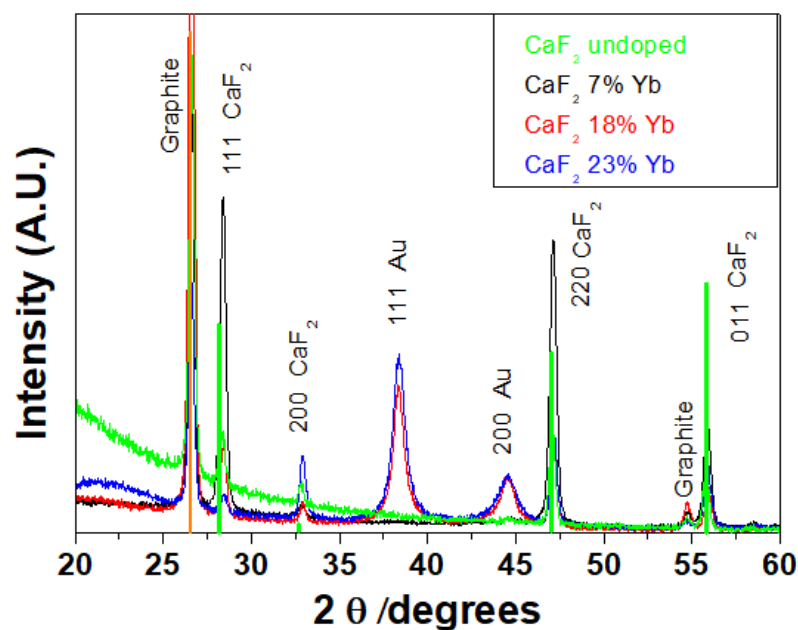


Fig. 3 XRD patterns of CaF₂ films doped with different amount of Yb: undoped, 7%,18% and 23%.

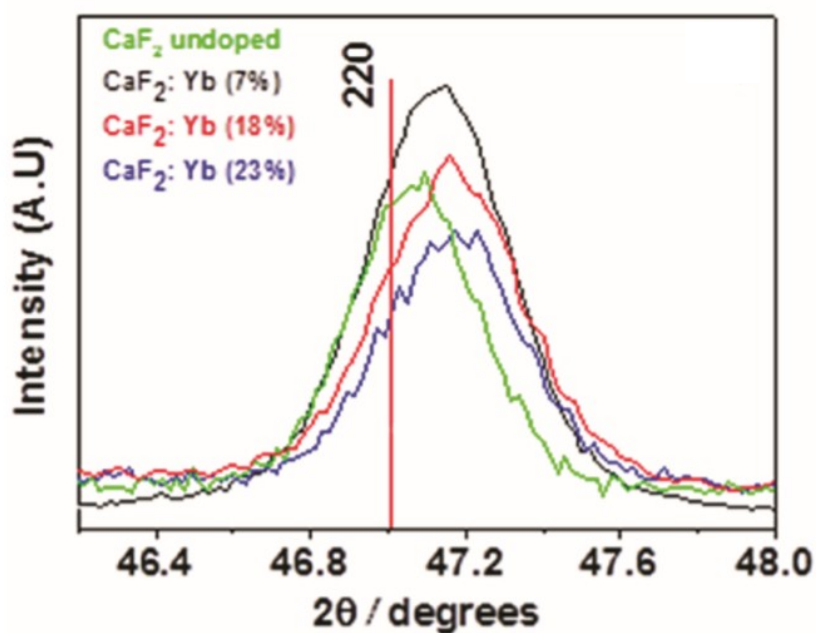


Fig. 4 A magnification of the 220 reflection of the CaF₂ films doped with different amount of Yb.

The lanthanide ions are supposed to substitute calcium, thus assuming an eight coordination, considering that the Ca²⁺ and Ln³⁺ ions have similar ionic radii, with Ca²⁺ = 1.12 Å and the Ln³⁺ ranging from 1.16 Å (La³⁺) to 0.977 Å (Lu³⁺), in eightfold

coordination [23]. In particular, the Yb^{3+} , Er^{3+} , and Tm^{3+} ions have ionic radii of 0.985, 1.004, and 0.994 Å, respectively (in eightfold coordination) [23], slightly smaller than the Ca^{2+} ions. Therefore, a mere effect due to substitution of Ca^{2+} by Ln^{3+} ions gives rise to a shift toward higher 2θ angles.

The a-axis parameters of the CaF_2 : Yb, Er films and for an undoped MOCVD-grown CaF_2 film have been determined as average of all the values obtained from the individual reflections by using the relationship between hkl and the lattice parameter for a cubic structure, and they are reported in Table 1 as a function of the ytterbium doping. In this context, it is worth mentioning that the a-axis parameter has been estimated using graphite as an internal standard.

Sample	Yb ^{a)} [%]	A-axis [Å]
CaF_2 (ICDD No. 35-816)	–	5.4630
CaF_2 film	Undoped	5.46(0)
CaF_2 film	7	5.45(3)
CaF_2 film	18	5.44(6)
CaF_2 film	23	5.44(5)

^{a)}Determined by EDX.

Table 1. Values of the a-axis parameters of the CaF_2 : Yb^{3+} , Er^{3+} films grown on quartz at 500 °C.

The energy dispersive X-ray (EDX) analysis confirms that the Yb^{3+} ions are incorporated in the films, but further experiments are needed to clarify the reason of the observed similarity between the a-axis parameter for the two 18% and 23% ytterbium doped films. The decrease of the a-axis parameter may be related to the slight smaller ionic radius of Ln^{3+} vs Ca^{2+} and it clearly indicates that the lanthanide ions are incorporated in the crystalline lattice. Nevertheless, both the difference of the ionic radii of the metal ions and the effect of the charge compensation, which could

be satisfied by the insertion of interstitial fluoride ions or clusters, has to be considered to explain the peak shift.

In addition, thermal stresses between CaF₂ films and the Si substrate, due to the considerable difference in their thermal expansion coefficients (vide infra), could have effect in the lattice parameter of the deposited films. This effect has been deeply studied in the morphologic characterization and the optimized parameters of time deposition (60 min), and cooling rate (3 °C•min⁻¹) from deposition temperature to room temperature, yields crack-free films on Si and thickness of about 500nm.

EDX analysis

Quantitative EDX analysis confirms a uniform stoichiometry on the whole surface for all the films and for all the deposition temperatures. The EDX spectrum of a film deposited at 500 °C (fig. 5) shows the L and M lines of ytterbium, the K α and K β peaks of calcium, the K α peak of fluorine, and the K α peak of the silicon substrate. The erbium and thulium peaks, relative to the nominal concentration of 2%, are scarcely detectable, due to their low concentrations that are on the borderline of the detection limit of the EDX technique. It is worthy of noting the absence of C and O, whose K α peaks should appear at 0.277 and 0.525 keV, respectively.

The concentrations of the dopants, typically used for efficient UC emission [24] of 18% of ytterbium and 2% of erbium or thulium for the CaF₂ doped films, are found through EDX in samples deposited at 500°C. An accurate evaluation of the deposition temperature effect on atomic composition of the Ln dopants in the films has been done through EDX characterization. At temperatures of 450 °C the percentage of Ln³⁺ found in the films is higher than about 20% compared to the expected value based on the initial composition of the precursor mixture. On the contrary, at temperatures of 550 °C, the percentage of Ln³⁺ found is lower than about 18%. Finally, at deposition temperature of 500 °C the percentage composition of the doping ions obtained is the same of that initially set. Therefore, the doping amount increases upon increasing the deposition temperature and, on the contrary, decreases

at temperatures lower than 500°C. This finding may be related to a different decomposition behavior of the precursors, i.e., the Ca precursor likely decomposes more easily at lower temperature, so the net result is a major amount of Ca with respect to Ln, which reflects on the lower doping ratio observed at the lower temperature. In any case, the deposition temperature permits an accurate tuning of the stoichiometry, and an appropriate tuning of the mixture composition, i.e., the Ca:Ln ratio in the multicomponent source, permits the deposition of films with a desired stoichiometry at whatever temperature.

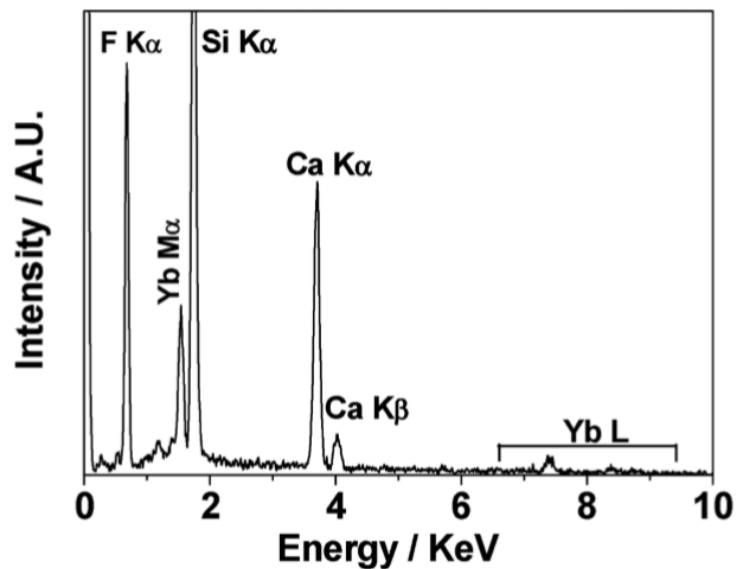


Fig. 5 EDX spectrum of the CaF₂: Yb(18%), Er(2%) film deposited at 500 °C on Si (001).

FE-SEM characterization

Microstructure and morphology of CaF₂ films have been studied by field emission scanning electron microscopy (FE-SEM). The FE-SEM images of the films deposited on Si (100) do not show a homogeneous surface. Film deposited at 500 °C for 90 min (fig. 6a) shows some swelling, while films deposited for 60 min show a significant cracking as observed in fig. 6b. These effects are likely due to the considerable difference in the thermal expansion coefficients of the CaF₂ film and that of the Si

substrate. In fact, the linear thermal expansion coefficient of CaF_2 spans in the range $16.5\text{--}19.4 \times 10^{-6} \text{ }^\circ\text{C}^{-1}$ versus the linear expansion coefficient of Si that is $2.6 \times 10^{-6} \text{ }^\circ\text{C}^{-1}$. The different behavior of swelling or cracking is essentially due to the different thickness, about $1 \text{ } \mu\text{m}$ for sample reported in fig. 6a and 500 nm for the sample reported in fig. 6b.

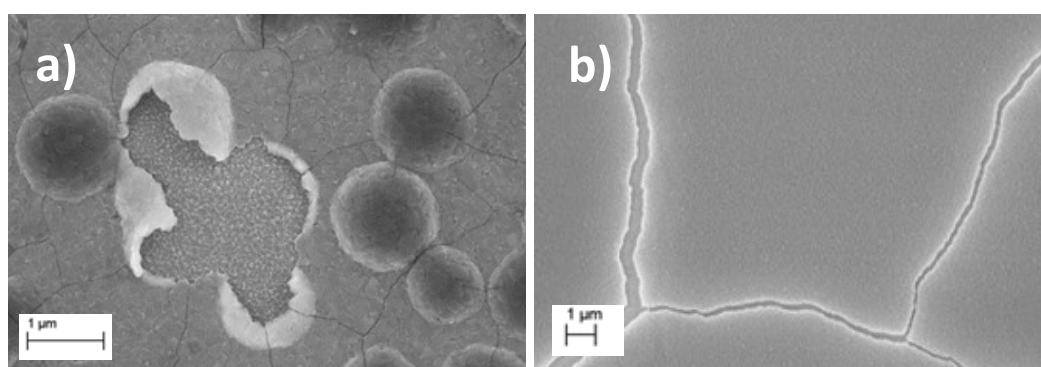


Fig. 6 FE-SEM images of the CaF_2 : Yb,Er films deposited at $500 \text{ }^\circ\text{C}$ for 90 min **a)** and 60 min **b)** on Si substrate.

Optimization of deposition conditions, i.e., very slow cooling rate ($3 \text{ }^\circ\text{C min}^{-1}$) from deposition temperature to room temperature, yields almost crack-free films on Si (fig. 7a). In figure 7b, the cross section of the film deposited on Si at $500 \text{ }^\circ\text{C}$ allows the thickness estimation of about 550 nm . Being the duration time 60 min, a growth rate of about $9\text{--}10 \text{ nm min}^{-1}$ may be derived. The presently observed growth rate is similar to that previously reported for the deposition of pure CaF_2 from the same precursor under similar conditions [25]. FE-SEM images of films grown on glass and quartz show a smooth homogeneous surface throughout the entire $10 \times 20 \text{ mm}^2$ surface. The Yb, Er co-doped CaF_2 films show crystalline grains of about 150 nm (fig. 7c,d). The CaF_2 : Yb,Tm have a uniform surface with crystalline grains of about 200 nm (fig. 7e,f). The FE-SEM investigations confirm the homogeneity of the film surfaces, independently of the deposition temperature.

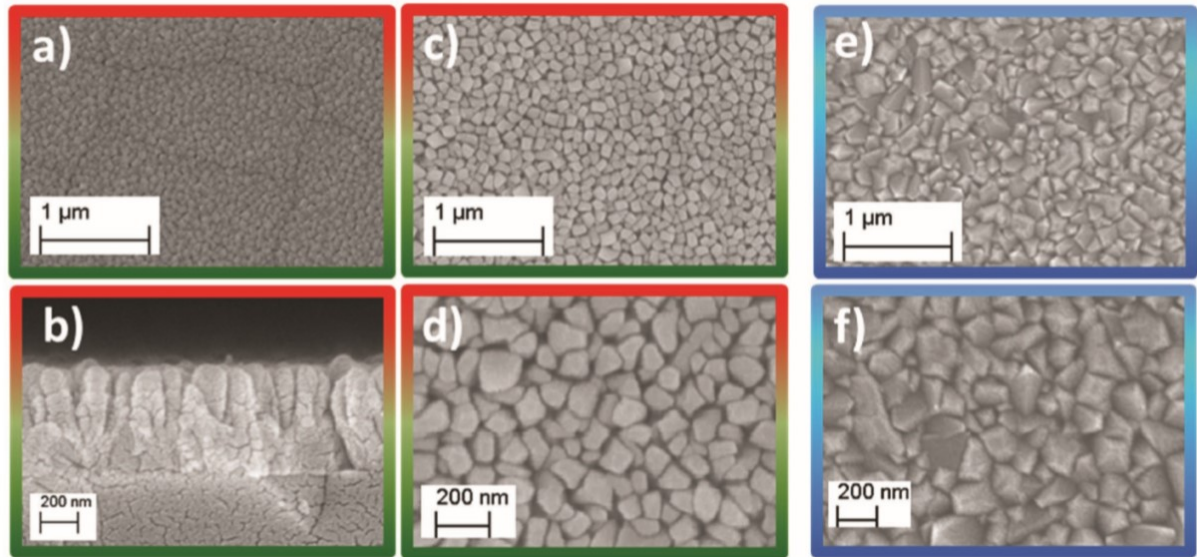


Fig. 7 FE-SEM images of the CaF_2 : Yb(18%), Er(2%) films deposited at 500 °C: **a)** plan view and **b)** cross section of films deposited on Si (100); **c)** low and **d)** high magnification of films deposited on quartz. **e)** Low and **f)** high magnification FE-SEM images of the CaF_2 : Yb(18%), Tm(2%) deposited at 500 °C on quartz.

2.2.3 Luminescent proprieties

Up-conversion measurements in the visible and near-infrared regions show that all the samples under investigation confirm bright luminescence upon 980 nm laser excitation. The spectra of CaF_2 :Yb,Er films deposited on Si (100) substrate at 500 °C are shown in fig. 8a. Upon laser excitation at 980 nm, Er^{3+} emissions in the green region around 525 and 550 nm due to $^2\text{H}_{11/2} \rightarrow ^4\text{I}_{15/2}$ and $^4\text{S}_{3/2} \rightarrow ^4\text{I}_{15/2}$ electronic transitions, respectively, and in the red region, around 660 nm due to $^4\text{F}_{9/2} \rightarrow ^4\text{I}_{15/2}$ transitions, indicating that $\text{Yb}^{3+} \rightarrow \text{Er}^{3+}$ UC processes are present. The complete assignments of the emission bands are reported in the caption of Fig. 8b and are in perfect agreement with the bands observed in the energy level diagrams for the Er^{3+} and Yb^{3+} ions and up-conversion mechanisms upon 980 nm laser excitation (Fig. 8b). It is noted that the red emission is stronger than the green one so that the luminescence at the naked eyes appears to be yellow-orange. The enhancement of the red emission with respect to the green one can be ascribed to the high Yb^{3+}

concentration (around 18% with respect to the total metal content) in the CaF₂ host, as also observed for other up-converting nanomaterials [26].

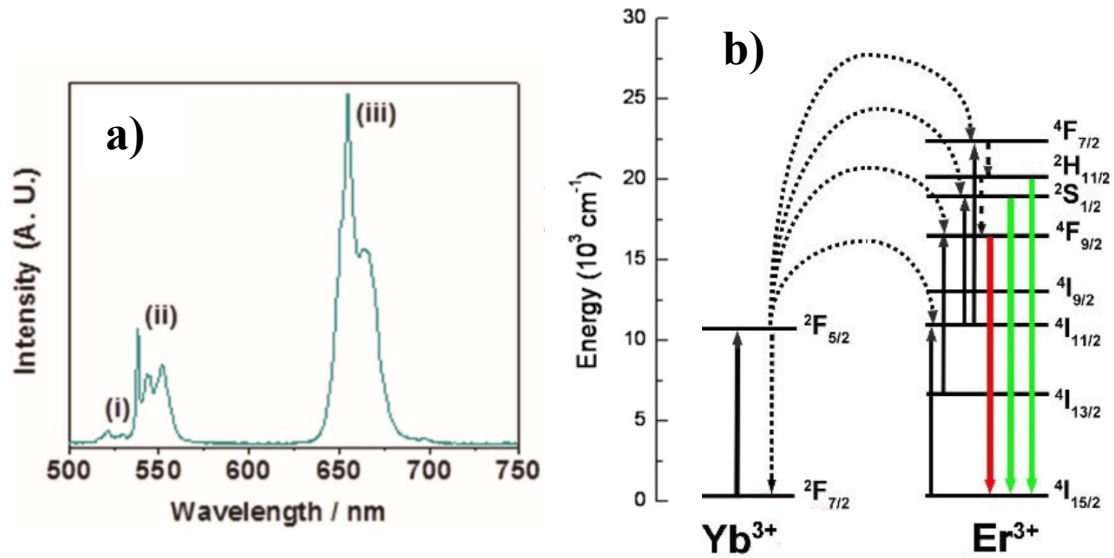


Fig. 8 a) Room temperature UC emission spectrum of a CaF₂:Yb(18%), Er(2%) film deposited on Si substrate at 500 °C. The peaks correspond to the Er³⁺ transition: (I) $^2H_{1/2} \rightarrow ^4I_{15/2}$; (II) $^4S_{3/2} \rightarrow ^4I_{15/2}$; (III) $^4F_{9/2} \rightarrow ^4I_{15/2}$. **b)** Energy level scheme for the Er³⁺ and Yb³⁺ ions and up-conversion mechanisms upon 980 nm laser excitation (laser intensity 3.2 W mm⁻²).

The emission spectra of the samples doped with Tm³⁺ show several bands in the UV, visible, and NIR regions, with the strongest band observed in the blue region. The up-conversion properties are similar for the film deposited on Si (fig. 9a) or on quartz (Fig. 9b). The spectrum may be assigned considering the following Tm³⁺ transitions: (I) $^1D_2 \rightarrow ^3H_6$; (II) $^1D_2 \rightarrow ^3F_4$; (III) $^1G_4 \rightarrow ^3H_6$, (IV) $^1D_2 \rightarrow ^3H_5$, (V) $^1G_4 \rightarrow ^3F_4$, (VI) $^1G_4 \rightarrow ^3H_5$, (VII) $^3H_4 \rightarrow ^3H_6$ (fig. 10).

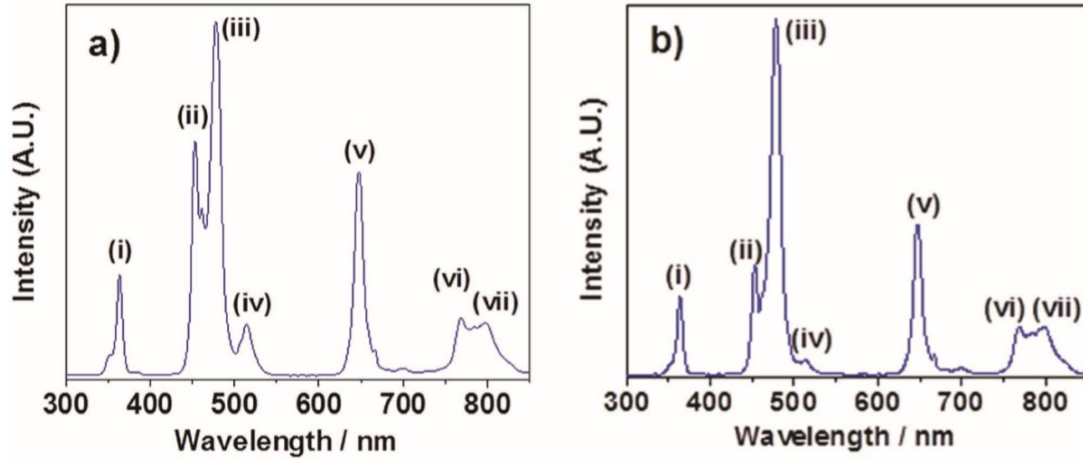


Fig. 9 UC emission spectra of CaF₂:Yb(18%),Tm(2%) films deposited at 500 °C on **a)** Si and **b)** quartz substrates. The peaks correspond to the Tm³⁺ transition: (I) ¹D₂ → ³H₆; (II) ¹D₂ → ³F₄; (III) ¹G₄ → ³H₆, (IV) ¹D₂ → ³H₅, (V) ¹G₄ → ³F₄, (VI) ¹G₄ → ³H₅, (VII) ³H₄ → ³H₆. All spectra were collected at room temperature upon 980 nm laser excitation (laser intensity of 3.2 W mm⁻²).

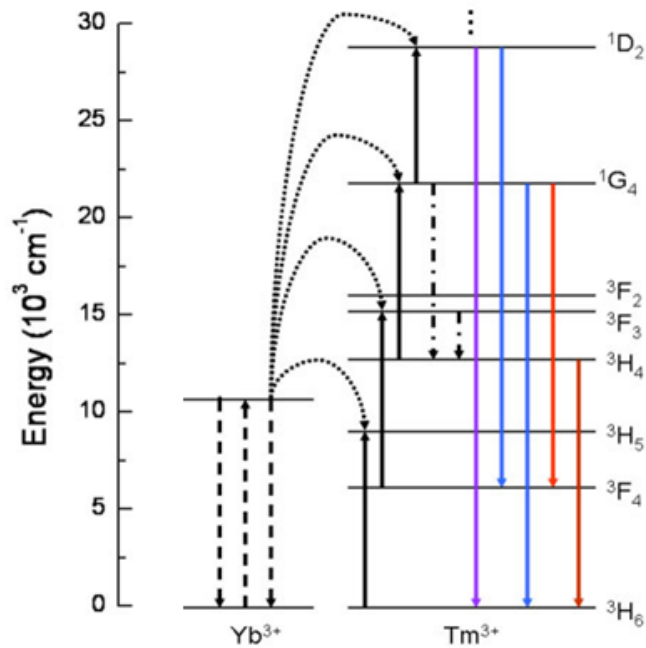


Fig. 10 Energy level scheme for the Tm³⁺ and Yb³⁺ ions and up-conversion mechanisms upon 980 nm laser excitation.

For both kinds of co-doped samples, the UC emission is clearly visible, indicating that an efficient Yb³⁺ → Er³⁺ or Tm³⁺ energy transfer is present. Some differences in

the relative intensities of the Tm^{3+} emission bands are observed for samples deposited on silicon and quartz substrates, in particular for the ${}^1\text{D}_2 \rightarrow {}^3\text{F}_4$ and ${}^1\text{G}_4 \rightarrow {}^3\text{H}_6$ emission transitions. Presently, this behavior cannot be easily rationalized, and it could be tentatively attributed to an effect of cross-relaxation processes among the Tm^{3+} ions, due to possible clustering of the lanthanide ions [27]. Additional experiments using samples at different Tm^{3+} concentration would be necessary in order to shed light on this issue.

2.3 NaYF₄ thin film: MOCVD growth of cubic and hexagonal phases

In the present work, preliminary results on the MOCVD synthesis of NaYF₄ nanostructured thin films are reported using the novel fluorinated bimetallic β -diketonate compound, synthesized in a previous work [28], NaY(hfa)₄•tetraglyme (Hhfa = 1,1,1,5,5,5 – hexafluoro - 2,4 - pentanedione; tetraglyme = 2, 5, 8, 11, 14 – Pentaioxapentadecane), which acts as single precursor for the metal components and the fluorine. An accurate optimization of the operative parameters, such as the deposition temperature and the substrates' positions inside the reactor, has been carried out to stabilize the fluoride hexagonal β -NaYF₄ phase that shows the best host behavior for the Ln doping ions compared to the cubic structure in the photovoltaic applications. X-ray diffraction and field emission scanning electron microscopy, lead to the evaluation of the deposition temperature on the final phase of the film and point to the formation of good quality hexagonal NaYF₄ films with a uniform and nanostructured morphology.

2.3.1 Experimental Section

The films were deposited on Si (100) under low-pressure in a horizontal hot-wall reactor, in the 350–500 °C temperature range. The single precursors was used at 160°C, a suitable temperature for an efficient vaporization without thermal

degradation. The $\text{NaY}(\text{hfa})_4 \bullet \text{tetraglyme}$ precursor was synthesized as reported in ref. [28]. Heating rates of 30 and 8 $^\circ\text{C min}^{-1}$ were used for the reactor chamber and the vaporization reservoir, respectively. Argon was used as a carrier gas, while oxygen as the reactant gas was introduced in the main flow into close proximity to the reaction zone. The XRD and FE-SEM characterizations of the films were carried out in analogous configuration equipment of the previous paragraph 2.2.1.

2.3.2 Results and discussion

The novel Na-Y precursor, provided by Battiato et al. [28], has been the starting point for the MOCVD growth of $\beta\text{-NaYF}_4$. The $\text{NaY}(\text{hfa})_4 \bullet \text{tetraglyme}$ complex has a ionic structure in which the rare earth metal is complexed by the β -diketonate hfa^- and the alkaline metal is complexed only by the tetraglyme, according to the general formula $[\text{Y}(\text{hfa})_4]^- [\text{Na} \bullet \text{tetraglyme}]^+$ (fig. 11).

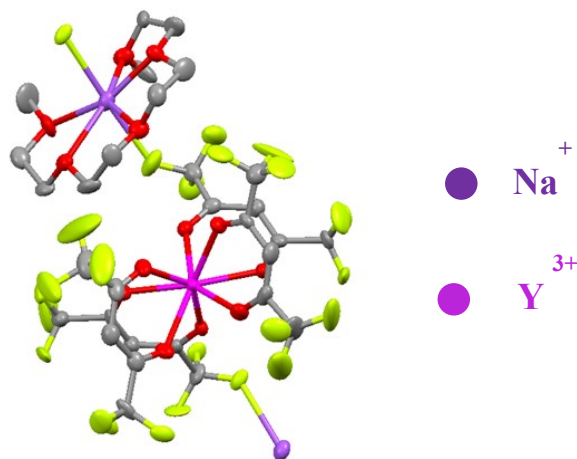


Fig. 11 Ball and stick view of the $[\text{Y}(\text{hfa})_4]^- [\text{Na} \bullet \text{tetraglyme}]^+$ complex (reprinted from ref. 28).

It is worth noting that this complex has been synthesized with a high yield in a single step, low-cost route from commercially available chemicals. The adduct is anhydrous and soluble in common organic solvents such as ethanol, dichloromethane, acetone. In regard to mass transport properties and thermal behavior studies of this

precursor, atmospheric pressure thermal gravimetric analysis and the differential scanning calorimetric data make it particularly attractive for preparation of Na, Y and F solid phases through the MOCVD approach.

The films deposited were characterized by XRD and FE-SEM analysis. These investigations allowed to evaluate the deposition temperature and the position of the substrates in the reactor on the films structure.

XRD analysis

In fig. 12a it is reported a diagram of the NaYF₄ phase stability, obtained through XRD analysis, in relation of deposition temperatures and positions A and B of the silicon substrate inside the hot wall horizontal MOCVD reactor. The A position corresponds to a site located closer to the precursor source in which the temperature is 100 °C lower than the nominal temperature of the reactor; and the B position corresponds to a site located closer to the center of the reactor in which the temperature is 50 °C lower than the nominal temperature (fig. 12b).

As evidence in this graph, at temperatures up to 400 °C only the cubic structure has been obtained. At the temperature of 450 °C the position of the substrates has a crucial role: the hexagonal phase is present for the films located in B, while in position A only a cubic structure is present. At 500 °C, on the other hand, only the hexagonal phase is present for all the films in both positions.

These data, which could appear in contrast with what has been observed in the literature, i.e. that the hexagonal phase is stable at lower temperatures [29], could be interpreted considering the growth technique that does not work under thermodynamic equilibrium conditions and sometimes stabilizes different phases from those thermodynamically stable in that given temperature range. These results can be traced back to a delicate balance between thermodynamic and kinetic factors in the formation of the phase.

Figure 13 shows the diffractograms of the deposited films with a cubic and hexagonal structure. The XRD measurements of samples NaYF₄ deposited on Si (100)

exhibit patterns associated with a cubic α - phase according to the ICDD 06-0342, due to the presence of peaks at 2θ values of 28.40° , 47.15° , and 56.05° associated with the 111, 220 and 311 reflections, respectively. The hexagonal β - NaYF_4 films nature has been assessed through the patterns showing the presence of peaks at 2θ values of 17.20° , 30.05° , 30.80° , 34.85° , 39.65° , 43.50° , 46.60° , 53.30° , 53.75° , and 55.20° , associated with the 100, 110, 101, 200, 111, 201, 210, 300, 211 and 102 reflections, respectively, of the β -phase (ICDD 16-0334).

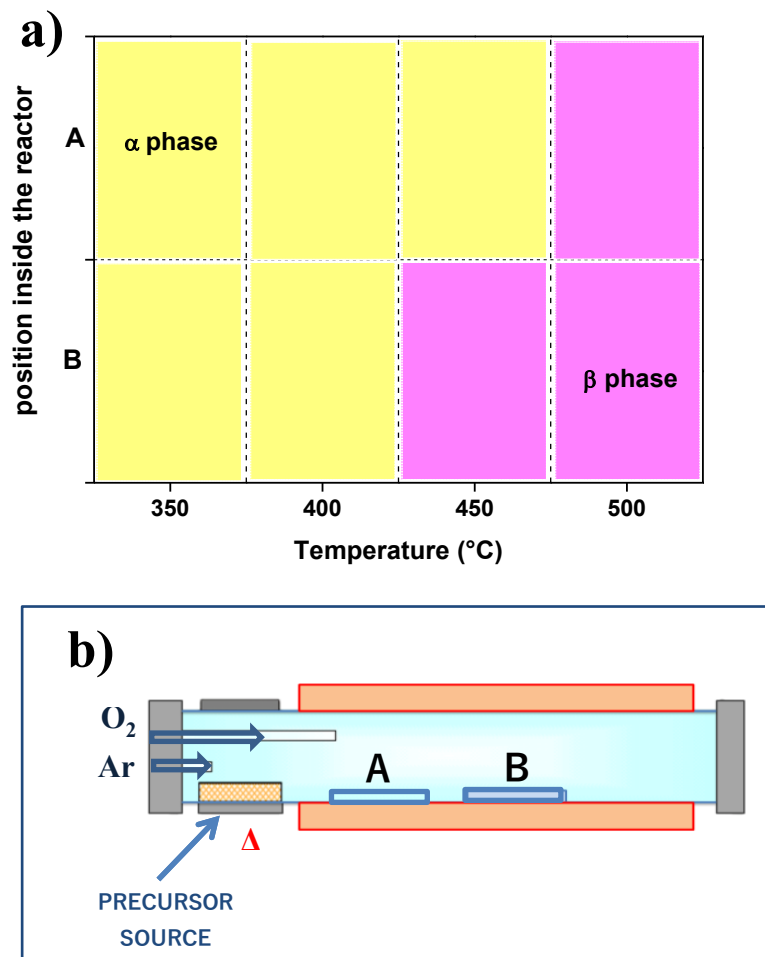


Fig. 12 a) Diagram of the NaYF_4 phases, obtained through XRD analysis, in relation of deposition temperatures and positions A and B of the substrates; **b)** scheme of hot wall horizontal MOCVD reactor.

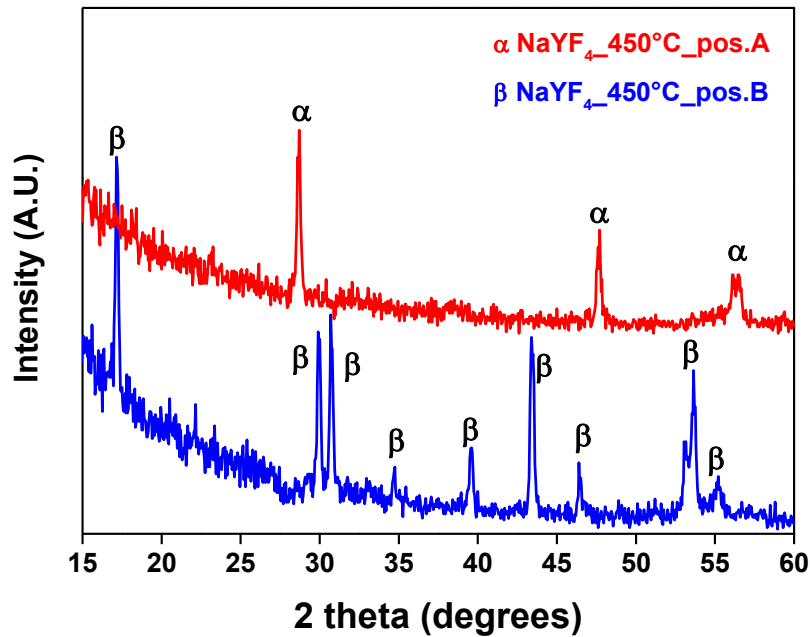


Fig. 13 XRD patterns of NaYF₄ films grown on Si(100) at 450°C in different positions.

FE-SEM characterization

Microstructure and morphology of NaYF₄ thin films have been studied by field emission scanning electron microscopy (FE-SEM). The FE-SEM images of the films deposited on Si(100) for 60 min show a homogeneous surface for all the samples, independently of phase structure, deposition temperature and their position inside the reactor. However, SEM images in fig. 14 show different morphologies in relation with the phase and the temperature in which they were deposited and on the basis of their position A or B inside the reactor. The α -NaYF₄ film deposited at 350 °C (fig. 14a) shows very small coalescence grains, while films deposited at 400 °C (fig. 14b) have a uniform surface with crystalline grains of about 100nm. At higher temperature 450°C and 500°C, the β -NaYF₄ thin films show similar smooth morphologies with “plate like” grains of about 250nm (fig. 14c,d).

The NaYF₄ thin films obtained at 450°C for 60 min on Si(100) have the cubic or the hexagonal structure in relation to their position A or B in the reactor and thus shows

two different morphologies: the β -NaYF₄ film in fig. 14e has a smooth surface with plate-like grains of about 250-300nm, the α -NaYF₄ film in fig. 14f has a nanostructured surface with very small grain of about 50nm. These morphologies could be explained due to the difference balance of nucleation and grown rate of the films in the two positions, in which the amount of precursor is different.

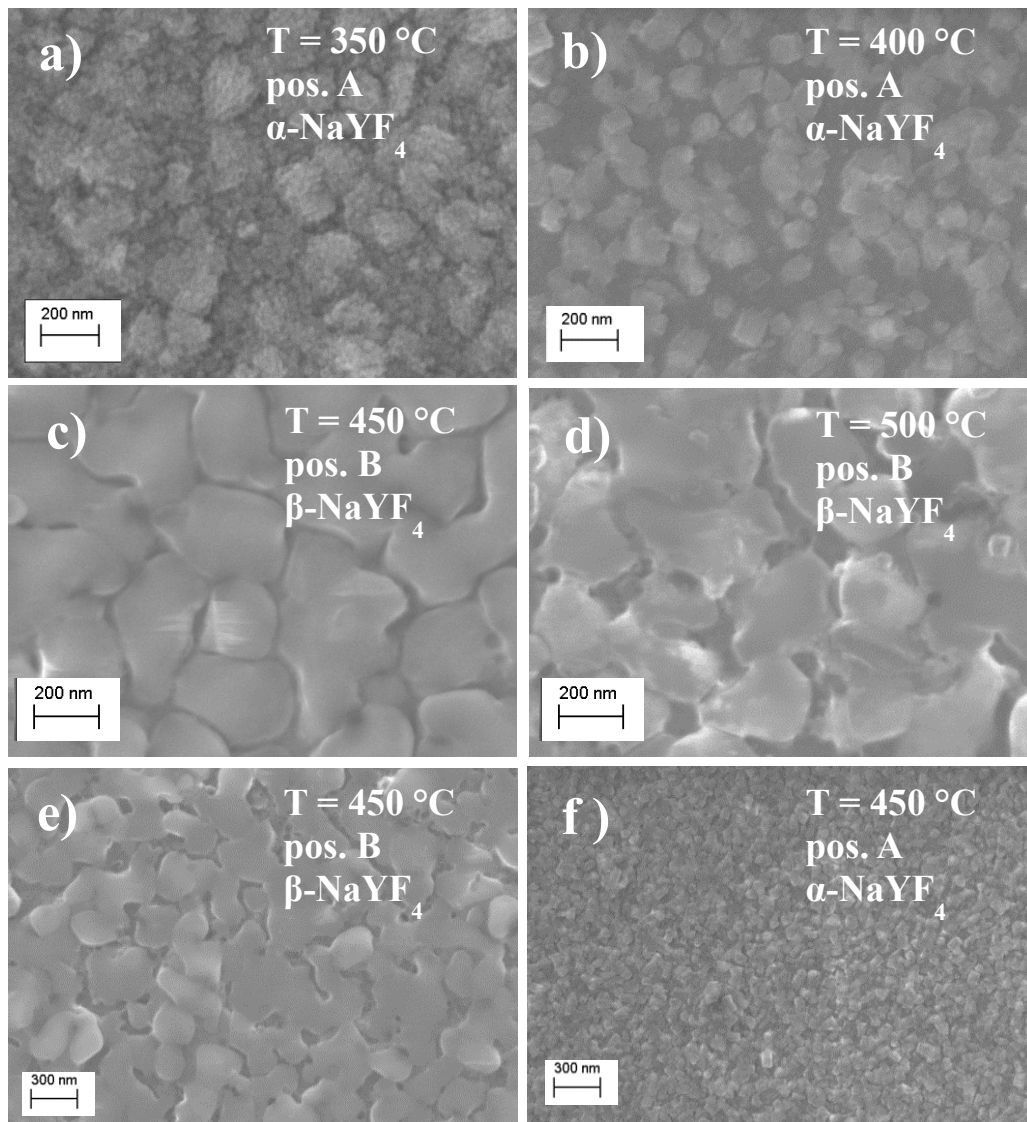


Fig. 14 FE-SEM images of the NaYF₄ deposited on Si(100): **a)** α phase at 350 °C in A; **b)** α phase at 400 °C in A; **c)** β phase at 450 °C in B; **d)** β phase at 500 °C in B. Low magnification FE-SEM images of NaYF₄ deposited on Si(100) at 450°C **e)** in pos B (β phase) and **f)** in pos A (α phase).

2.4 KYF₄ thin films: MOCVD synthesis through a new β -diketonate heterobimetallic potassium-yttrium precursor

A metal organic chemical vapor deposition method has been successfully applied for the fabrication of KYF₄ nanostructured thin films using the novel “third-generation” fluorinated bimetallic β -diketonate compound, KY(hfa)₄•tetraglyme (Hhfa = 1,1,1,5,5,5 – hexafluoro - 2,4 - pentanedione; tetraglyme = 2, 5, 8, 11, 14 – Pentaioxapentadecane), which acts as single-source precursor for the metal components and the fluorine.

The novel KY(hfa)₄•tetraglyme adduct has been synthesized through a one-step reaction with a high yield in the form of white non-hygroscopic crystals. The adduct was characterized by infrared spectroscopy (FT-IR), energy dispersive X-ray (EDX) analysis, differential scanning calorimetry analysis (DSC) and thermogravimetric analysis (TGA).

The precursor KY(hfa)₄•tetraglyme has been the starting point, as preliminary MOCVD results confirm, to yield, through an accurate optimization of the operative parameters, reproducibly and selectively the synthesis of the pure KYF₄ phase. Structural, morphological, and compositional characterization of the films shows the formation of polycrystalline thin films with a very uniform surface.

2.4.1 Experimental section

The KY(hfa)₄•tetraglyme adduct synthesis finds counterparts in the route previously considered by Battiato et al. [28] for the analogous NaY(hfa)₄•tetraglyme complex. The precursor has been prepared by the reaction of Y(NO₃)₃•6H₂O (1,34 gr; 3.52×10⁻³ mol) and KOH (0,98 gr; 1.75×10⁻² mol) suspended in dichloromethane (60 ml) with tetraglyme (0.770 ml, 3.52×10⁻³ mol) and H-hfa (2ml, 1.41×10⁻² mol). The mixture was refluxed, under stirring, for 90 min. The solution was collected by filtration under vacuum and the excess of KOH and Y(NO₃)₃•6H₂O was filtered off. White crystals

were obtained upon evaporation of the solvent, were washed two times in pentane and recovered by filtration. The films were deposited on Si(100) under low-pressure in a horizontal hot-wall reactor, in the 450–500 °C temperature range. The complex was vaporized in the 150°C-180°C temperature range, for an efficient vaporization without thermal degradation. Heating rates of 40 and 8 °C min⁻¹ were used for the reactor chamber and the vaporization reservoir, respectively. Argon was used as a carrier gas, while oxygen as the reactant gas was introduced in the main flow into close proximity to the reaction zone, with a constant flow of 200 ml/min.

Film structure was analyzed by XRD in glancing incidence mode (0.5°) using a Bruker D5005 diffractometer. Film morphology was analyzed by FE-SEM using a ZEISS SUPRA 55 VP field emission microscope. The atomic composition of the complex and deposited film was performed by energy dispersive X-Ray (EDX) analysis using an INCA-Oxford windowless detector, having a resolution of 127 eV as the full width half maximum (FWHM) of the Mn K α .

2.4.2 Synthesis and characterization of the novel KY(hfa)₄•tetraglyme

The KY(hfa)₄•tetraglyme adduct has been prepared through a one-step reaction from the potassium hydroxide, yttrium nitrate, Hhfa and tetraglyme ligands in dichloromethane under refluxing for 90 min. After solvent evaporation, the complex appears in the form of white non-hygroscopic crystals that can be handled in air and that show a melting temperature around 59-62 °C. The adduct is anhydrous and soluble in common organic solvents such as ethanol, dichloromethane, acetone. This synthetic strategy produces the product with a high yield (83%) in a single step and low-cost route.

Given the nominal stoichiometry and the thermal properties analogous to the [Y·(hfa)₄]⁻ [Na·tetraglyme]⁺ adduct, it is likely that the present complex has an ionic structure in which the yttrium is complexed by four β -diketonate hfa⁻ and the potassium is complexed by the tetraglyme, according to the following structure

[Y·(hfa)₄][K·tetraglyme]⁺. A definitive proof could be given by single crystal X ray diffraction characterization, which is under course.

The FT-IR transmittance spectrum (fig. 15a) of the KY(hfa)₄•tetraglyme shows the peaks at 1674 cm⁻¹ and at 1560 associated with C=O stretching and C=C stretching respectively, due to the β-diketonate ligand. The bands at 1014, 862 and 837 cm⁻¹ can be associated with glyme modes. In addition C-H glyme stretching modes, lying in the 2800-3000 cm⁻¹ range, overlap with nujol features. In fact, the nujol shows peaks at 2923 cm⁻¹, at 1461 cm⁻¹ and at 1377 cm⁻¹. The broad band observed in the 1000-1300 cm⁻¹ range may be associated with absorptions of the polyether C-O bending and/or stretching overlapped with the C-F stretching. The small bands around 3500 cm⁻¹ range indicates the presence of coordinated water molecules, which probably saturates the potassium coordination sphere.

In regard to thermal behavior of this bimetallic precursor, differential scanning calorimetric data (fig. 15b) in atmospheric pressure (10°C/min under N₂) shows one endothermic peak at 60 °C, due to the melting of the adduct, while the exothermic peak at a higher temperature at 264°C, is likely due to exothermic processes associated with the ligand losses.

The characterization of mass transport properties behavior of the precursor, carried out in atmospheric pressure thermal gravimetric analysis (TGA, 5°C/min under N₂), reveals that the weight loss takes place in a single step, in the 245-255°C range, with a residue of about 16 % at 350 °C (fig. 15c). This weight loss may be associated with the decomposition of the adduct that loses both the hfa and the tetraglyme ligands leaving KF and YF₃ residue (theoretical value of the residue of 16.8%). The evaluation of complex thermal stability at different temperatures has been carried out through isothermal thermogravimetric measurements in the 150-190°C range for a total duration of 60 min (fig. 15d). These data point to a mass loss that is linearly dependent on vaporization time in the range 150-170°C, excluding secondary phenomena. At highest temperature, the observed non-linear behavior suggests a partial decomposition under atmospheric pressure.

Energy dispersive X-ray (EDX) analysis (fig. 16) established the quantitative crystals composition in various sites in term of metal ratio. The EDX spectrum of the adduct shows the typical $L\alpha$ line of the Y, and the $K\alpha$ and $K\beta$ lines of the K. The presence of the ligand is confirmed to the F $K\alpha$ peak at 0.670 keV, the peak at 0.520 keV associated with the O $K\alpha$, and the K α peak at 0.525 keV due to the presence of the C. The quantitative analysis confirm the correct stoichiometry for the $KY(hfa)_4 \cdot tetraglyme$ adduct with a K:Y ratio of 0,85 : 1.

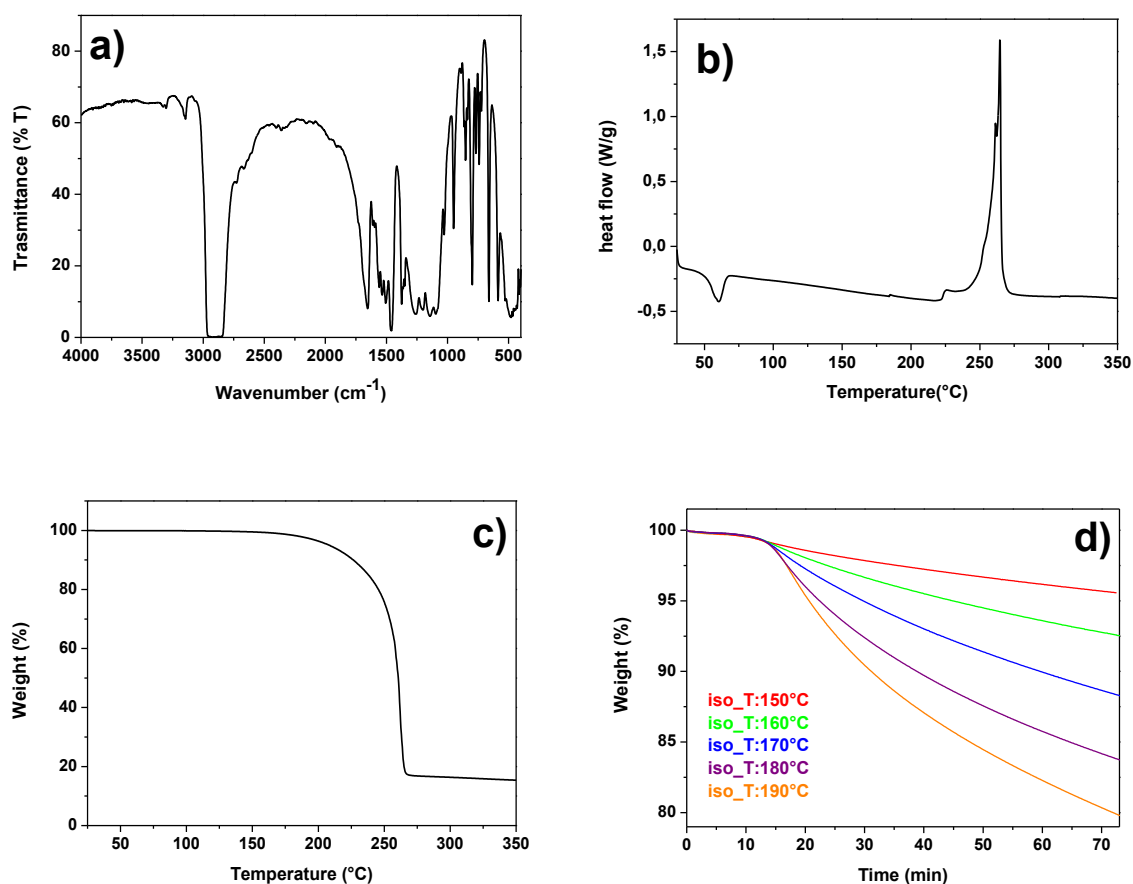


Fig. 15 a) FT-IR transmittance spectrum; b) DSC curve; c) TGA curve; d) isothermal thermogravimetric curves in the 150-190 $^{\circ}C$ range of the $KY(hfa)_4 \cdot tetraglyme$ adduct.

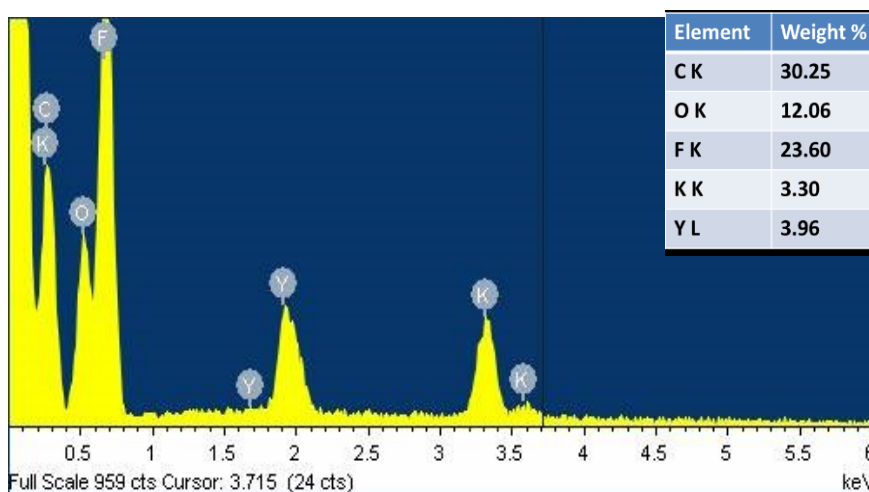


Fig. 16 EDX spectrum of KY(hfa)₄•tetraglyme crystals.

2.4.3 KYF₄ MOCVD synthesis: results and discussion

XRD analysis

The X-ray diffraction (XRD) analysis of the samples deposited on Si (100) for 60 min at different vaporization temperature of precursor source (T_{vap1} :170°C and T_{vap2} :180°C) and different deposition temperature (T_{dep} : 450-500°C) exhibit patterns associated with different kind of fluoride and oxyfluoride phases (fig. 17).

Sample obtained at T_{vap1} :170°C and at T_{dep} : 450°C (fig. 17a) shows pattern associated with the YF₃ phase, according to the ICDD N.05-0546 and confirmed by the EDX analysis, which confirm the presence of Y, F and Si peaks and the absence of K and O signals. Whereas, XRD pattern recorded for sample obtained at T_{vap1} :170°C and at T_{dep} : 500°C (fig. 17a) shows pattern associated with the YOF phase, according to the ICDD N.38-0746 and confirmed by the EDX analysis, which confirm the presence of Y, F, O and Si peaks and the absence of K signal.

The patterns of samples obtained on Si (100) for 60 min at T_{vap2} :180°C and at T_{dep} : 450°C and 500°C are reported in fig. 17b and show peaks at 2θ values of 21.85°, 26.85°, 31.14°, 40.80°, 44.55° and 52.94° associated with the 111, 111, 200, 224, 220, and 311 reflections, respectively, of the KYF₄ (ICDD27-0466).

These data could be interpreted considering a delicate balance between kinetic and thermodynamic contribution, that allow the stabilization of a pure KYF_4 phase only under controlled condition. In addition, the oxygen flow, fixed at 200 ml/min and introduced into the reaction during the depositions zone as the reactant gas, could have effect in the decomposition process of the precursor and in the oxide-fluoride formation. For this reason other deposition processes in which the oxygen flow has been modified are under course to establish its effect on the film composition.

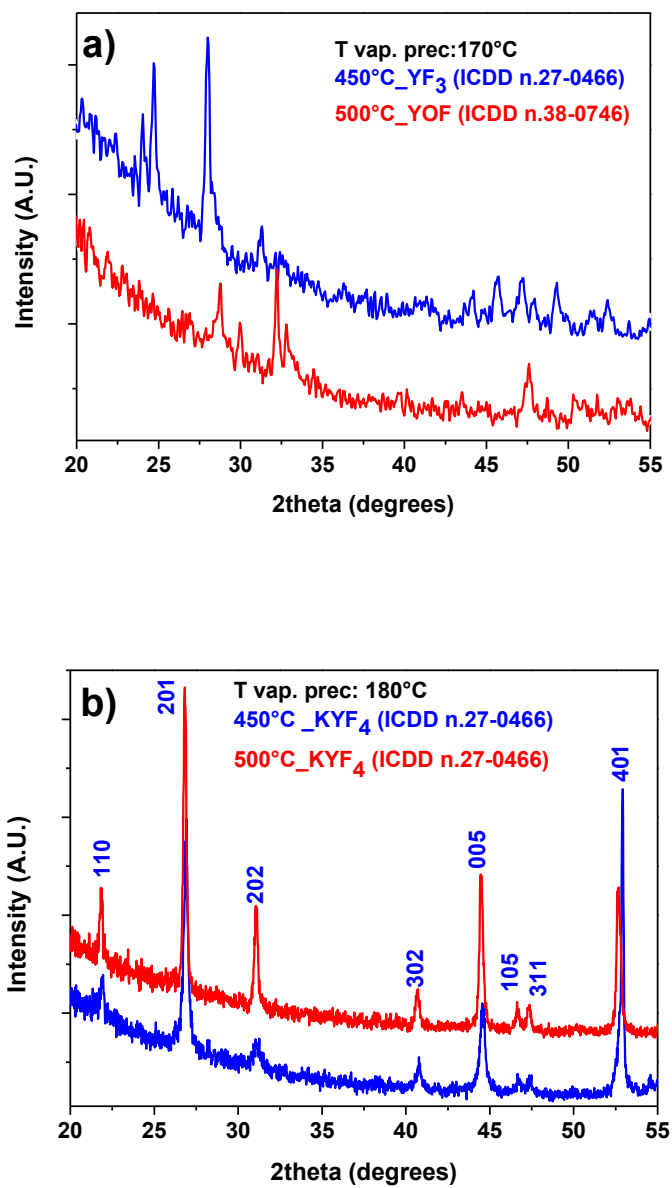


Fig. 17 XRD patterns of films grown on Si(100) for 60min with T_{dep} : 450-500°C and at **a)** $T_{\text{vap}1}$:170°C, and **b)** $T_{\text{vap}2}$:180°C.

FE-SEM characterization

Microstructure and morphology of different kind of films (YF_3 , YOF and KYF_4) have been studied by field emission scanning electron microscopy (FE-SEM). SEM images show different morphologies in relation with the phase and the setting temperatures. The FE-SEM image of the YF_3 film deposited on Si (100) (T_{vap1} :170°C and T_{dep} : 450°C) in fig. 18a shows a homogeneous and uniform nanostructured deposit with very small crystalline grains. Films obtained under the same condition at higher T_{dep} : 500°C (fig. 18b) do not have an homogeneous surface, with elongated grains having different shapes and dimensions. Differently, the films deposited on Si (100) at T_{vap2} :180°C show a very compact and smooth surface for the KYF_4 film at T_{dep} : 450°C (fig. 18c); and a uniform and nanostructured deposit with a plate grains of about 100nm for the KYF_4 film at T_{dep} : 500°C (fig. 18d).

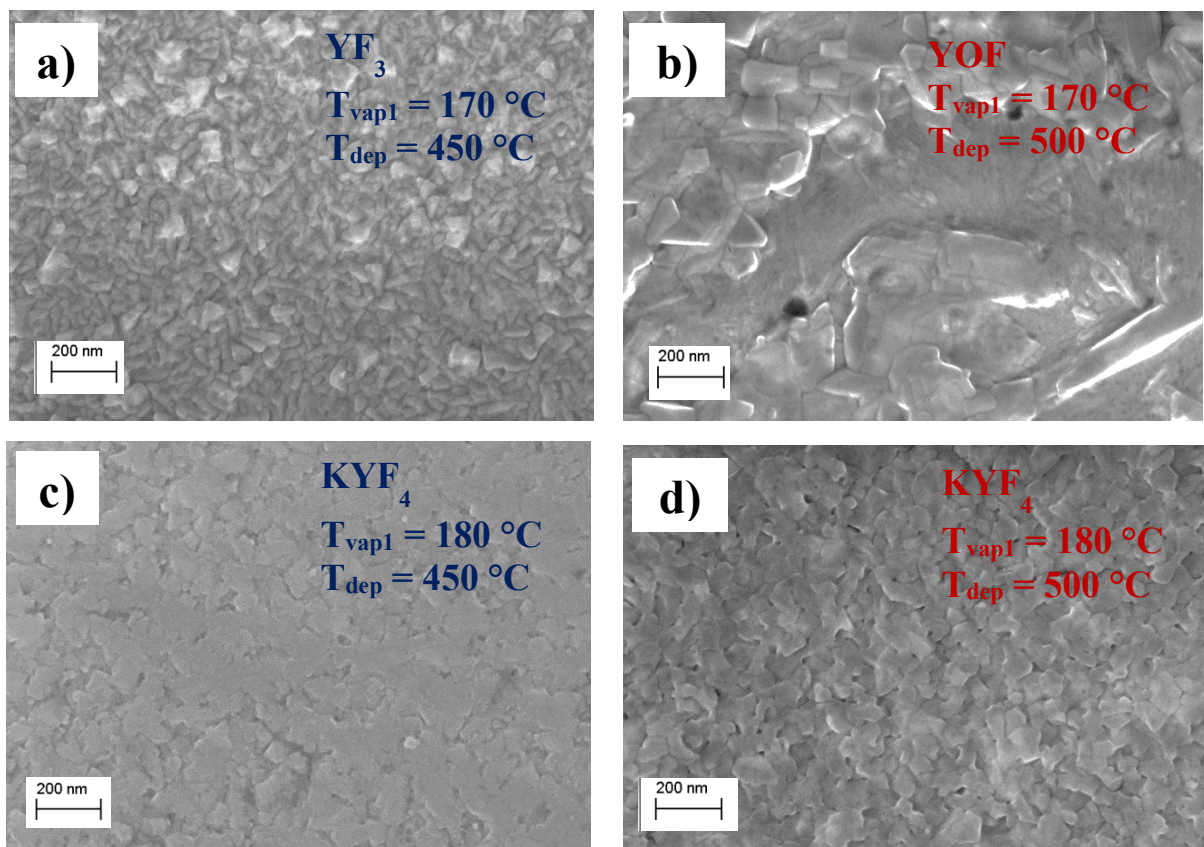


Fig. 18 FE-SEM images of the samples deposited on Si(100) at T_{vap1} :170°C and **a)** T_{dep} :450°C and YF_3 phase; **b)** T_{dep} :500°C and YOF phase; and at T_{vap2} :180°C and **c)** T_{dep} :450°C and KYF_4 phase; **d)** T_{dep} :500°C and KYF_4 phase.

2.5 Conclusion

In summary, a simple MOCVD process has been applied to the fabrication of doped CaF₂ based films, using the M(hfa)_n•diglyme complexes, which act as single-source precursors for the metal component, the doping ions and the fluorine. The deposited films are pure CaF₂ with highly homogeneous surfaces. Depending on the substrate nature further optimization may be needed to avoid cracking on Si substrates. The films show promising up conversion properties in the visible and near-infrared regions upon laser excitation for both Yb³⁺/Er³⁺ and Yb³⁺/Tm³⁺ doping mixtures.

The β-NaYF₄ thin films have been synthesized through MOCVD approach as well. A novel Na-Y precursor, provided by Battiato et al. [28], has been the starting point for MOCVD process and the preliminary results show that: at temperatures up to 400 °C only the cubic structure is obtained, and at temperature of 500°C only the hexagonal phase has been obtained. At the temperature of 450 °C the position of the substrates has a crucial role. These data can be explained considering a balance between thermodynamic and kinetic factors.

Finally, MOCVD method has been successfully applied for the fabrication of KYF₄ nanostructured thin films using the novel fluorinated “third-generation” bimetallic precursor KY(hfa)₄•tetraglyme. The adduct has been synthesized through a one-step reaction with a high yield and characterized by FT-IR, EDX, DSC and TGA. The preliminary results confirm that the MOCVD approach yields reproducibly and selectively the synthesis of the pure KYF₄ phase; these final goals have been achieved through an accurate optimization of the operative parameters, such as the deposition temperature and the vaporization temperature of the precursors.

The X-ray diffraction (XRD) analysis confirms that the MOCVD synthetic approach yields reproducibly and selectively the doped CaF₂, KYF₄ and β-NaYF₄ phase without any impurity phases. Field-emission scanning electron microscopy (FE-SEM) images indicate that morphology surfaces, grain dimensions and thickness are strongly related to the processing parameters.

Finally, the present MOCVD approach is very challenging also in view of its easy scalability, which makes it very attractive for industrial scaling up. This synthetic strategy paves the way for the synthesis of other fluoride phases in thin film forms for up or also down conversion luminescence.

References

- [1] M. Quintanilla, I. X. Cantarelli, M. Pedroni, A. Speghini, F. Vetrone, J. Mater. Chem. C 2015, 3, 3108.
- [2] M. Back, R. Marin, M. Franceschin, N. Sfar Hancha, F. Enrichi, E. Trave, S. Polizzi, J. Mater. Chem. C 2016, 4, 1906.
- [3] P. Dolcet, A. Mambrini, M. Pedroni, A. Speghini, S. Gialanella, M. Casarin, S. Gross, RSC Adv. 2015, 5, 16302.
- [4] B. Ritter, P. Haida, F. Fink, T. Krahl, K. Gawlitza, K. Rurack, E. Kemnitz, Dalton Trans. 2017, 46, 2925.
- [5] N. N. Dong, M. Pedroni, F. Piccinelli, G. Conti, A. Sbarbati, J. E. Ramirez-Hernandez, L. M. Maestro, M. C. Iglesias-de la Cruz, F. Sanz-Rodriguez, A. Juarranz, F. Chen, F. Vetrone, J. A. Capobianco, J. G. Sole, M. Bettinelli, D. Jaque, A. Speghini, ACS Nano 2011, 5, 8665.
- [6] F. K. Ma, Q. Zhang, D. P. Jiang, L. B. Su, Y. J. Shao, J. Y. Wang, F. Tang, J. Xu, P. Solarz, W. Ryba-Romanowski, R. Lisiecki, B. Macalik, Laser Phys. 2014, 24, 105703.
- [7] S. W. Hao, L. M. Yang, H. L. Qiu, R. W. Fan, C. H. Yang, G. Y. Chen, Nanoscale 2015, 7, 10775.
- [8] S. Normani, A. Braud, R. Soulard, J. L. Doualan, A. Benayad, V. Menard, G. Brasse, R. Moncorge, J. P. Goossens, P. Camy, CrystEngComm 2016, 18, 9016
- [9] V. Mahalingam, K. N. K. B. Adusumalli, M. Koppsetti, J. Mater. Chem. C 2016, 4, 2289.
- [10] W. Y. Yin, G. Tian, W. L. Ren, L. Yan, S. Jin, Z. J. Gu, L. J. Zhou, J. Li, Y. L. Zhao, Dalton Trans. 2014, 43, 3861.

- [11] G. Wang, Q. Peng, Y. Li, *J. Am. Chem. Soc.* 2009, 131, 14200.
- [12] N. J. Dudley, *J. Vac. Sci. Technol., A* 1998, 16, 615.
- [13] N. Marechal, E. Quesnel, P. Juliet, Y. Pauleau, *J. Appl. Phys.* 1993, 74, 5203.
- [14] a) M. Ylilampi, T. Ranta-aho, *J. Electrochem. Soc.* 1994, 141, 1278; b) T. Pilvi, K. Arstila, M. Leskela, M. Ritala, *Chem. Mater.* 2007, 19, 3387.
- [15] E. Daran, R. Legros, P. Pernas, C. Fontaine, *J. Appl. Phys.* 1997, 81, 679.
- [16] C. Deiter, M. Bierkandt, A. Klust, C. Kumpf, Y. Su, O. Bunk, R. Feidenhans'l, J. Wollschläger, *Phys. Rev. B* 2010, 82, 085449.
- [17] T. Jiang, W. Qin, F. Ding, *J. Nanosci. Nanotechnol.* 2010, 10, 2013.
- [18] A. V. Blednov, O. Yu Gorbenko, S. V. Samoilenkov, V. A. Amelichev, V. A. Lebedev, K. S. Napol'skii, A. R. Kaul, *Chem. Mater.* 2010, 22, 175.
- [19] G. Malandrino, I. L. Fragalà, *Coord. Chem. Rev.* 2006, 250, 1605.
- [20] A. M. Makarevich, P. P. Semyannikov, N. P. Kuzmina, *Russian J. Inorg. Chem.* 2010, 55, 1940.
- [21] N. P. Kuzmina, D. M. Tsybarenko, I. E. Korsakov, Z. A. Starikova, K. A. Lysenko, O. V. Boytsova, A. V. Mironov, I. P. Malkerova, A. S. Alikhanyan, *Polyhedron* 2008, 27, 2811.
- [22] A. Valore, E. Cariati, S. Righetto, D. Roberto, F. Tessore, R. Ugo, I. L. Fragalà, M. E. Fragalà, G. Malandrino, F. De Angelis, L. Belpassi, I. Ledoux-Rak, K. Hoang Thi, J. Zyss, *J. Am. Chem. Soc.* 2010, 132, 4966.
- [23] R. D. Shannon, *Acta Crystallogr. Sect. A* 1976, 32, 751.
- [24] J. Zhou, Q. Liu, W. Feng, Y. Sun, F. Li, *Chem. Rev.* 2015, 115, 395.
- [25] A. M. Makarevich, A. S. Shchukin, A. V. Markelov, S. V. Samoilenkov, P. P. Semyannikov, N. P. Kuzmina, *ECS Trans.* 2009, 25, 525.
- [26] J. A. Capobianco, F. Vetrone, J. C. Boyer, A. Speghini, M. Bettinelli, *J. Phys. Chem. B* 2002, 106, 1181.
- [27] P. Villanueva-Delgado, K. W. Kramer, R. Valiente, M. de Jong, A. Meijerink, *Phys. Chem. Chem. Phys.* 2016, 18, 27396.

[28] S. Battiato, P. Rossi, P. Paoli and G. Malandrino, *Inorg. Chem.* 2018, <http://dx.doi.org/10.1021/acs.inorgchem.8b02267>.

[29] N.C.Dyck, F.C.vanVeggel, G.P.Demopoulos , *Appl. Mater. Interfaces* 2013, 5, 11661–11667.

CHAPTER 3

Sol-gel approach to the fabrication of Ln³⁺ doped fluoride thin films

In the present investigation, an innovative sol-gel process has been optimized to produce up-converting and down converting Ln³⁺doped β -NaREF₄ thin films (Ln: Eu³⁺, Yb³⁺, Tm³⁺, Er³⁺ and RE: Gd, Y), using a mixture of a novel β -diketonate “second generation” sodium precursor, the Na(hfa)•tetraglyme [1], and a well-known rare earth precursors, the RE(hfa)₃•diglyme (RE=Y, Gd, Eu, Yb, Tm, Er; Hhfa = 1, 1, 1, 5, 5, 5 - hexafluoro - 2, 4 - pentanedione; tetraglyme = 2, 5, 8, 11, 14 - Pentaioxapentadecane; diglyme = 2- Methoxyethyl ether) [2]. In addition, the sol gel procedure has been successfully tested for the synthesis of Ln³⁺ doped YOF thin film. The Na(hfa)•tetraglyme and M(hfa)₃•diglyme (M = Y, Gd, Eu, Yb, Tm, Er) complexes act as single sources of metals and fluorine.

The effects of molar ratio of the precursors, aging time of sol and annealing treatment have been explored in the evolution of thin films composition, microstructural features and morphology. In addition, the up-conversion (UC) emission properties of Ln³⁺ co-doped β -NaREF₄ have also been investigated.

3.1 Introduction

Great efforts were made in the last years to investigate energy converting (EC) nanomaterials [3]. Up converting materials (UC) have the interesting property of generating emission at energies higher than the exciting radiation, in particular in the

near infrared (NIR) and visible regions. On the contrary, down converting materials (DC) have the property of generating emission at energies lower than the exciting radiation. These peculiar properties and the possibility of preparation of nanosized structures, have attracted a great attention for applications of these materials in modern technological fields, such as in solar cells [4] and nanomedicine [5]. Very recently UC nano- or microsized materials have been revealed to be also interesting for non-contact, high spatial resolution, optical thermometry [6].

Lanthanide (Ln) ions as dopants in EC materials are able to generate luminescence covering the ultraviolet (UV), visible and NIR spectral ranges [7], that can be easily tuned by a proper choice of the Ln ions and their concentration.

On the other hand, the choice of an appropriate host, accommodating the luminescent ions, is of paramount importance, and for this reasons fluorides are very interesting hosts due to their low phonon energies and therefore reduced multiphonon relaxation processes for the Ln excited states [8,9].

In particular, hexagonal phases NaGdF_4 and NaYF_4 , suitably co-doped with $\text{Yb}^{3+}/\text{Er}^{3+}$, $\text{Yb}^{3+}/\text{Tm}^{3+}$ or Eu^{3+} ions, have been proved as ones of the most promising and efficient EC materials [10-14], more efficient than the cubic phase. Hexagonal phase NaYF_4 has been prepared in form of nanocrystals [15-16] and nanocomposites [17-18] or self-assembled nanoparticles on Si substrate [19]. Nevertheless, applications of the EC NaYF_4 phase in solar cells, solid state lasers or in microelectronics, require the use of material in thin film form. In the literature only few reports have appeared about the preparation and characterization of co-doped Ln activated NaYF_4 thin films [20].

In the present work the simple and innovative sol-gel/spin-coating route has been developed for the reproducible and phase-selective synthesis of Ln-doped $\beta\text{-NaYF}_4$ and Ln-doped $\beta\text{-NaGdF}_4$ nanostructured thin films. This final goal has been achieved through an accurate optimization of the operative parameters such as molar ratio of the precursor mixture, aging time of sol, spin coating procedure and annealing temperatures.

In addition, this approach has been tested for rare earth oxyfluorides YOF:Ln^{3+} synthesis. The oxyfluorides materials are promising hosts for preparation of phosphors and also for combining multi-color DS and UC emissions due to their attractive chemical and physical properties which may be classified as in between characteristics of fluorides and oxides [21]. Alike fluorides, oxyfluorides have low phonon energy, high refractive index, and high ionicity which leads to the efficient luminescence, in addition, these compounds have great chemical and thermal stabilities which resemble properties of oxides [22].

3.2 Ln^{3+} doped $\beta\text{-NaYF}_4$ thin films: Sol-gel fabrications and their luminescent properties

A novel sol-gel and spin-coating approach has been carried out to synthesize Yb^{3+} , Er^{3+} and Yb^{3+} , Tm^{3+} codoped NaYF_4 nanostructured thin films using the fluorinated “second-generation” β -diketonate compounds $\text{Na}(\text{hfa})\text{tetraglyme}$ and $\text{Ln}(\text{hfa})_3 \bullet \text{diglyme}$ ($\text{Ln} = \text{Y, Er, Tm, Yb}$).

The novel $\text{Na}(\text{hfa}) \bullet \text{tetraglyme}$ adduct has been synthesized through a one-step reaction with a high yield in the form of white non-hygroscopic crystals. The adduct was characterized by single crystal X-ray diffraction, infrared spectroscopy (FT-IR), Nuclear magnetic resonance spectroscopy ($^1\text{H-NMR}$, $^{13}\text{C-NMR}$), differential scanning calorimetry analysis (DSC) and thermogravimetric analysis (TGA).

Afterward a systematic study has been carried out to optimize the fluoride phase formation with the correct stoichiometry and a uniform and nanostructured morphology. Structural, morphological and compositional characterizations of the films, carried out through X-ray diffraction, field emission scanning electron microscopy and energy dispersive X-ray analysis, respectively, show the formation of polycrystalline NaYF_4 film with a very uniform surface and rounded grains with average size of 200 nm. Spectroscopic properties in the visible and near infrared regions upon laser excitation at 980 nm have been investigated.

3.2.1 Experimental section

The sol-gel reaction occurred in water/ethanol solution of Na(hfa)•tetraglyme, Y(hfa)₃•diglyme and Ln(hfa)₃•diglyme, with Ln = Yb, Tm, for co-doped films. The Na(hfa)•tetraglyme adducts has been prepared according to the procedure reported in ref. [1] by the reaction of NaOH (1.47 gr; 7.07×10⁻³ mol) suspended in dichloromethane (30 ml) with tetraglyme (1.55 g, 7.07×10⁻³ mol) and H-hfa (1.470 g, 7.07×10⁻³ mol). The mixture was refluxed, under stirring, for 1 h. The solution was collected by filtration under vacuum and the excess of NaOH was filtered off. White crystals were obtained upon evaporation of the solvent, were washed two times in pentane and recovered by filtration.

The Ln(hfa)₃•diglyme complexes were synthesized as previously reported in ref. [23-24]. For the sol hydrolysis, trifluoroacetic acid (CF₃COOH) was used as catalyst and different molar ratio of precursors, solvent and catalyst were tested. The sol was aged at 60°C in a time range from 6 h to 20h and spin-coated on Si(100) and quartz substrates. The spin-coating process was carried out using a Spin-Coater SPIN-150 SPS Europe, at 3000 round per minute (RPM), time of 60s and speed rate of 1000 RPM/sec. We also tested a new multistep procedure in which spin-coating deposition is alternated to fast annealing steps at 400°C in air for 10 min. After four steps, films were annealed at 400 °C in air for 1h. Film structure was analyzed by X-ray diffraction (XRD) in grazing incidence mode (0.5°) using a Smartlab Rigaku diffractometer, equipped with a rotating anode of Cu K α radiation operating at 45 kV and 200 mA. Film surface morphology was investigated using the field emission scanning electron microscope, ZEISS Supra 55 VP. The atomic composition of the sample was performed by energy dispersive X-Ray (EDX) analysis. For the luminescence measurements, a 980 nm diode laser, in continuous or pulsed modes, was used as the radiation source (CNI Optoelectronics Tech). The emission spectra were recorded with a half meter monochromator (Andor, Shamrock 500i) equipped with a 1200 lines/mm grating and an iDus CCD camera. The optical resolution of the

spectra is 0.1 nm. The luminescence lifetimes were acquired with a Hamamatsu R928 photomultiplier tube connected to a 500 MHz digital oscilloscope (LeCroy, WaveRunner LT342). All the spectroscopic measurements were collected at room temperature.

3.2.2 Synthesis and characterization of a novel Na(hfa)•tetraglyme

The Na(hfa)•tetraglyme adduct has been prepared through a one-step reaction from the sodium hydroxide, Hhfa and tetraglyme ligands in dichloromethane under refluxing for 1 hour. After solvent evaporation, the complex appears in the form of white non-hygroscopic crystals that can be handled in air and that show a melting temperature around 65-68 °C. The adduct is soluble in common organic solvents such as ethanol, dichloromethane, acetone. It is worth noting that this synthetic strategy produces an anhydrous adduct with a high yield (86%) in a single step, low-cost route from commercially available chemicals. The adduct was characterized by means of single crystal X-ray diffraction. In the Na(hfa)•tetraglyme complex, the sodium cation is seven-coordinated by the five oxygen atoms of the ether and by the two oxygen atoms of the hfa anion (fig. 1).

The FT-IR transmittance spectrum (fig. 2) of the Na(hfa)•tetraglyme shows the peaks at 1674 and at 1560 cm^{-1} associated with C=O stretching and C=C stretching respectively, due to the β -diketonate ligand. The broad band observed in the 1000-1300 cm^{-1} range may be associated with absorptions of the polyether C-O bending and/or stretching overlapped with the C-F stretching. In addition, bands at 1015, 861 and 837 cm^{-1} can be associated with glyme modes. The C-H glyme stretching modes, lying in the 2800-3000 cm^{-1} range, overlap with nujol features. In fact, the nujol shows peaks at 2923 cm^{-1} , at 1461 cm^{-1} and at 1377 cm^{-1} . The absence of any bands around 3500 cm^{-1} range confirms the absence of coordinated water molecules, indicating that the Lewis base tetraglyme saturates the metal centre.

The ^1H -NMR and ^{13}C -NMR characterizations (fig. 3a) confirm the formation of the

desired complex; in fact the ^1H NMR spectrum of the $\text{Na}(\text{hfa})\bullet\text{tetraglyme}$ adduct shows two singlet at $\delta=5.08$ and 3.4 ppm due to the one proton of the hfa ligand and to the six equivalent proton of the two methyl groups of the tetraglyme ligand, respectively. In addition to the singlet, the multiplet at $\delta=3.5\text{--}3.7$ ppm represents resonances of methylenic protons of the tetraglyme. The single peak at 7.2 ppm is due to the chloroform.

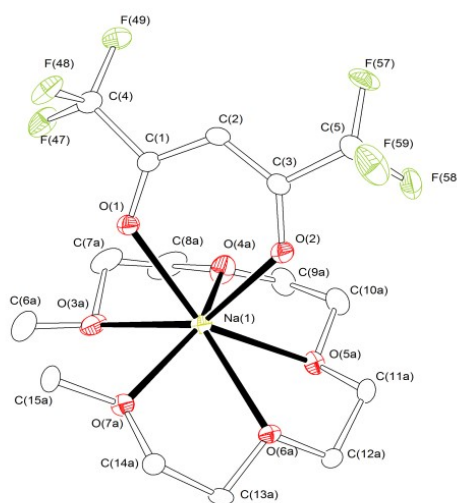


Fig. 1 ORTEP3 view of the $\text{Na}(\text{hfa})\bullet\text{tetraglyme}$ complex (ellipsoids are drawn at 20% probability).

Hydrogen atoms have been omitted for the sake of clarity.

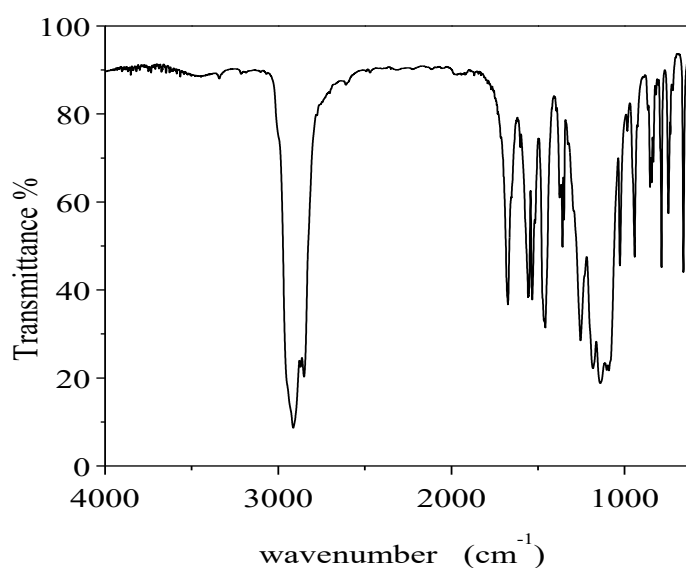


Fig. 2 FT-IR transmittance spectrum of the $\text{Na}(\text{hfa})\bullet\text{tetraglyme}$ adduct.

The ^{13}C NMR spectrum (Fig. 3b) shows resonances at δ 86 ppm, 118 ppm e 176 ppm associated, respectively, with a singlet for the CH groups, a quartet for the CF_3 groups and a quartet for the CO groups of the coordinated hfa ligands. The quartets are due to first order (CF_3 ; $^1J = 284$ Hz) and second order (CO; $^2J = 33$ Hz) coupling with the CF_3 fluorine atoms. Coordinated tetraglyme gives signals at δ 59, due to methylic carbons (s, OCH_3), in the range of δ 69-71 there are the signal due to eight methylenic carbons.

In regard to mass transport properties and thermal behavior of this sodium precursor, atmospheric pressure thermal gravimetric analysis (TGA, $5^\circ\text{C}/\text{min}$ under N_2) reveals that the weight loss takes place in a single step, in the $130\text{-}250^\circ\text{C}$, with a residue of about 9.8 % at 350°C (fig. 4a). This weight loss may be associated with the decomposition of the adduct that loses both the hfa and the tetraglyme ligands leaving a NaF residue (theoretical value of the residue of 9.3%). The differential scanning calorimetric data (fig. 4b) show endothermic peaks at 43°C , likely associated with a solid-solid phase change, and at 67°C due to the melting of the adduct, while the exothermic peak at a higher temperature is likely due to exothermic processes associated with the ligand loss.

The observed thermal features, associated with a high solubility of the adduct in organic solvents, make it particularly attractive for preparation of Na and F containing solid phases with the sol-gel technique. In addition, no complexes are known in the literature as sodium precursors for sol-gel processes.

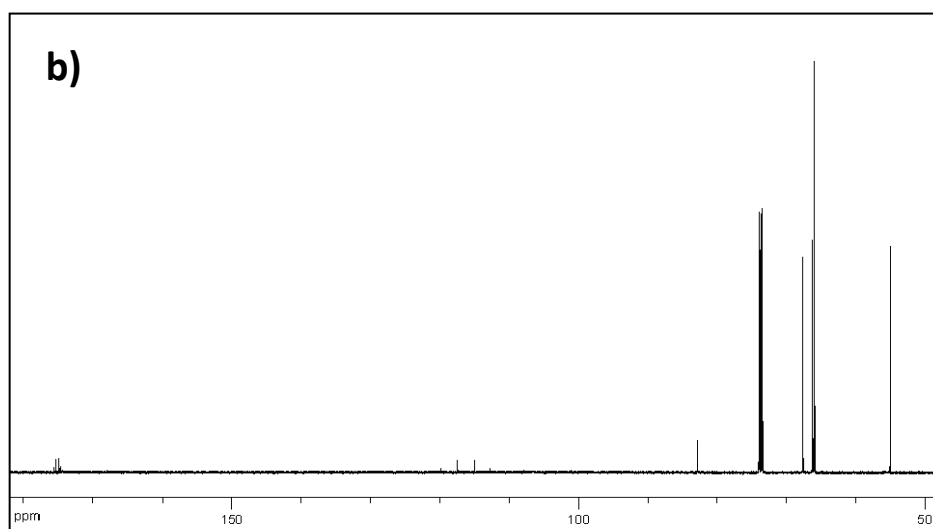
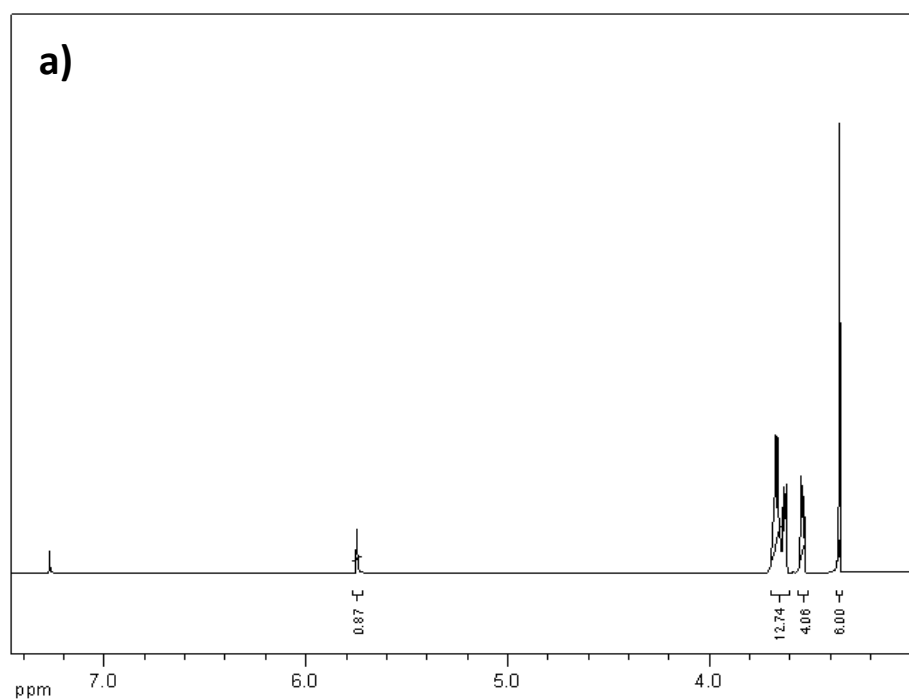


Fig. 3 a) ^1H -NMR, and **b)** ^{13}C -NMR spectra of the $\text{Na}(\text{hfa})\cdot\text{tetraglyme}$ adduct.

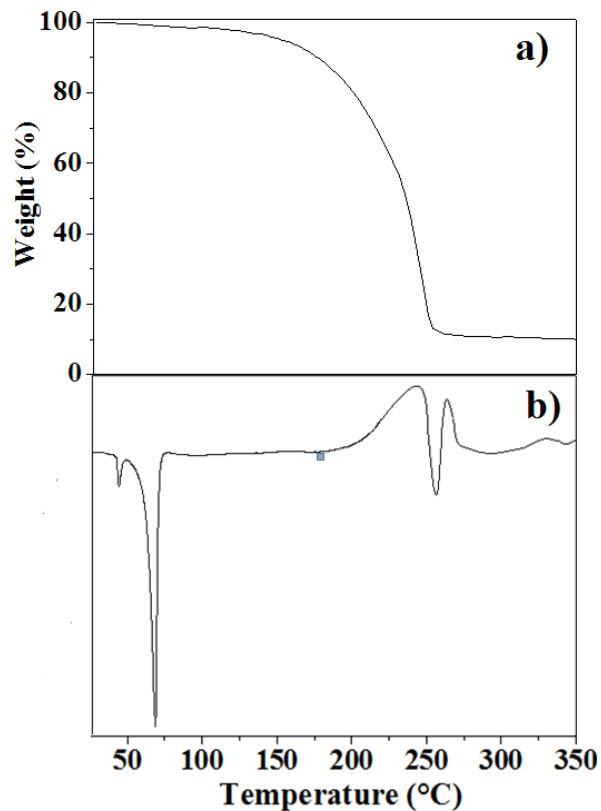


Fig. 4 a) TGA, and b) DSC of the Na(hfa)•tetraglyme adduct.

3.2.3 Optimization of the sol-gel process for the formation of β -NaYF₄ phase films

Present data show that the nature of films strictly depends upon the adopted procedure. The new sol-gel process finds counterparts in the route previously considered by Armelao et al. for the synthesis of luminescent Eu³⁺ doped LaOF thin films [25]. In particular, molar ratios of the mixture and aging time have been shown to be the most important parameters. A scheme of the various routes applied to optimize the formation of the β -NaYF₄ phase is drafted in fig. 5.

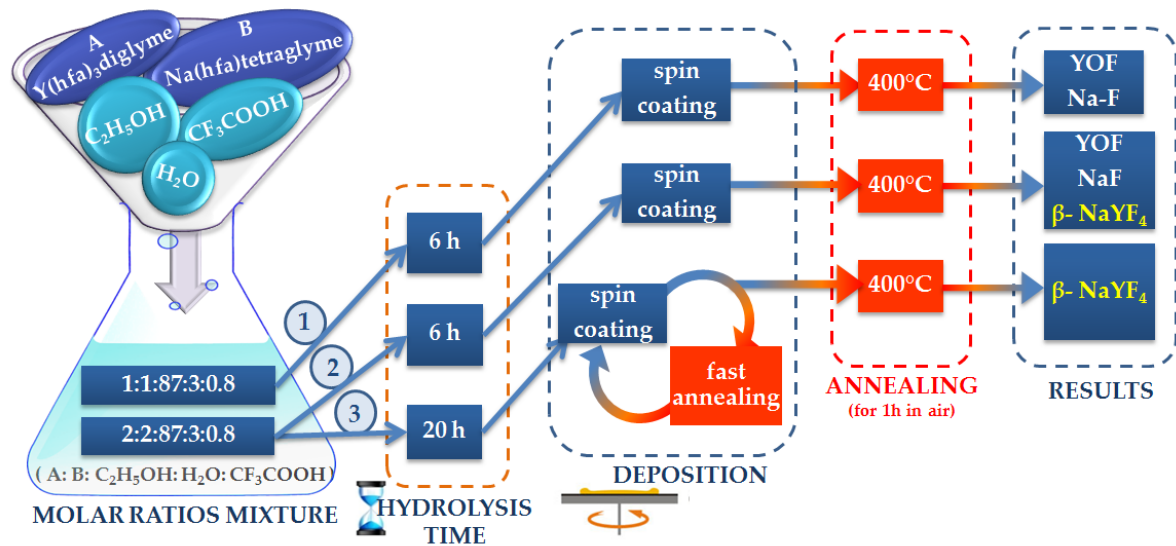
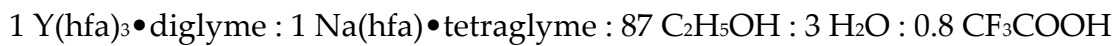


Fig. 5 Scheme of the processes at different molar ratios, aging time and deposition steps.

The first procedure (route 1 in fig. 5) with a $Y(hfa)_3 \bullet diglyme(A) : Na(hfa) \bullet tetraglyme (B)$ ratio of 1:1 :



annealing temperature (T_{ann}) of $400^\circ C$ and hydrolysis time of 6h produces non uniform films containing YOF (ICDD n° 06-0346), as shown in the XRD pattern reported in fig. 6a. The related FE-SEM image (Fig. 6b) shows a homogeneous morphology with elongated grains of about 400 nm due to coalescence of nuclei. This morphology is similar to that observed for the LaOF MOCVD grown films [26]. Nevertheless, the energy dispersive X-Ray (EDX) analyses within the grains and underneath indicate a not homogeneous composition, with different Na:Y ratios in the two positions (fig. 7 and 8). In any case, the presence of Na, confirmed through EDX, points to the formation of an amorphous Na-F phase. In fact, the Na $K\alpha$ peak is observed at 1.06 keV, while the Y L peaks are observed in the 1.8-2.2 range keV. In addition, the windowless EDX detector allowed to detect the F $K\alpha$ peak at 0.670 keV,

and a small peak at 0.520 keV associated with the O K α peak, due to the presence of the YOF. Subsequently, a molar ratio of:



with a T_{ann} of 400 °C and aging time of 6 h has been tested (route 2 in fig. 5), in order to yield a higher density gel with a consequent more uniform film together with the formation of the β -NaYF₄ phase. The XRD pattern of the sample obtained through this procedure (fig. 6c) shows reflections at $2\theta = 30.05, 30.80, 39.65, 43.50, 53.30, 53.75, 55.20^\circ$, associated with those of an hexagonal NaYF₄ structure, in accordance with the ICDD n° 160334. Peaks associated with the YOF phase are also observed. The related FE-SEM image (fig. 6d) shows a heterogeneous morphology with grains of irregular shapes and dimensions ranging from 400 nm to about 600 nm. EDX analyses show different composition in various zones of the film, in which Na and Y are present in different ratios (fig. 9 and 10) and are correlated to the presence of the three phases NaYF₄, amorphous NaF and YOF.

A different procedure (route 3 in fig. 5) has been developed with aging time of 20h and with a new multistep process in which spin coating deposition is alternated to fast annealing step at 400°C in air for 10 min. After four cycles of spinning/10 min-annealing, the sample has been treated at 400°C for 1 h. Under these conditions, the film shows a pure hexagonal phase, as assessed by the XRD pattern (fig. 6e), showing only the peaks associated with the β -NaYF₄ phase. The associated FE-SEM image shows a homogeneous and uniform film over large areas (1× 2 cm) with rounded grains of ≈ 250 nm (fig. 6f). Quantitative EDX analysis confirms the correct stoichiometry for the NaYF₄ phase with a Na:Y ratio of 1.0:0.95 on the whole surface.

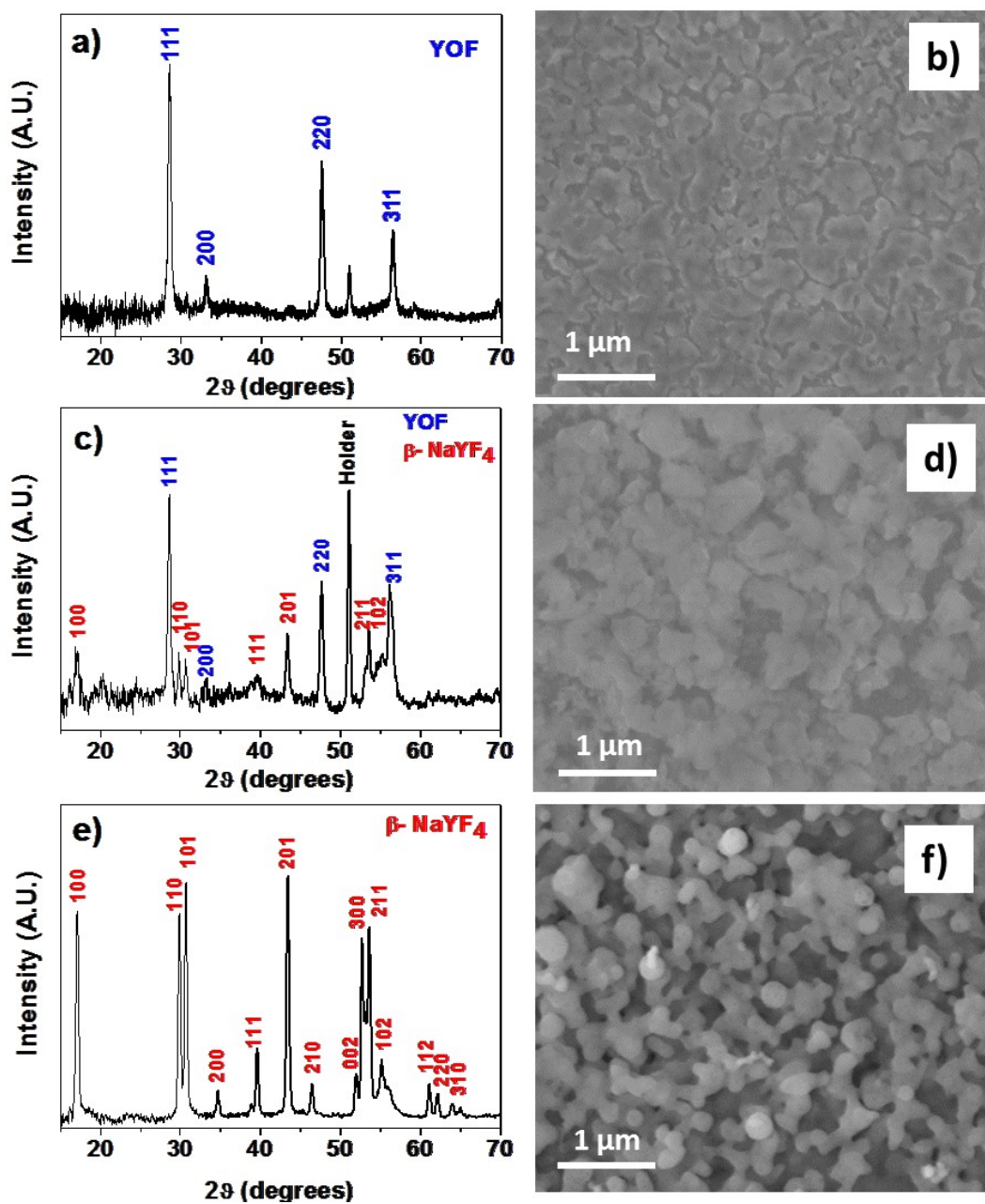


Fig. 6 XRD patterns and FE-SEM images of NaYF_4 films grown on Si (100) under different conditions: route 1, 400°C, 6h, molar ratio 1:1:87:3:08 (a,b); route 2, 400°C, 6h, molar ratio 2:2:87:3:08 (c,d); route 3, 400°C, 20h, molar ratio 2:2:87:3:08 and multistep procedure (e,f).

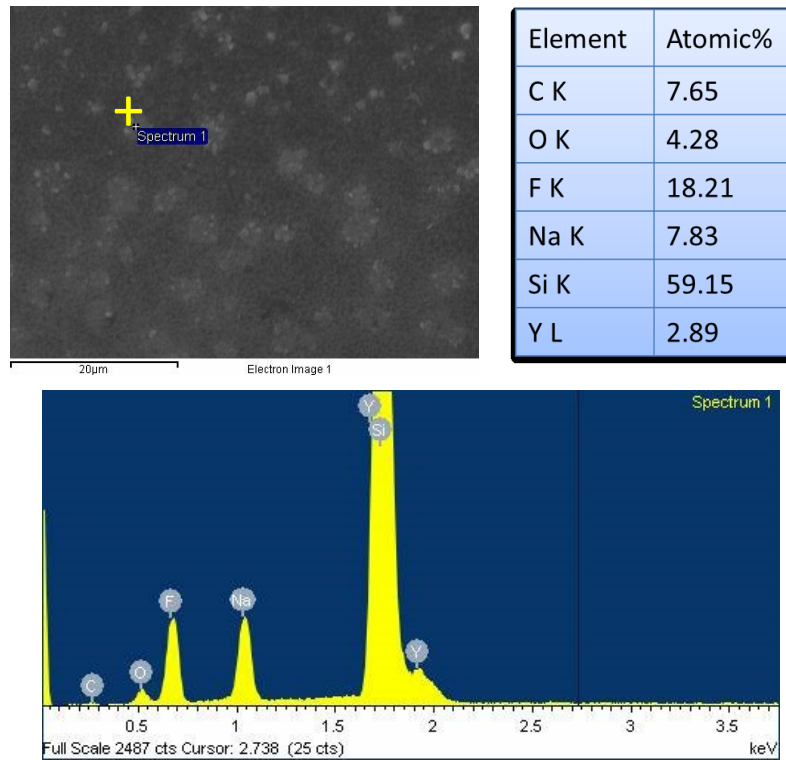


Fig. 7 EDX spectrum recorded in position 1 of the sample obtained through route 1.

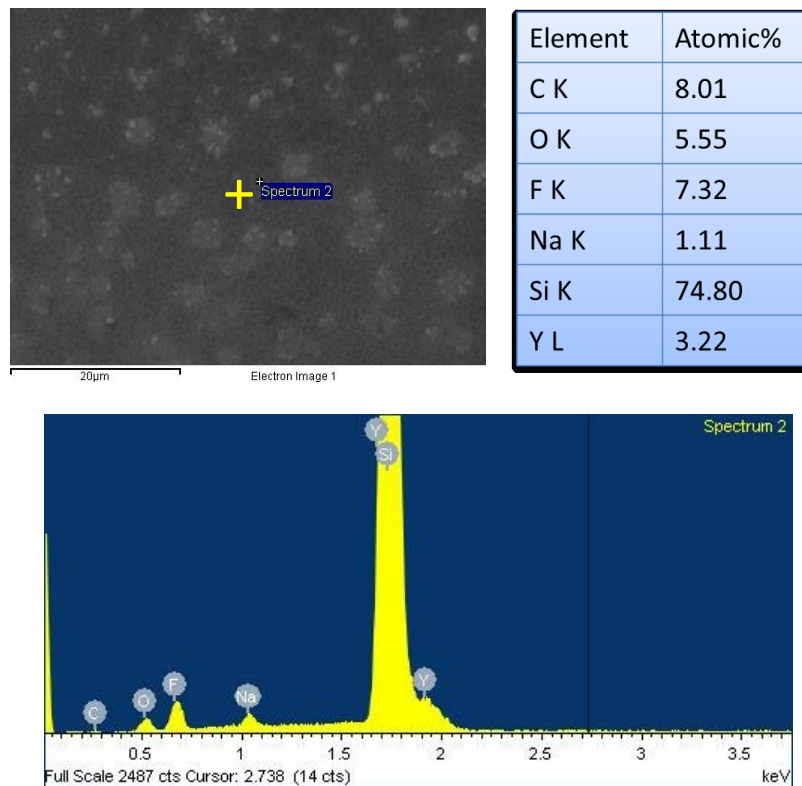


Fig. 8 EDX spectrum recorded in position 2 of the sample obtained through route 1.

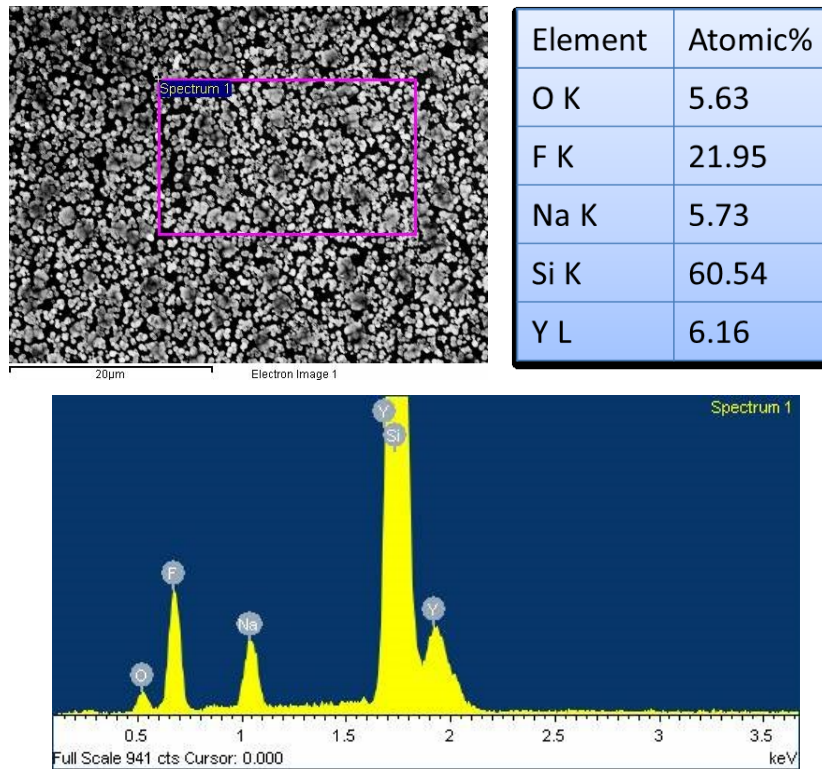


Fig. 9 EDX spectrum recorded on one side of the sample obtained through route 2.

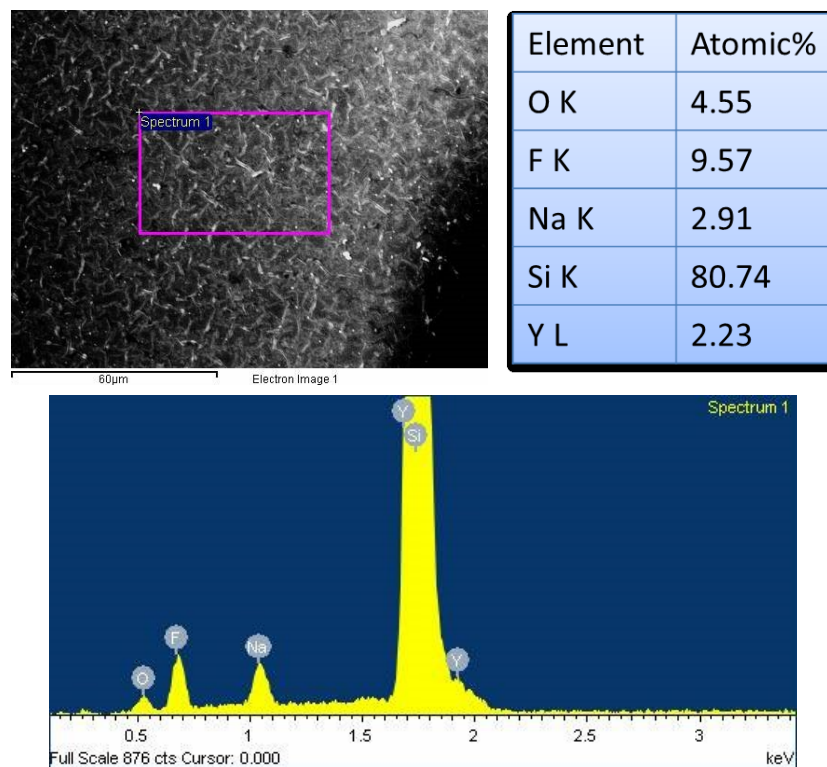


Fig. 10 EDX spectrum recorded on the other side of the sample obtained through route 2.

A comment deserves the comparison between the β -NaYF₄ thin films obtained through sol-gel process and the same material obtained through MOCVD process, described in chapter 2.

The starting point for the MOCVD synthesis of NaYF₄ nanostructured thin films has been the novel fluorinated bimetallic β -diketonate compound, NaY(hfa)₄•tetraglyme precursor. The synthesis has been conducted through an optimization of the operative parameters, such as the deposition temperature and the substrates' positions inside the reactor in order to stabilize the hexagonal structure. The FE-SEM images of the films show a homogeneous surface for all the samples with different morphologies in relation with the α or β phase. The β -NaYF₄ thin films show uniform and smooth surface morphologies with "plate like" grains of about 250 nm (cap.2 fig. 14c,d cap.2) and a thickness of about 500 nm.

Differently, the sol gel synthesis of β -NaYF₄ thin films has been conducted using the fluorinated β -diketonate compounds Na(hfa)tetraglyme and Ln(hfa)₃•diglyme (Ln = Y, Er, Tm, Yb) and an appropriate turning of the molar ratio of the mixture, aging time and spin coating procedure. The films show a pure hexagonal phase, as assessed by the XRD pattern, and the associated FE-SEM images show a homogeneous and uniform film over large areas with rounded grains of \approx 250 nm and a thickness of about 1 μ m.

Both materials show good structural and physical properties as host for lanthanide ions, and luminescent characterization of the new doped β -NaYF₄ thin films obtained through MOCVD route are under course.

3.2.4 Co-doped Yb³⁺/Er³⁺ and Yb³⁺/Tm³⁺ β -NaYF₄ phase thin films

The optimized route, used to produce phase pure hexagonal NaYF₄ films, has been conveyed to the fabrication of co-doped Yb³⁺, Er³⁺ and Yb³⁺, Tm³⁺ β -NaYF₄ thin films. This aim has been easily reached since the nature of the doping ion sources are similar to the Y one, being the Yb(hfa)₃•diglyme, Er(hfa)₃•diglyme and

Tm(hfa)₃•diglyme complexes used as sources of the Yb³⁺, Er³⁺ or Tm³⁺ ions, respectively. The proper amount of dopants, which are strongly connected to the UC efficiency of the β-NaYF₄ systems [27], have been set up at A:1.6, B:2, Yb:0.4, Tm:0.01 ratio in accordance to literature studies [28]. The co-doped NaYF₄ thin films, have the hexagonal phase, as indicated by the XRD pattern reported in fig. 11. The diffractogram has been recorded using graphite as an internal standard to correctly position the pattern peaks. This procedure allowed us to confirm that the peaks of the codoped β-NaYF₄ film correspond perfectly to the peak positions of the undoped β-NaYF₄ phase (ICDD n° 16-0334).

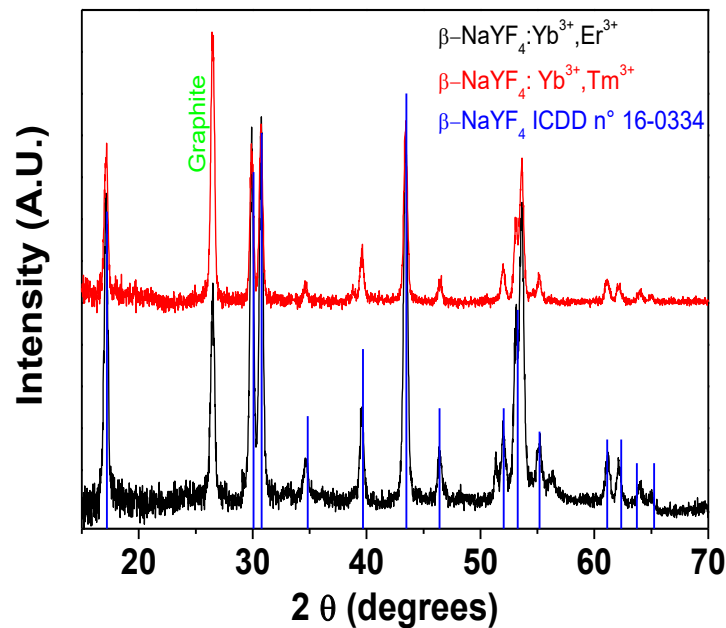


Fig. 11 XRD patterns of NaYF₄:Yb³⁺, Er³⁺ and NaYF₄:Yb³⁺, Tm³⁺ films grown on Si (100).

This is in accordance with the similar ionic radii of the Yb³⁺, Er³⁺ and Tm³⁺ ions of 0.985, 1.004, 0.994 Å, respectively compared to the Y³⁺ ionic radius value of 1.075 Å, all of them taken from the Shannon's table for a nine fold coordination [29]. Actually, Y³⁺, and consequently the Ln³⁺ doping ions, are located in nine coordinated sites of

low symmetry in the β - NaYF_4 phase [30]. The stoichiometry of the co-doped film has been assessed by the energy dispersive X-Ray analysis, whose spectrum (fig. 12) shows the typical peaks of the Na, Y, and Yb elements. In particular, in addition to the Na $K\alpha$ and Y L peaks, the peak due to the Yb $M\alpha$ is observed at 1.6 keV. The absence of a peak at 0.520 keV excludes any O contamination.

No peaks of Er or Tm are present in the EDX spectra due to their low amount, at the limit of the EDX detectability. Quantitative EDX analysis confirms the correct stoichiometry for the $\text{NaYF}_4:\text{Yb}^{3+}, \text{Er}^{3+}$ phase with a Na:Y:Yb ratio of 1.1:0.8:0.2 on the whole surface.

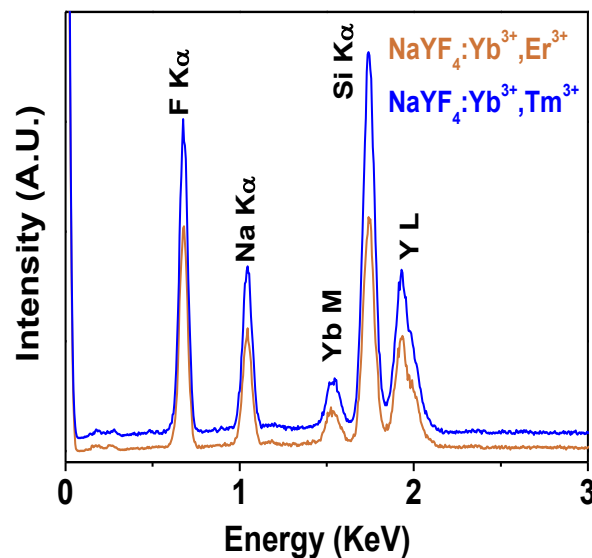


Fig. 12 EDX spectra of the co-doped $\text{NaYF}_4:\text{Yb}^{3+}, \text{Er}^{3+}$ and $\text{NaYF}_4:\text{Yb}^{3+}, \text{Tm}^{3+}$ film grown on Si (100).

The morphologies of the co-doped NaYF_4 films (fig. 13) are similar to the undoped one. FE-SEM plan view images of both the $\text{NaYF}_4:\text{Yb}^{3+}, \text{Er}^{3+}$ (fig. 13a) and $\text{NaYF}_4:\text{Yb}^{3+}, \text{Tm}^{3+}$ films (fig. 13c) indicate the presence of rounded grains of about 200 nm. The cross-sections indicate that the films have a very compact structure with a thickness of about $1\mu\text{m}$ for the $\text{NaYF}_4:\text{Yb}^{3+}, \text{Er}^{3+}$ film (fig. 13b) and of $0.9\mu\text{m}$ for the $\text{NaYF}_4:\text{Yb}^{3+}, \text{Tm}^{3+}$ one (fig. 13d).

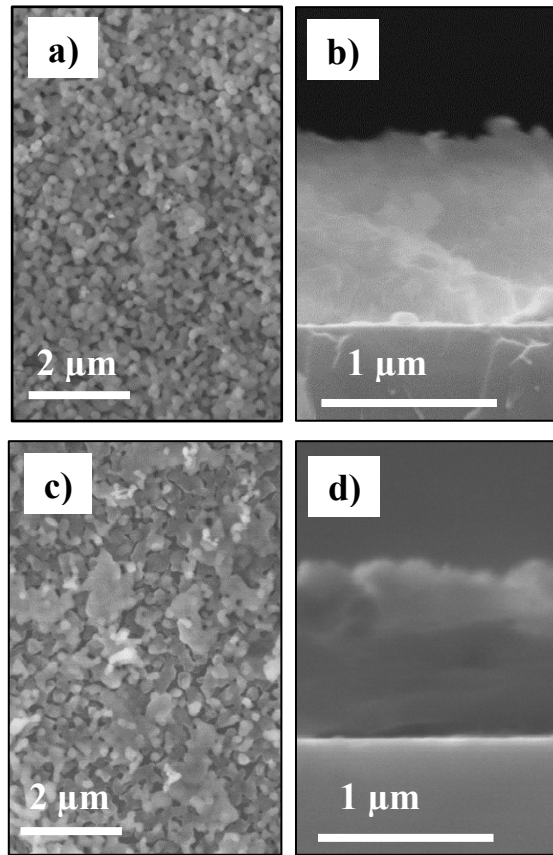


Fig. 13 FE-SEM plan views and cross sections of NaYF₄:Yb³⁺, Er³⁺ (a,b) and NaYF₄:Yb³⁺, Tm³⁺ (c,d) films grown on Si (100).

3.2.5 Upconversion properties and luminescence lifetimes of the co-doped β -NaYF₄: Yb³⁺, Er³⁺ and Yb³⁺, Tm³⁺ films

β -NaYF₄:Yb³⁺, Er³⁺ systems

Figure 14a shows the up-conversion spectrum of the NaYF₄:Er³⁺,Yb³⁺ film upon excitation with a 980nm diode laser. The emission bands in the visible range are typical of the Er³⁺ ion emission. In particular, the bands are assigned as in the following: the two bands in the green region centered at 525 nm and 550 nm are due to $^2H_{11/2} \rightarrow ^4I_{15/2}$ and $^4S_{3/2} \rightarrow ^4I_{15/2}$ electronic transitions, respectively. The band in the red region, centered at 660 nm, is due to the $^4F_{9/2} \rightarrow ^4I_{15/2}$ transition.

Due to the high percentage of the Yb^{3+} ions with respect to the total metal content, the main mechanism of the up-conversion process is most probably Energy Transfer Up-conversion (ETU), as found for similar systems [31], as also described in fig. 14b.

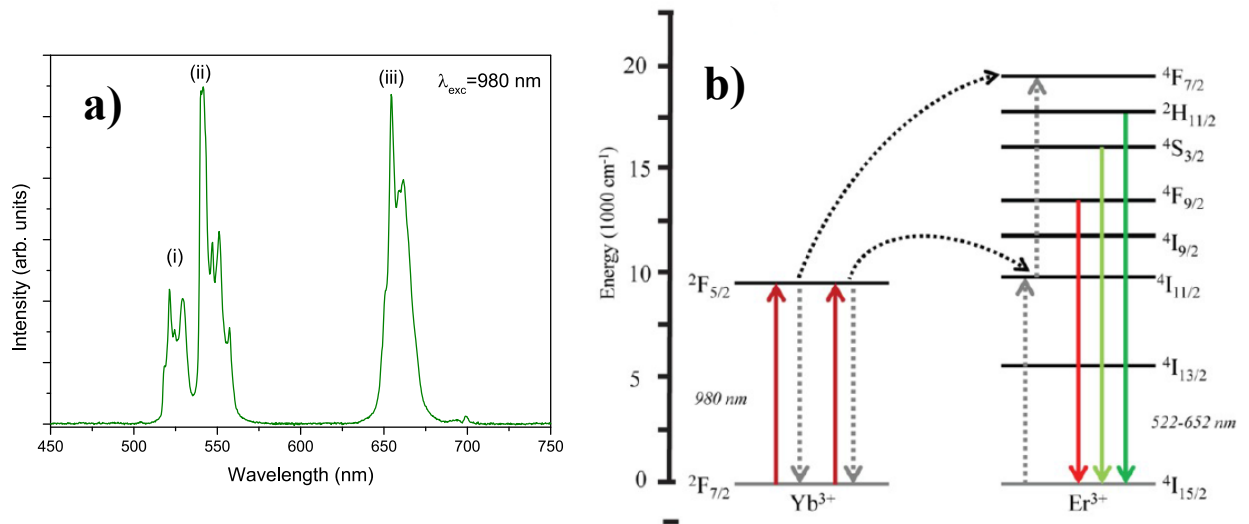


Fig. 14 a) Up-conversion spectrum for the $\text{NaYF}_4: \text{Er}, \text{Yb}$ film ($\lambda_{\text{exc}}=980 \text{ nm}$). Band assignments: (i) ${}^2\text{H}_{11/2} \rightarrow {}^4\text{I}_{15/2}$; (ii) ${}^4\text{S}_{3/2} \rightarrow {}^4\text{I}_{15/2}$; (iii) ${}^4\text{F}_{9/2} \rightarrow {}^4\text{I}_{15/2}$; **b)** diagram of energy level of UC system Yb/Er.

Nonetheless, a more accurate investigation considering more samples with different lanthanide concentrations would be needed to clearly identify the ETU up-conversion process. The spectrum is similar to that found for $\beta\text{-NaYF}_4$ samples of micrometer size doped with Er^{3+} , Yb^{3+} prepared by solvothermal method [32]. The ratio of the red (in the 630-680 nm range) and green (in the 510-580 nm range) integrated emissions for the present sample was found to be 0.845, slightly lower than the value found by Arppe et al. [33] for nanoparticles of Er^{3+} , Yb^{3+} doped hexagonal NaYF_4 . This behavior could be due to the different nature of the samples (thin film and powders) and/or to different lanthanide dopant ratios. The luminescence spectrum is similar to the one obtained for a $\text{NaGdF}_4: \text{Er}, \text{Yb}$ thin film

prepared by electrodeposition [34]. Both curves show a multi-exponential behavior, and therefore an effective lifetime has been calculated from the equation:

$$\tau = \frac{\int tI(t)dt}{\int I(t)dt}$$

where $I(t)$ is the emission intensity at time t and the integral is calculated for $t \gg \tau$. It is worth noting that a similar multiexponential nature of the decay curves has been already observed for Er^{3+} , Yb^{3+} doped NaYF_4 in hexagonal form, in nanoparticles [35]. The appearance of this behavior can be explained by emissions of Er^{3+} ions located in different environments, which experience different distortions of the lanthanide ion coordination sphere. In particular, shorter decay times correspond to ions located in more distorted environments, such as ions located at the surface [36]. On the other hand, longer lifetimes correspond to lanthanide ions positioned in more symmetric environments. Therefore, more than two contributions could be involved in the emission decay curve and we have evaluated the effective lifetimes taking into account all the emission decays in a unique effective lifetime. The obtained effective lifetime values are $287 \pm 2 \mu\text{s}$ and $219 \pm 2 \mu\text{s}$ for the ${}^4\text{F}_{9/2}$ and (${}^2\text{H}_{11/2}$, ${}^4\text{S}_{3/2}$) levels, respectively (fig. 15). The τ values appear to be similar to those reported for $\beta\text{-NaYF}_4\text{:Er,Yb}$ nanoparticles reported by Arppe et al. [33], in particular when the latter nanoparticles are encapsulated in SiO_2 and dispersed in D_2O solvent. This behavior suggests that the non-radiative decay processes for the Er^{3+} ions are not very active, pointing to a good emission.

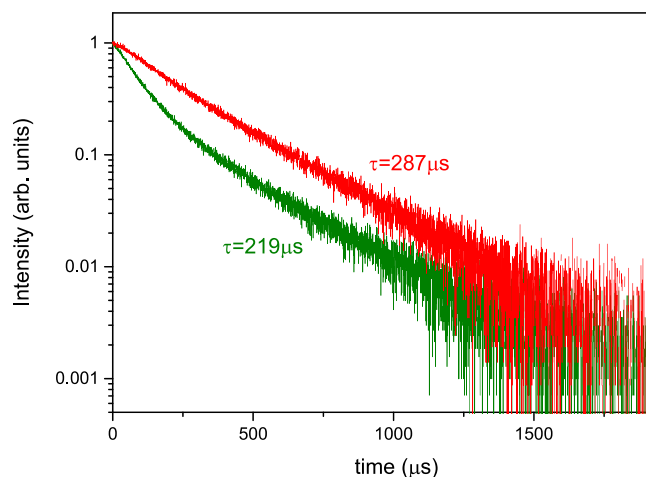


Fig. 15 RT Emission decay curves and effective lifetimes for the Er³⁺ ions of the NaYF₄:Er,Yb film ($\lambda_{\text{exc}}=980$ nm). Red curve: emission at 650 nm from the ⁴F_{9/2} level; green curve: emission at 550 nm from the thermalized (²H_{11/2}, ⁴S_{3/2}) levels. Effective lifetimes are shown.

β -NaYF₄:Yb³⁺, Tm³⁺ systems

Under 980 nm laser excitation, the β -NaYF₄:Yb³⁺, Tm³⁺ films, spin-coated on Si and quartz, present UC emission in the UV, visible and near infrared (NIR) range. Both samples show blue luminescence to the naked eye, as the most intense emission bands are located in the 450-490 nm (fig. 16). As it can be noted from fig. 16, there are no substantial differences between the UC spectra of the samples deposited on Si or on quartz, indicating that the local environment of the lanthanide ions is comparable and that both the substrates are very suitable to grow reproducibly β -NaYF₄ films. This behaviour is also confirmed by the luminescence decay curves for the Tm³⁺ ions in the β -NaYF₄ host, shown in fig. 17 for both substrates. All the decay curves show exponential behaviors and they have been fit with exponential profiles. The obtained lifetimes for the ¹D₂ and ¹G₄ energy levels (from the decay curves acquired at emission wavelengths of 450 nm and 473 nm, respectively) are 390±15 μs and 570±20 μs for the samples deposited on Si (shown in fig. 17a) and 370±20 and 590±10 μs on quartz (shown in fig. 17b), respectively. The substantial similarity of the emission decays and corresponding lifetimes for the two energy levels for the different

samples suggest that in both cases the Tm^{3+} ions experience a similar site environment. It is interesting to note that the lifetimes of the $^1\text{G}_4$ and $^1\text{D}_2$ levels obtained from our investigation result much longer than the values reported by Li et al. for hexagonal Yb^{3+} , Tm^{3+} co-doped NaYF_4 microcrystals ($142.54\mu\text{s}$ and $87.42\mu\text{s}$, for $^1\text{G}_4$ and $^1\text{D}_2$ levels, respectively) [34]. This different behavior could be explained by the different Tm^{3+} concentration used by Li et al. In fact, in the work of Li et al. the Tm^{3+} concentration in NaYF_4 is 3%, while in the present work a 0.5% concentration has been chosen, to avoid concentration quenching that can shorten the luminescence lifetime. On the other hand, Arppe et al. reported about Yb^{3+} , Tm^{3+} co-doped hexagonal NaYF_4 nanocrystals, doped with 0.5% Tm^{3+} , and found lifetimes comparable with the ones reported in this work ($593.0 \pm 10.9 \mu\text{s}$ for the $^1\text{G}_4$ level) [31]. This behaviour highlights the importance of carefully choosing the Tm^{3+} ion concentration to minimize the quenching of the luminescence.

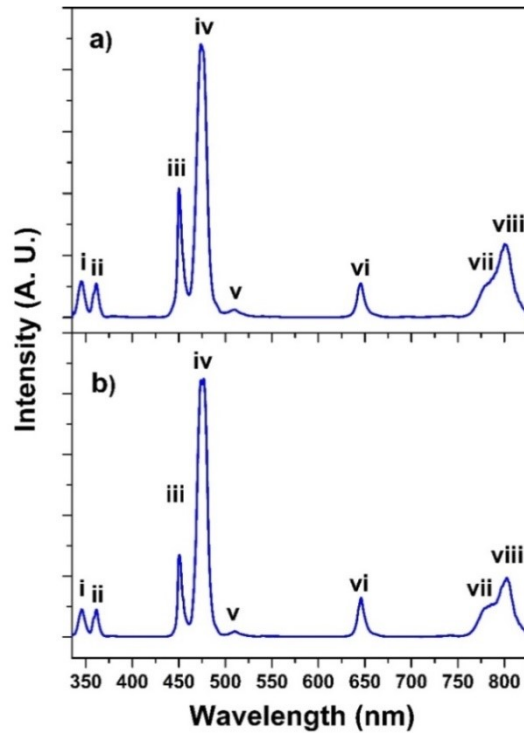


Fig. 16 UC emission spectra of single layer (a) NaYF_4 : $\text{Tm}(0.5\%)$, $\text{Yb}(18\%)$ sample grown on silicon and (b) on quartz. Assignments of the emission bands corresponding to Tm^{3+} ion transitions: (i) $^1\text{I}_6 \rightarrow ^3\text{F}_4$, (ii) $^1\text{D}_2 \rightarrow ^3\text{H}_6$; (iii) $^1\text{D}_2 \rightarrow ^3\text{F}_4$; (iv) $^1\text{G}_4 \rightarrow ^3\text{H}_6$, (v) $^1\text{D}_2 \rightarrow ^3\text{H}_5$, (vi) $^1\text{G}_4 \rightarrow ^3\text{F}_4$, (vii) $^1\text{G}_4 \rightarrow ^3\text{H}_5$, (viii) $^3\text{H}_4 \rightarrow ^3\text{H}_6$.

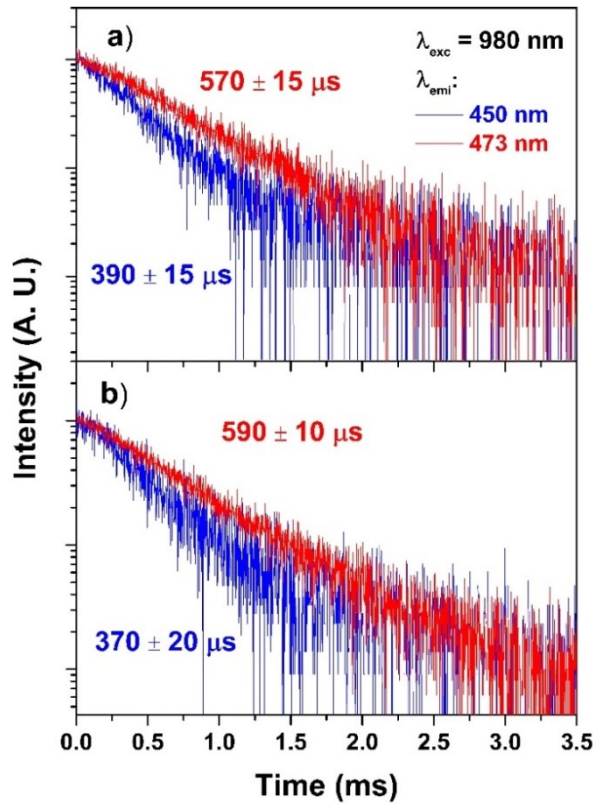


Fig. 17 Luminescence decay times for the (a) NaYF₄: Tm(0.5%), Yb(18%) sample grown on silicon and (b) NaYF₄: Tm(0.5%), Yb(18%) sample grown on quartz. The ¹D₂ (blue curve) and ¹G₄ (red curve) emitting energy levels are

3.3 Ln³⁺ doped β-NaGdF₄ thin films

The sol-gel and spin coating procedure described above and optimized for the β-NaYF₄ thin film systems has also been studied for the fabrication of down converting Eu³⁺ β-NaGdF₄ system using a mixture of Na(hfa)•tetraglyme, Gd(hfa)₃•diglyme and Eu(hfa)₃•diglyme complex as doping source (Hhfa = 1,1,1,5,5,5-hexafluoro-2,4-pentanedione; tetraglyme = 2,5,8,11,14-Pentaoxapentadecane; diglyme = 2-Methoxyethyl ether).

3.3.1 Sol-gel process for the formation of β -NaGdF₄:Eu³⁺ phase films

The optimized route, used to produce phase pure hexagonal NaYF₄ films and co-doped Ln³⁺ β -NaYF₄ thin films, has been conveyed to the fabrication of Eu³⁺ NaGdF₄ because the nature of the Eu doping ion source is similar to the Yb³⁺, Er³⁺, Tm³⁺ ones; and the nature of the Gd source is similar to the Y one. The proper amount of precursors has been set up in accordance to the previous studies at the following molar ratio (ratio **i** for undoped film and ratio **ii** for the doped films):

i) 2 Gd (hfa)₃•diglyme: 2 Na(hfa)•tetraglyme: 87C₂H₅OH : 3H₂O : 0.8CF₃COOH

ii) 1.8 Gd (hfa)₃•diglyme: 2 Na(hfa)•tetraglyme: 0.2 Eu (hfa)₃•diglyme: 87C₂H₅OH : 3H₂O : 0.8CF₃COOH

The sol was aged at 60°C for 20h and spin-coated on Si(100) and quartz substrates. The spin-coating process was carried out at 3000 round per minute (RPM), and speed rate of 1000 RPM/sec with a multistep procedure in which spin-coating deposition (1 minute) is alternated to fast annealing steps at different temperatures (from 200°C to 450°C) in air for 10 min. After four steps, films were annealed at different temperatures (from 200°C to 450°C) in air for 1h.

The preliminary results of XRD, EDX and FE-SEM analysis seem to confirm an excellent reproducibility of the developed process also for the doped hexagonal NaGdF₄ phase.

Energy dispersive X-ray (EDX) analysis (fig. 18) established the film composition in term of dopant ions, which are responsible for the down-converting properties of the material. The EDX spectra of the doped film shows the typical peaks of the Na, Gd, and Eu elements and confirms the correct stoichiometry for the NaGdF₄: Eu³⁺ phase with a Na:Gd:Eu ratio of 1:0.9:0.1 on the whole surface. The absence of a peak at 0.520 keV excludes any O contamination.

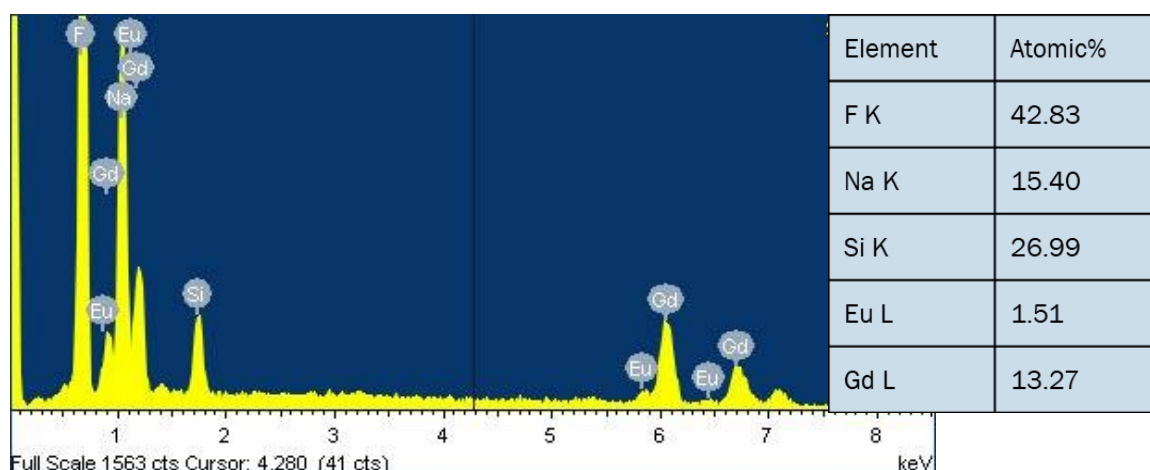


Fig. 18 EDX spectrum of the NaGdF₄:Eu³⁺(10%) film grown on Si (100) at 400°C.

3.3.2 β -NaGdF₄: Eu³⁺ thin films: analysis of phase stability vs. annealing temperature

The work on β -NaGdF₄ phase involved an accurate study of the annealing treatment effect in the evolution of thin films composition and morphology.

These set of NaGdF₄ films has been obtained with the same operating conditions of molar ratio (i) and the same procedure. The annealing temperature of the intermediate steps (10 minutes) and final treatment (1 hour) has been varied from 200°C up to 450°C. The XRD patterns recorded for NaGdF₄ thin films obtained at different annealing temperature: 200°C, 250°C, 300°C, 350°C, 400°C and 450°C are reported in fig. 19. The XRD analysis show for NaGdF₄_200°C the presence of weak peaks associated with the cubic phase α -NaGdF₄ and the peaks associated with the hexagonal phase for the samples at higher temperatures. Furthermore, upon increasing the temperature treatment, the intensity of peaks associated with the β -NaGdF₄ increases gradually. No peaks associated with the cubic NaGdF₄ phase or other phases are present.

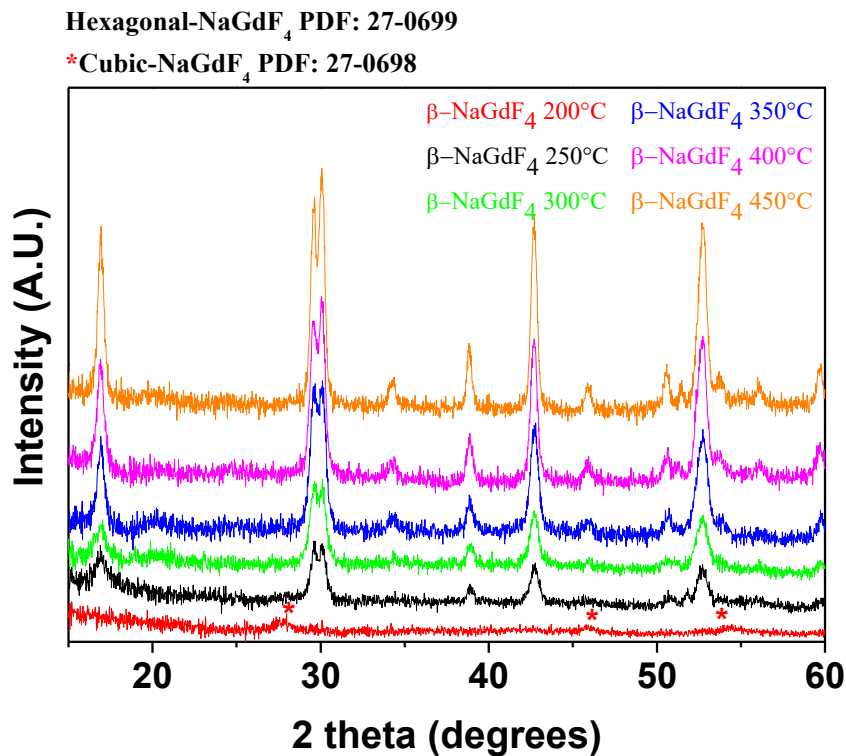


Fig. 19 XRD patterns of NaGdF₄ films grown on Si(100) at different temperatures (from 200°C to 450°C).

FE-SEM plan view images of the NaGdF₄ show different morphologies at different annealing temperatures (T_{ann} from 200°C to 450°C in fig. 20). The FE-SEM images acquired for these samples show differences in morphology: it is observed that the higher the temperature, the most defined is the structure of the deposit, which changes from an amorphous-like structure for treatment at 200°C to a nanostructured and very compact structure for treatments at 400°C and 450 °C with the presence of rounded grains of about 200 nm.

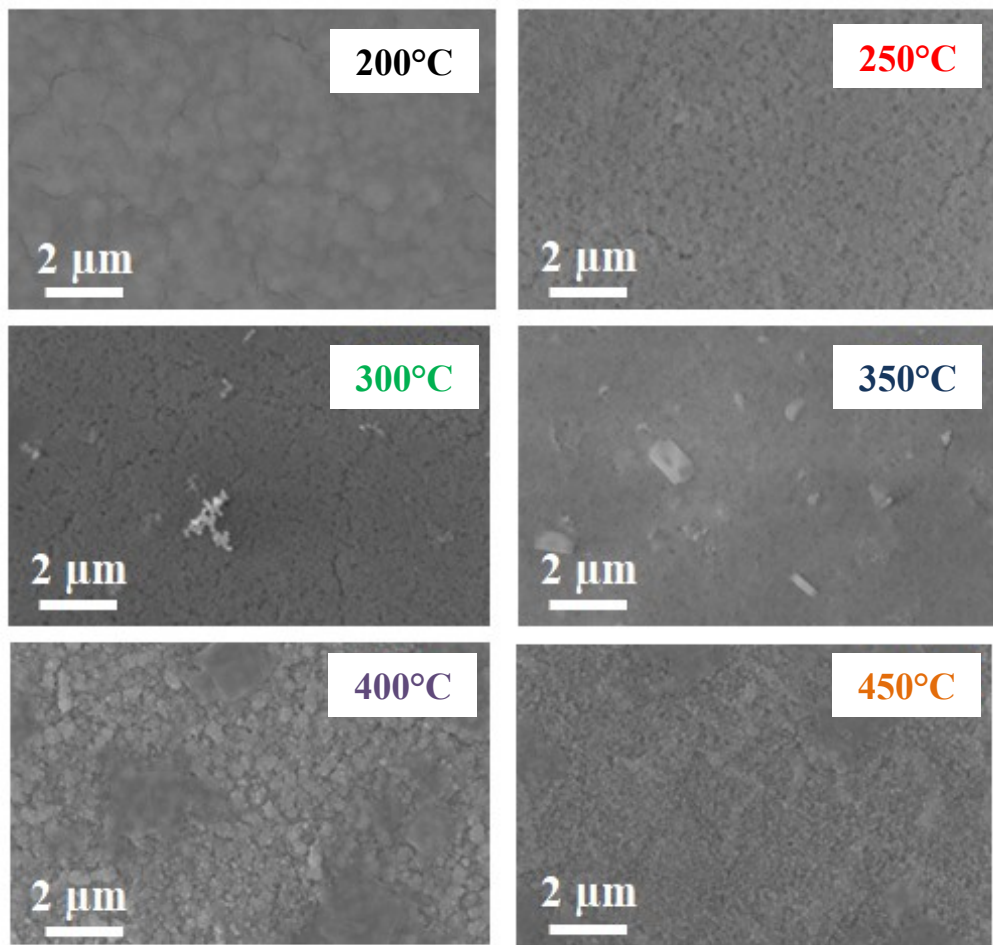


Fig. 20 FE-SEM images of NaGdF₄ films grown on Si (100) at different temperatures (from 200°C to 450°C).

3.4 Ln³⁺ doped YOF thin films

In the following work, sol-gel and spin-coating procedure, described for the doped β -NaYF₄ and β -NaGdF₄ thin films systems, have also been tested for the fabrication of luminescent co-doped Yb³⁺,Tm³⁺ and Yb³⁺,Er³⁺ YOF systems using a mixture of Y(hfa)₃•diglyme, as yttrium precursor and Ln(hfa)₃•diglyme complexes as the doping source (Ln: Yb, Tm, Er; Hhfa = 1,1,1,5,5,5-hexafluoro-2,4-pentanedione; tetraglyme = 2,5,8,11,14-Pentaoxapentadecane; diglyme = 2-Methoxyethyl ether).

3.4.1 Sol- gel process for the formation of YOF thin films

The optimized route, used to produce pure hexagonal phase of co-doped NaGdF₄, has been conveyed to the fabrication of Ln³⁺ YOF. The proper amount of precursors has been set up in accordance to the previous studies and just modified in regard to the concentration of ethanol/water/ trifluoroacetic acid at the follow molar ratio (ratio **i** for undoped films and ratios **ii** and **iii** for the doped films):

i) 1 Y(hfa)₃•diglyme: 29 C₂H₅OH : 1 H₂O : 0.01 CF₃COOH

ii) 0,815 Y(hfa)₃•diglyme: 0,18 Yb(hfa)₃•diglyme: 0,005 Tm(hfa)₃•diglyme: 29 C₂H₅OH : 1 H₂O : 0.01 CF₃COOH

iii) 0,81 Y(hfa)₃•diglyme: 0,18 Yb(hfa)₃•diglyme: 0,01 Er(hfa)₃•diglyme: 29 C₂H₅OH : 1 H₂O : 0.01 CF₃COOH

In analogy with the previous procedures the sol was aged at 60°C for 20h and spin-coated on Si(100) and quartz substrates. The spin-coating process was carried out with a multistep procedure in which spin-coating deposition (1 minute) is alternated to fast annealing steps at temperatures of 400°C in air for 10 min. After four steps, films were annealed at 400°C in air for 1h.

Afterward a systematic study has been carried out to optimize the oxyfluoride YOF pure phase formation with the correct stoichiometry of the doped ions and a uniform and nanostructured morphology. Structural, morphological and compositional characterization of the films have been carried out through XRD, FE-SEM and EDX analysis, respectively, and allow to achieve the final goal.

3.4.2 Structural, morphological and compositional characterization of Ln³⁺ doped YOF thin films

Structural characterization of films obtained on different substrate and for two different doping ions combination has been carried out in this study.

The XRD patterns of the samples YOF:18%Yb,1%Er on Si(100) and quartz obtained through the procedure (iii) show reflections at $2\theta = 28.25^\circ, 32.50^\circ, 40.75^\circ, 47.05^\circ, 55.55^\circ, 58.45^\circ$ associated with a rhombohedral YOF structure, in accordance with the ICDD n° 06-0346 (fig. 21). Similar behavior has been observed on the undoped YOF film and on YOF:18%Yb,0,5%Tm thin films.

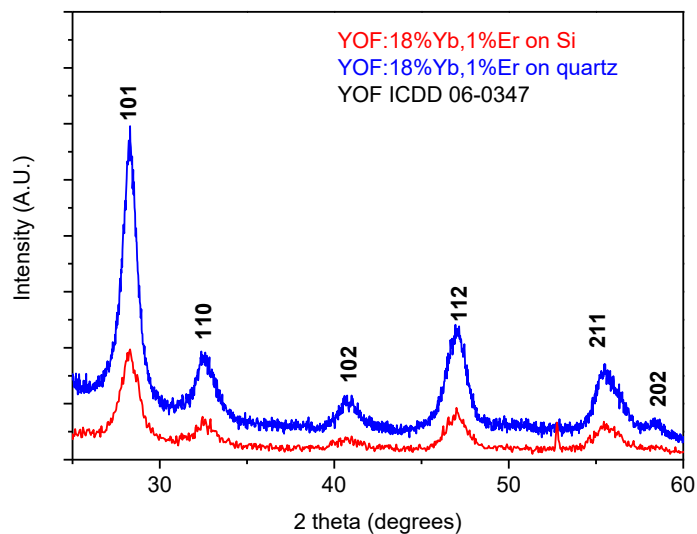


Fig. 21 XRD patterns of YOF:18%Yb,1%Er films grown on Si (100) and quartz.

Microstructure and morphology of doped YOF films have been studied by field emission scanning electron microscopy (FE-SEM).

The FE-SEM image of the films YOF: 18%Yb,0.5%Tm deposited on quartz does not show a homogeneous surface, and shows some cracking as observed in fig. 22a.

These effects are likely due to the difference in the thermal expansion coefficients of the YOF film and that of the quartz substrate. For this reason, the following samples have been cooled with a slow cooling rate ($10\text{ }^{\circ}\text{C min}^{-1}$) from annealing temperature to room temperature, which yields crack-free and compact films on quartz, as observed in fig. 22c for YOF:18%Yb,1%Er on quartz.

The FE-SEM image of the Yb, Tm co-doped YOF film deposited on Si (100) and annealed at $400\text{ }^{\circ}\text{C}$ shows a smooth homogeneous surface throughout the entire surface (fig. 22b). The Yb, Er co-doped YOF film on Si(100) in fig. 22d shows a compact deposit with grains of irregular shapes, similar to the morphology observed for co-doped $\beta\text{-NaYF}_4$ and $\beta\text{-NaGdF}_4$ samples previously reported.

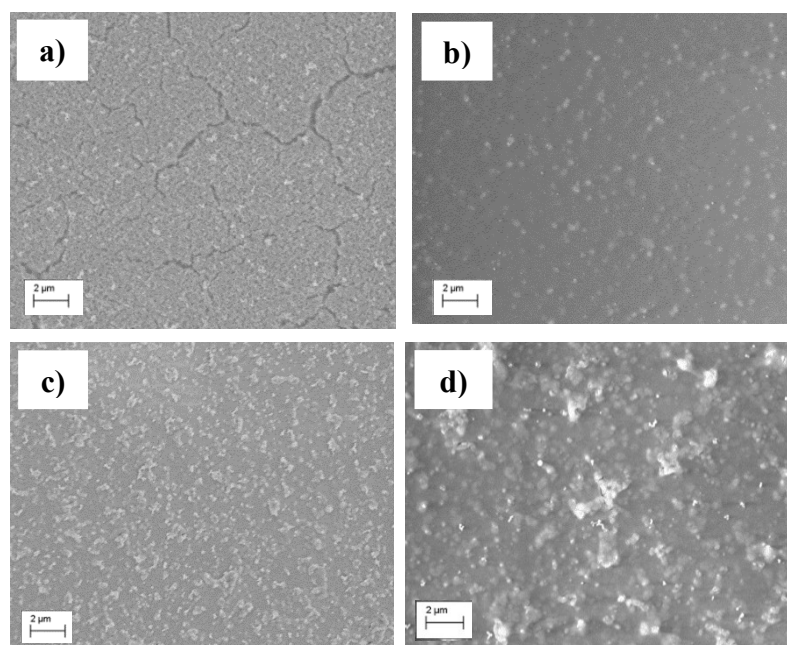
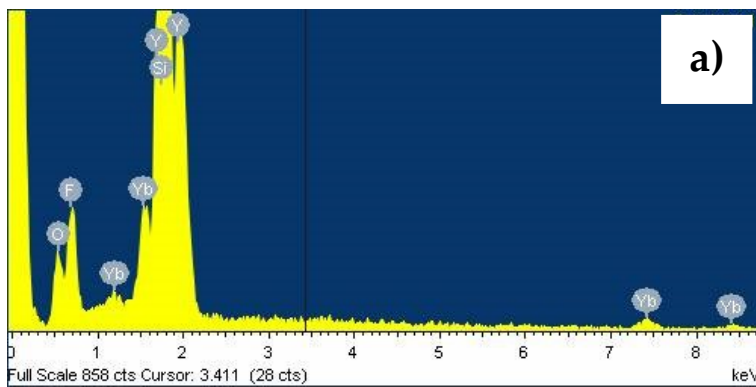


Fig. 22 FE-SEM images of the YOF: Yb(18%), Tm(0,5%) deposited on quartz(**a**) and Si(100) (**b**) and of the YOF: Yb(18%), Er(1%) deposited on quartz(**c**) and Si(100) (**d**).

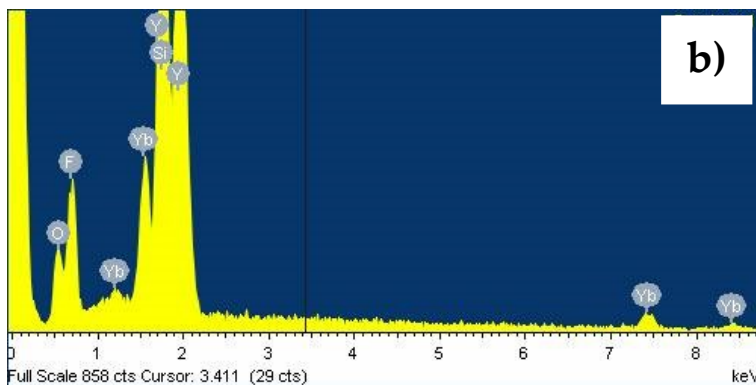
The related quantitative EDX analysis confirms the correct stoichiometry in various zones of the films for the co-doped YOF phase with a Y:Yb ratio of about 1.0:0.18 on the whole surface (fig. 23).

In fact, the Y L peak is observed in the 1.8-2.2 range keV. In addition, the windowless EDX detector allowed to detect the F K α peak at 0.670 keV, and a peak at 0.520 keV associated with the O K α peak, due to the presence of the YOF. It is worthy of noting the absence of C peak, whose K α peak should appear at 0.525 keV.

The thulium and erbium peaks, relative to the nominal concentration of 0.5% and 1%, are scarcely detectable, due to their low concentrations that are at the borderline of the detection limit of the EDX technique.



Element	Atomic%
F K	11
O	13
Y L	6.5
Yb L	1.5
% Yb	18.5%



Element	Atomic%
F K	12.8
O	12.1
Y L	6.4
Yb L	1.34
% Yb	17%

Fig. 23 EDX spectra of the YOF:Yb(18%) Tm(0.5%) film **(a)** and of the YOF:Yb(18%) Tm(0.5%) film **(b)** grown on Si(100).

3.5 Conclusions

In summary, the novel Na(hfa)•tetraglyme compound has been synthesized through a simple one-pot strategy and it represents a suitable single source precursor of Na and F elements for the sol-gel deposition of co-doped sodium rare earth fluoride-containing films. An all-inclusive study of a novel sol-gel process for the fabrication of the β -NaREF₄ (RE: Y, Gd) and YOF phase film, paying attention to the effects of experimental parameters, such as precursors' molar ratios, aging time, annealing temperature and spin-coating deposition procedure is described. Through this approach, the hexagonal NaREF₄ phase films have been selectively and reproducibly prepared by a combined sol-gel/spin-coating approach employing the fluorinated β -diketonate compounds, which act as sources of all the required ions, namely sodium, yttrium or gadolinium and fluorine. The optimized procedure has allowed to produce NaGdF₄:Eu³⁺, NaYF₄:Yb³⁺, Er³⁺ and NaYF₄:Yb³⁺, Tm³⁺ thin films with bright luminescence and their preliminary luminescent properties have been carefully reported in this study. In addition, this synthetic approach has been successfully applied for the fabrication of YOF: Yb³⁺, Er³⁺ and YOF: Yb³⁺, Tm³⁺ thin films.

Compared to other synthetic processes, the sol-gel method is a facile mass production method for synthesizing β -NaREF₄ and YOF in high yield with an inexpensive equipment, low environment loads and high crystallinity.

The X-ray diffraction (XRD) analysis confirms that the new sol-gel preparation route yields reproducibly and selectively the hexagonal structure β -NaREF₄ and YOF without any impurity phases. Field-emission scanning electron microscopy (FE SEM) images indicate that morphology surfaces, grain dimensions and thickness are strongly related to the processing parameters. Energy dispersive X-ray (EDX) analyses established the film composition in term of dopant ions, which are responsible for the energy-converting properties of the materials. Luminescent measurements under laser excitation at 980 nm confirmed promising up-conversion properties for the Ln³⁺ co-doped β -NaREF₄ and YOF films.

Finally, this synthetic strategy paves the way for the synthesis of other fluoride phases in thin film forms for up or also down conversion luminescence properties.

References

- [1] M. R. Catalano, A. L. Pellegrino, P. Rossi, P. Paoli, P. Cortelletti, M. Pedroni, A. Speghini, and G. Malandrino, *New J. Chem.*, 2017, 41(12), 4771-4775.
- [2] G. Malandrino, R. Lo Nigro, I. L. Fragala, C. Benelli, *Eur. J. Inorg. Chem.*, 2004, 3, 500.
- [3] W. Zheng, P. Huang, D. Tu, E. Ma, H. Zhu and X. Chen, *Chem. Soc. Rev.*, 2015, 44, 1379.
- [4] a) J. C. Goldschmidt and S. Fischer, *Adv. Opt. Mater.* 2015, 3, 510; b) P. Ramasamy, P. Manivasakan and J. Kim, *RSC Advances*, 2014, 4, 34873.
- [5] J. Yao, M. Yang and Y. Duan, *Chem. Rev.* 2014, 114, 6130.
- [6] M. Quintanilla, I. X. Cantarelli, M. Pedroni, A. Speghini and F. Vetrone, *J. Mater. Chem. C*, 2015, 3, 3108.
- [7] I. X. Cantarelli, M. Pedroni, F. Piccinelli, P. Marzola, F. Boschi, G. Conti, A. Sbarbati, P. Bernardi, E. Mosconi, L. Perbellini, L. Marongiu, M. Donini, S. Dusi, L. Sorace, C. Innocenti, E. Fantechi, C. Sangregorio, and A. Speghini, *Biomater Sci-Uk*, 2014, 2, 1158; b) C. D. S. Brites, P. P. Lima, N. J. O. Silva, A. Millan, V. S. Amaral, F. Palacio, and L. D. Carlos, *Nanoscale*, 2012, 4, 4799.
- [8] J.-C. G. Bünzli and C. Piguet, *Chem. Soc. Rev.*, 2005, 34, 1048.
- [9] G. Y. Chen, H. C. Liu, G. Somesfalean, H. J. Liang and Z. G. Zhang, *Nanotechnology*, 2009, 20, 385704.
- [10] J. F. Suyver, J. Grimm, M. K. van Veen, D. Biner, K.W. Kramer and H. U. Gudel, *J. Lumin.*, 2006, 117, 1
- [11] K. W. Kramer, D. Biner, G. Frei, H. U. Gudel, M. P. Hehlen and S. R. Luthi, *Chem. Mater.*, 2004, 16, 1244.

- [12] J. C. Boyer, C. J. Carling, B. D. Gates and N. R. Branda, *J. Am. Chem. Soc.*, 2010, 132, 15766.
- [13] N. Erathodiyil and J. Y. Ying, *Acc. Chem. Res.*, 2011, 44, 925.
- [14] F. Wang, Y. Han, C. S. Lim, Y. Lu, J. Wang, J. Xu, H. Chen, C. Zhang, M. Hong and X. Liu, *Nature*, 2010, 463, 1061.
- [15] W. Zou, C. Visser, J. A. Maduro, M. S. Pshenichnikov and J. C. Hummelen, *Nat. Photon.*, 2012, 6, 560.
- [16] Zhengquan Li, Yong Zhang and Shan Jiang, *Adv. Mater.* 2008, 20, 4765–476
- [17] D. T. Klier and M. U. Kumke, *RSC Advances*, 2015, 5, 67149.
- [18] D. L., Jr. Inglefield, T. R. Merritt, B. A. Magill, T. E. Long and G. A. Khodaparast, *J. Mater. Chem. C*, 2015, 3, 5556.
- [19] X. Sang, W. Chen, P. Chen, X. Liu and J. Qiu, *J. Mater. Chem. C*, 2015, 3, 9089.
- [20] C. Wang and X. Cheng, *RSC Advances*, 2015, 5, 94980.
- [21] T. Grzyb, M. Węclawiak, J. Rozowska, S. Lis, *J Alloy Comp* 2013, 576, 345–9.
- [22] H. He, Q. Liu, D. Yang, Q. Pan, J. Qiu, G. Don, *Sci Rep*, 2016, 6, 35348.
- [23] a) K. D. Pollard, J.J. Vittal, G.P. A. Yap, R.J. Puddephatt, *J. Chem. Soc. Dalton Trans.*, 1998, 8, 1265-1268; b) G. Malandrino, R. Lo Nigro, I. L. Fragala, C. Benelli, *Eur. J. Inorg. Chem.*, 2004, 3, 500-509.
- [24] A. Valore, E. Cariati, S. Righetto, D. Roberto, F. Tessore, R. Ugo, I. L. Fragala, M. E. Fragala, G. Malandrino, F. De Angelis, L. Belpassi, I. Ledoux-Rak, K. H. Thi, J. Zyss, *J. Am. Chem. Soc.*, 2010, 132, 4966-4970.
- [25] L. Armelao, G. Bottaro, L. Bovo, C. Maccato, M. Pascolini, C. Sada, E. Soini, E. Tondello, *J. Phys. Chem. C*, 2009, 113, 14429–14434.
- [26] G. Malandrino, L. M. S. Perdicaro, and Ignazio L. Fragalà, *Chem. Vap. Deposition*, 2006, 12, 736–741.
- [27] J. Zhou, Q. Liu, W. Feng, Y. Sun, F. Li, *Chem. Rev.*, 2015, 115, 395-465.
- [28] C. Lorbeer, F. Behrends, J. Cybinska, H. Eckert, A.V. Mudring, *J. Mater. Chem. C*, 2014, 2, 9439-9450.
- [29] R.D. Shannon, *Acta Crystallogr.*, 1976, 32, 751.767.

- [30] a) D. Yang, D. Chen, H. He, Q. Pan, Q. Xiao, J. Qiu, G. Dong, *Scientific Reports*, 2016, 6, 29871; b) J. Wang, H. Song, W. Xu, B. Dong, S. Xu, B. Chen, W. Yu, S. Zhang, *Nanoscale*, 2013, 5, 3412-3420.
- [31] A. Bednarkiewicz, D. Wawrzynczyk, A. Gagor, L. Kepinski, M. Kurnatowska, L. Krajczyk, M. Nyk, M. Samoc, W. Strek, *Nanotechnology*, 2012, 23, 145705.
- [32] (a) J. L. Zhuang, J. Wang, X. F. Yang, I. D. Williams, W. Zhang, Q. Y. Zhang, Z. M. Feng, Z. M. Yang, C. L. Liang, M. M. Wu and Q. Su, *Chem. Mater.* 2009, 21, 160; (b) M. Lin, Y. Zhao, M. Liu, M. Qiu, Y. Dong, Z. Duan, Y. H. Li, B. Pingguan-Murphy, T. J. Lu and F. Xu, *J. Mater. Chem. C* 2014, 2, 3671.
- [33] R. Arppe, I. Hyppänen, N. Perälä, R. Peltomaa, M. Kaiser, C. Würth, S. Christ, U. Resch-Genger, M. Schäferling and T. Soukka, *Nanoscale*, 2015, 7, 11746.
- [34] L. Tian, P. Wang, H. Wang and R. Liu, *RSC Adv.*, 2014, 4, 19896.
- [35] a) W. Yu, W. Xu, H. Song, S. Zhang, *Dalton Trans.*, 2014, 43, 6139. b) J. Zhao, Z. Lu, Y. Yin, C. McRae, J. A. Piper, J. M. Dawes, D. Jin, E. M. Goldys, *Nanoscale*, 2013, 5, 944. c) D. T. Klier, M. U. Kumke, *J. Mater. Chem. C*, 2015, 3, 11228.
- [36] C. Li, Z. Quan, J. Yang, P. Yang, J. Lin, *Inorg. Chem.*, 2007, 46, 6329-6337.

CHAPTER 4

Combined MOCVD/MLD approach for hybrid metalorganic-inorganic systems of NiO thin films with a luminescent europium complex monolayer

Transparent NiO thin films, grown through MOCVD approach, have been successfully functionalized with luminescent europium(III) complex [Eu(hfa)₃phen] through a molecular layer deposition (MLD) process. The surface of as-deposited NiO films were activated using H₂O vapour, and then were functionalized in gas phase by anchoring Eu complexes at different temperatures. The effects of the activation method and the effective temperature for the MLD process, which determines the chemisorption of the Eu complex, were evaluated through X-ray photoelectron and luminescence spectroscopy measurements. These analyses allow the optimization of the procedure and the study of the hybrid system in terms of bonding nature and stoichiometry of the chemisorbed Eu complex on the surface. Luminescence properties of the hybrid system show further information about coordination sites of Eu(III) anchored on the NiO surface and energy conversion phenomena.

4.1 Introduction

The organic-inorganic hybrid systems have attracted great attention because of their potential applications in several fields of material science [1] such as sensors [2], dye sensitized solar cells [3], optoelectronics [4], and heterogeneous catalysis [5].

In these systems, transition metal oxides thin films, such as NiO, are among the most promising inorganic materials, due to their wide spectrum of magnetic, electrical, and optical properties [6-8]. As metalorganic component, Eu(III) complexes have attracted growing interest as efficient downshifter and as a probe to sense the chemical environment.

Among the different synthetic strategies to prepare hybrid systems, such as sol-gel procedure [9], Langmuir-Blodgett techniques [10] and self-assembly through solution route [11] are the most used.

Recently, atomic layer deposition has attracted great interest for the layer-by-layer growth of thin films [12] and the strictly related molecular layer deposition represents an emerging technology as synthetic method to create conformal coating organic molecular layers taking advantage of the self-limiting reactions occurring on the surface during the MLD process [13].

In the present study we applied for the first time a full vapor phase approach based on the sequential steps of (i) MOCVD of the inorganic NiO thin films as reported in ref. [14], and (ii) the molecular layer deposition (MLD) to link on the activated surface in a covalent way the metalorganic monolayer component $\text{Eu}(\beta\text{-diket})_3\text{L}$, where $\beta\text{-diket}$ is 1,1,1,5,5,5-hexafluoro-2,4-pentanedione (hfa) and L is 1,10-phenanthroline. The approach is based on the activation step of the synthesized NiO thin film with a flux of H_2O vapour in order to form $-\text{OH}$ terminal groups on the heated surface. Subsequently, anchoring of the $\text{Eu}(\text{hfa})_3\text{phen}$ complex has been carried out in gas phase through a ligand-exchange reaction between one or two $\beta\text{-diketonate}$ ligands and the terminal $-\text{OH}$ groups. Finally, a sonication step, in a solvent in which $\text{Eu}(\text{hfa})_3\text{phen}$ complex is highly soluble, guarantees that only chemisorbed molecules remain chemically anchored on the NiO surface.

An accurate X-ray photoelectron spectroscopy characterization confirmed the optimal parameter conditions of the activation step and of the covalent anchoring of the luminescent europium(III) adduct onto nanostructured transparent NiO films. Optical properties of the hybrid NiO/Eu(III) system are evaluated by spectroscopy

measurement and show that there is a correlation between the Eu coordination sphere and the luminescence properties of the monolayers.

4.2 Experimental Section

4.2.1 Precursors synthesis

Various $\text{Eu}(\beta\text{-diket})_3\text{L}$ compounds have been studied for the formation of the Eu luminescent monolayer such as $\text{Eu}(\text{tta})_3\text{phen}$ (EuC1), $\text{Eu}(\text{hfa})_3\text{diglyme}$ (EuC2) and $\text{Eu}(\text{hfa})_3\text{phen}$ (EuC3) (fig. 1). They were prepared from europium(III) acetate hydrate suspended in dichloromethane, following the procedure reported in ref [15]. H-TTA (H-TTA = α -thenoyltrifluoroacetone; tmeda = N,N,N',N'-tetramethylethylenediamine) or H-hfa (H-hfa = 1,1,1,5,5,5-Hexafluoro-2,4-pentanedione) together with phen (phen = 1,10-phenanthroline) or diglyme (diglyme = 2-Methoxyethyl ether) were added to such a suspension, and the mixture was maintained under reflux for 1h with constant stirring. Upon ligand addition, the initially transparent mixture assumed a pale orange color. The crystals were carefully washed with several portions of pentane and dried under vacuum.

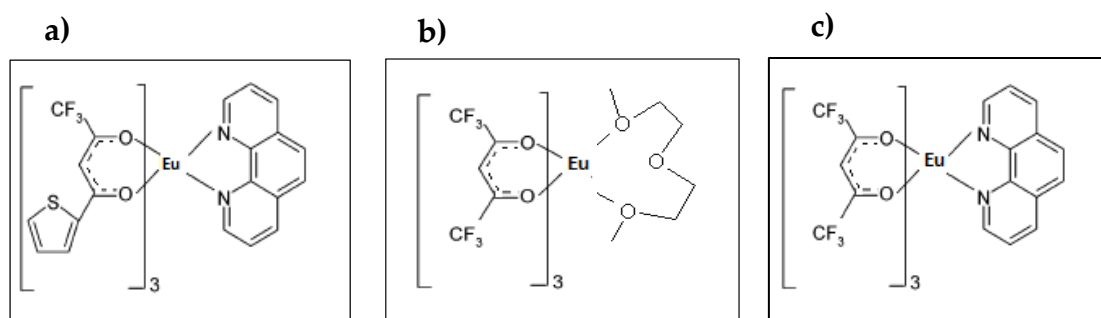


Fig. 1 a) $\text{Eu}(\text{tta})_3\text{phen}$ (EuC1), **b)** $\text{Eu}(\text{hfa})_3\text{diglyme}$ (EuC2) and **c)** $\text{Eu}(\text{hfa})_3\text{phen}$ (EuC3) structures.

4.2.2 MOCVD/MLD synthetic approach

NiO films were deposited on quartz substrates under reduced pressure in a horizontal hot-walled MOCVD reactor using the Ni(TTA)₂TMEDA precursor (fig. 2) [16]. The precursor, contained in a resistively heated alumina boat, was heated at 160°C. Depositions were carried out at a deposition temperature of 400 °C for 60 min. An Ar flow at 150 standard cubic centimeter per minute (scm) and an O₂ flow at 150 scm were used as carrier and reaction gases, respectively. The total pressure in the reactor was about 6 Torr. The mass flows were controlled with a 1160 MKS flowmeter using an MKS 147 electronic control unit.

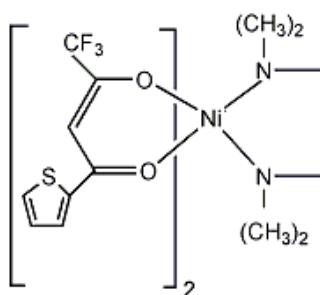


Fig. 2 Ni(tta)₂TMEDA structure.

XPS spectra were recorded with a PHI 5600 multi-technique ESCA-Auger spectrometer with a standard Al-K α X-ray source. Analyses were carried out with a photoelectron angle of 45° (relative to the sample surface) with an acceptance angle of $\pm 7^\circ$. The XPS binding energy (B.E.) scale was calibrated by centering the C 1s peak due to hydrocarbon moieties and adventitious carbon at 285.0 eV [17]. The elemental compositions of the samples were evaluated by estimating the integrated area of each component corrected for the corresponding Wagner sensitivity factor [18].

The novel synthetic procedure for the preparation of the NiO/Eu complex hybrid systems takes place inside a hot wall horizontal reactor and it is schematized in fig. 3. The NiO films have been grown through the MOCVD process at 400°C on

transparent quartz substrates, starting from the $\text{Ni}(\text{tta})_2\text{TMEDA}$ precursor (Fig. 3a) [14]. After the MOCVD synthesis of the inorganic NiO component, the second step regards the surface activation. The NiO film is maintained at 300 °C inside the reactor at the pressure of 300 Torr for 1 hour with a $\text{H}_2\text{O}/\text{O}_2$ flow at 600 ml/min (fig. 3b). The third step procedure is the anchoring of the Eu complex through molecular layer deposition (fig. 3c). The activated NiO substrate is heated testing different temperature $T_1:200^\circ\text{C}$; $T_2:150^\circ\text{C}$ and $T_3:100^\circ\text{C}$ and maintained at the pressure of 4 Torr for 1 hour. Among the various Eu complexes tested (fig. 1) for the formation of the Eu luminescent monolayer, EuC3 complex shows the best properties to be applied in the MLD process. EuC3 complex is vaporized at 160°C and carried on the NiO surface through 150ml/min argon flow, where the ligand-exchange reaction between ligands and surface -OH groups takes place. The chemisorption is guaranteed by an oversaturation of the Eu complex vapors inside the reactor. Finally, the sonication treatment of the samples for 5 min in CH_2Cl_2 ensures that the physisorbed Eu complex is removed together with any impurities and only chemisorbed complexes remain anchored to the NiO surface (fig. 3d).

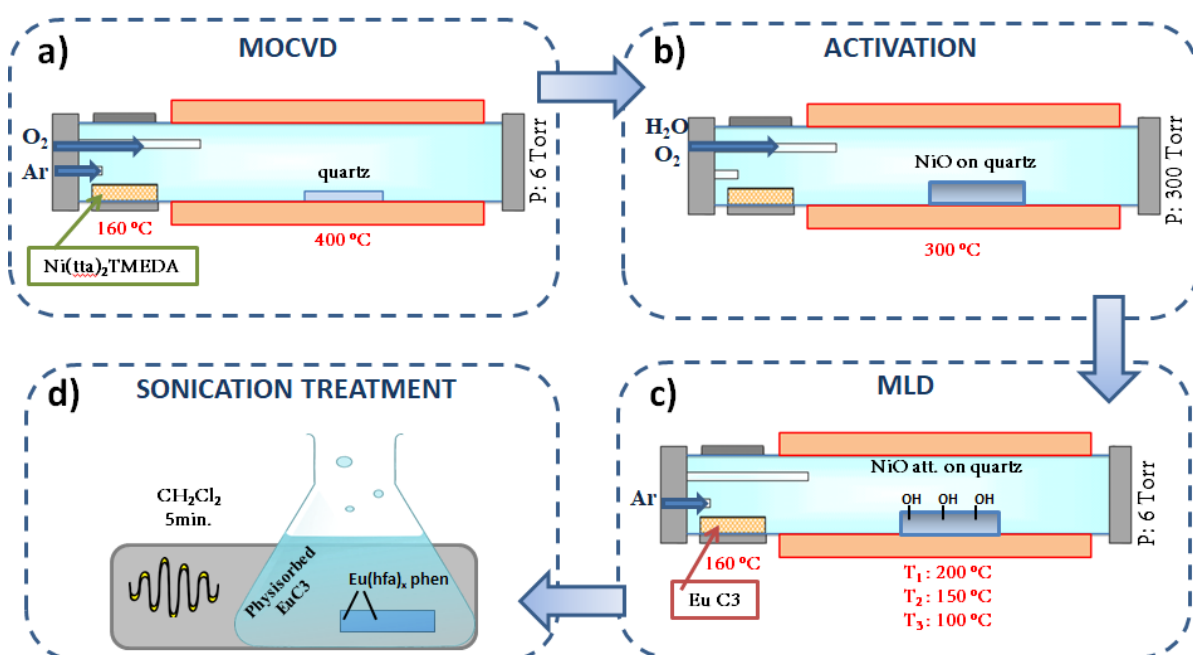


Fig. 3 Scheme of the process: **a)** MOCVD process; **b)** NiO surface activation; **c)** MLD functionalization, **d)** sonication treatment.

4.3 Results and Discussion

The structural and morphological characteristics of NiO_asdep films are shown in fig. 4. FE-SEM images show the formation of a uniform nanostructured NiO film with grains of about 70–80 nm in size (fig. 4a). The XRD pattern (fig. 4b) of all the samples obtained through MOCVD procedure, described above (fig. 3a), shows reflections at $2\theta = 37.25, 43.30, 62.90, 75.40, 79.40^\circ$, associated with NiO cubic structure, in accordance with the ICDD n° 47-1049.

Thermal stability of the EuC1, EuC2 and EuC3 complexes have been tested through thermogravimetric measurement (fig. 5). Thermal behavior of EuC1 indicates a one-step decomposition between 195-205 °C with a residue of about 40% in weight and thus EuC1 complex is not compatible with MLD procedure. Both EuC2 and EuC3 show a one-step vaporization in the 180-190°C and 245-255 °C range, respectively, and a very low residue of about 2% in both cases. Based on TGA data, EuC3 has been chosen because it shows a wide range of thermal stability up to about 240°C. Furthermore, it has also the advantage of the presence of a ligand, the 1,10-phenanthroline, which acts as an antenna useful to enhance the luminescent properties of the final hybrid system.

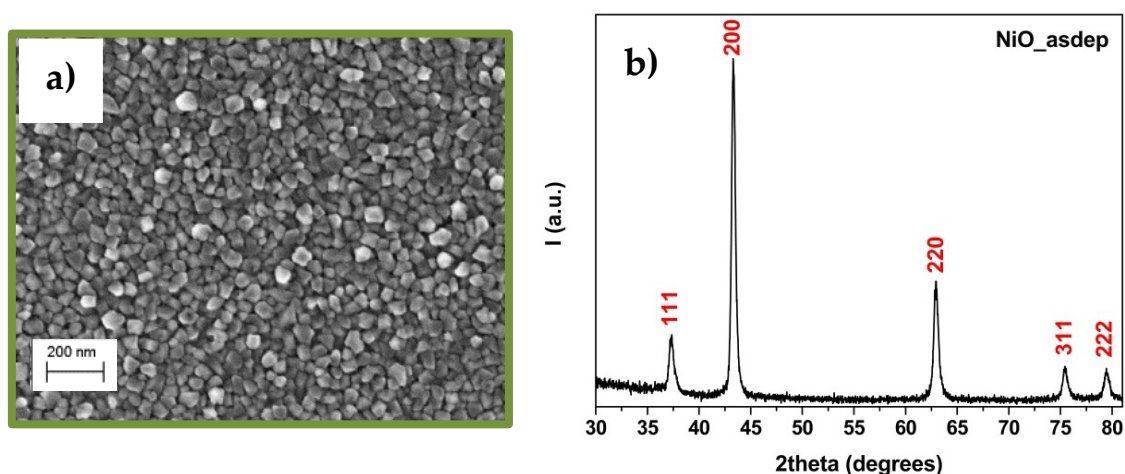


Fig. 4 a) FE-SEM image and b) XRD pattern of NiO_asdep film on quartz substrate.

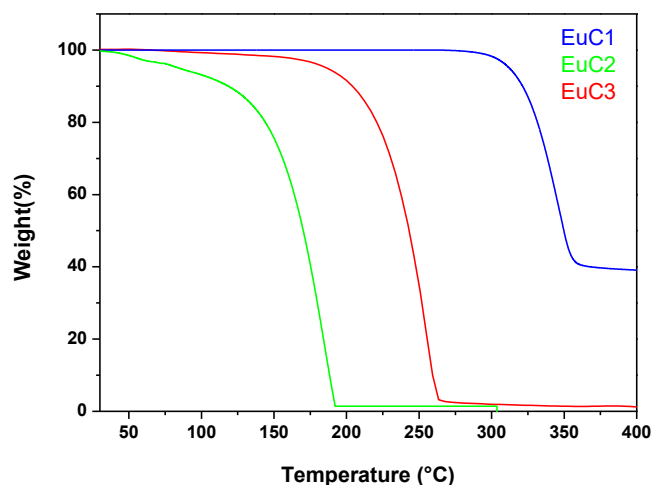


Fig. 5 Thermogravimetric Analysis of EuC1- EuC2 – EuC3

4.3.1 Monolayer characterization

XPS analysis carried out on the surface before and after the MLD process, and for all the different processing parameters have been studied to better understand the monolayer growth on the surface.

Regarding the NiO surface activation, the XPS spectra of oxygen 1s on the NiO surface made before and after the activation through H₂O vapour are reported in fig. 6 and confirm the formation of –OH terminal groups due to the presence of Ni-OH and NiOOH signals. After the activation step and the MLD process the XPS spectra of carbon on the surface confirms the complex anchorage due to the presence of CF₃ signal (fig. 7). The effect of the different temperatures used in the MLD process is also studied to better understand the molecule anchoring on the surface, either due to chemisorption or physisorption processes, and the nature of the final Eu-complex layer. To this aim, the film has been subjected to sonication treatment for 5 min in CH₂Cl₂ in which the complex is highly soluble. At the end of the sonication procedure the XPS characterization confirm that the Eu complex is still present on the

surface (fig. 8b) and the Ni region shows the peak shifted at binding energy of 856 eV (fig. 8a).

Successively, the effect of different temperatures used in the MLD growth process is also studied to assess the most suited temperature for chemisorption of the complex on the surface and to this aim the quantitative analysis on F1s has been carried out at the different MLD temperatures (fig. 9). Two different components are present: one is due to F of the CF_3 group and one is due to F of a fluoride phase. These data indicate that at the highest tested temperatures (T1:200°C and T2: 150°C) the F component of fluoride phase increases, suggesting that some decomposition of the EuC_3 occurs giving rise to an undesirable fluoride phase.

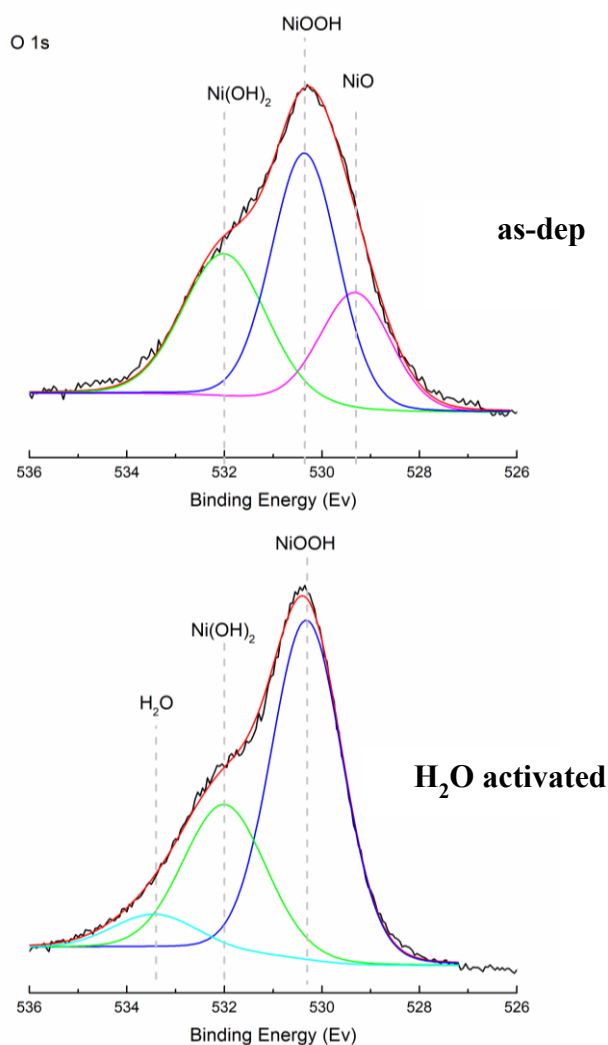


Fig. 6 XPS spectra of oxygen 1s on the NiO surface before and after the surface activation.

At the lowest temperature, the $-\text{CF}_3$ component is predominant, indicating that at this temperature almost no decomposition occurs. The N1s signal for sample at 100°C and after sonication treatment confirms the presence of phen ligand in the layer (fig. 10). All these data univocally point to chemisorption of the EuC_3 on the NiO surface.

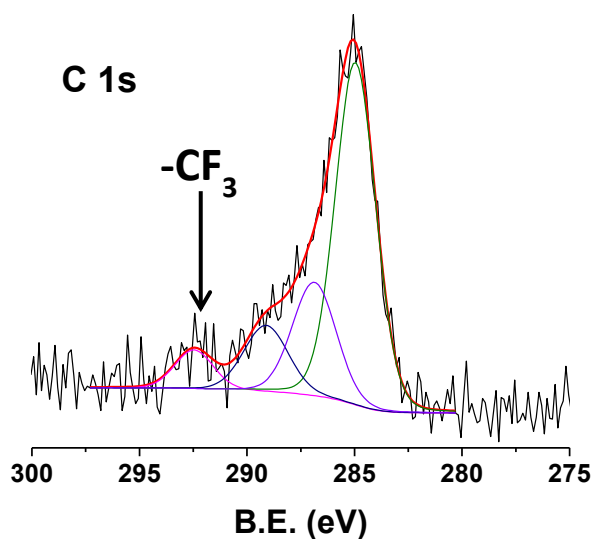


Fig. 7 XPS spectra of C 1s on the surface after activation and complex anchorage.

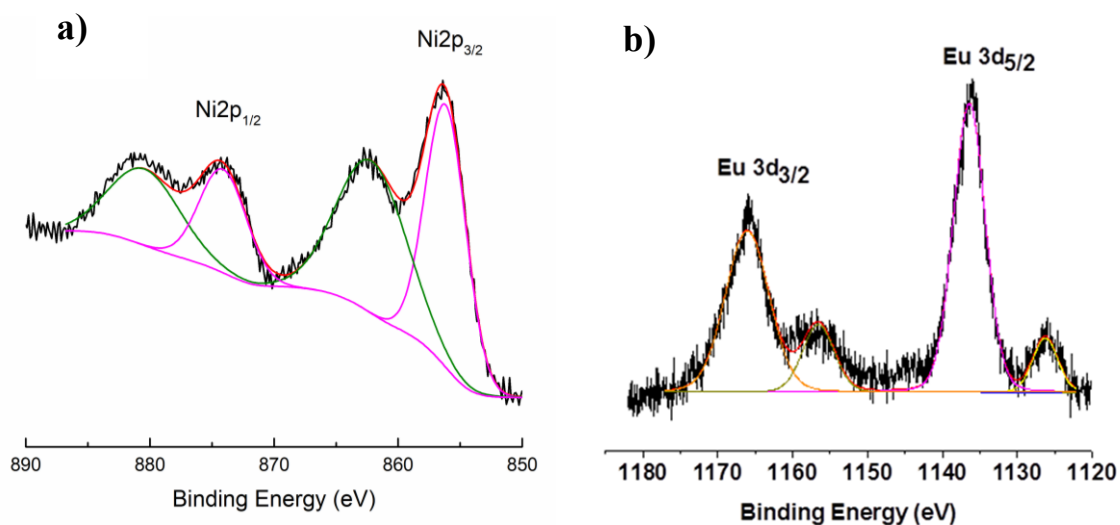


Fig. 8 XPS spectra of Ni 2p (a) and Eu 3d (b) of the hybrid system after the sonication procedure.

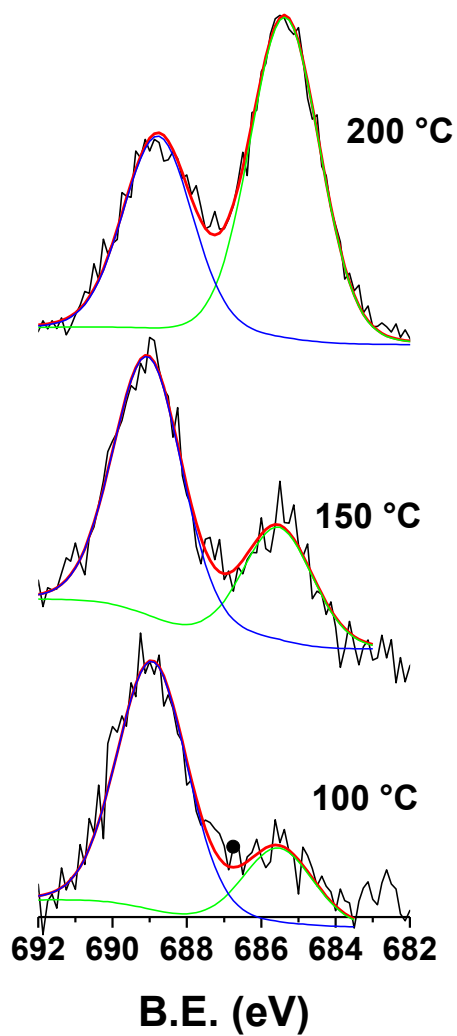


Fig. 9 XPS spectra of F 1s at different temperature: T1: 200°C, T2: 150°C, T3: 100°C.

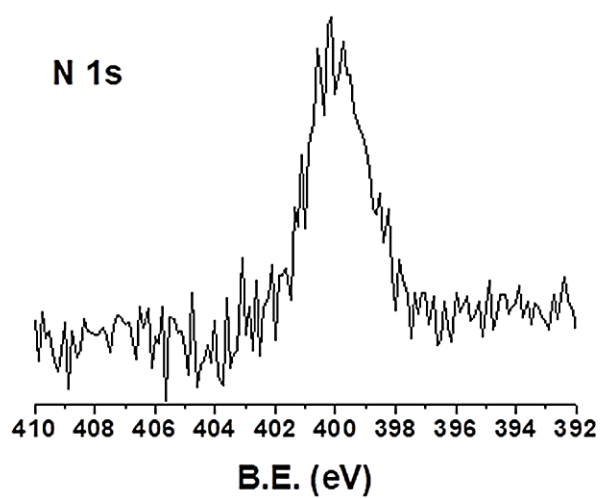


Fig. 10 XPS spectra of N 1s at 100°C after sonication treatment.

Nevertheless, the stoichiometry of the Eu adduct in the monolayer has still to be defined and to this aim XPS quantitative analysis are reported in Table 1. The comparison between the theoretical ratio of Eu:N:F for adducts where Eu (III) has different coordination spheres (see fig. 11) and the ratio found for samples obtained at different MLD temperatures point to the formation of Eu(hfa)phen-adduct and EuF₃ at the highest T3 temperature. The observed experimental XPS Eu:N:F ratio of sample obtained at the lower T1 and T2 temperatures points to the presence of Eu(hfa)₂phen and Eu(hfa)phen adducts.

Sample	Activation	MLD Temp (°C)	Eu:N:F Ratio (XPS)	Stoichiom. in the monolayer
Eu(hfa) ₃ •phen	---	---	1:2:18 (theoretical)	
Eu(hfa) ₂ •phen	---	---	1:2:12 (theoretical)	
Eu(hfa)•phen	---	---	1:2:6 (theoretical)	
NiO_att_Eu_T3	H ₂ O	200	1:0.5:7.5	Eu(hfa)phen + Eu-F
NiO_att_Eu_T2	H ₂ O	150	1:1.8:9.1	Eu(hfa)phen Eu(hfa) ₂ phen
NiO_att_Eu_T1	H ₂ O	100	1:1.7:8.6	Eu(hfa)phen Eu(hfa) ₂ phen

Tab. 1 Stoichiometry of the Eu complex in the monolayer vs. the starting adduct.

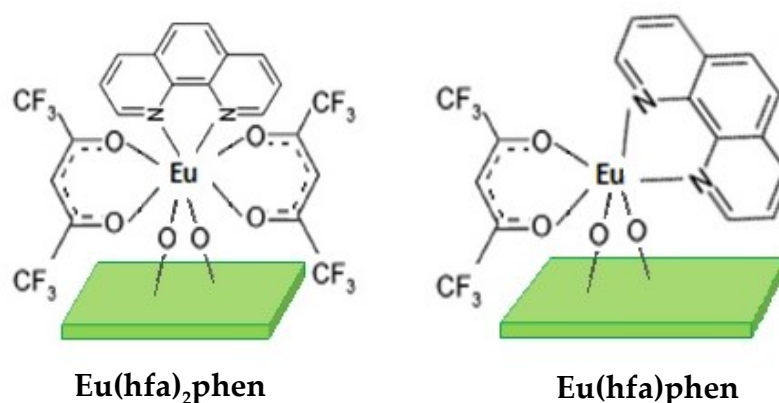


Fig. 11 Eu(hfa)₂phen-adduct and Eu(hfa)phen-adduct schemes.

4.3.2 Luminescent properties of the monolayer

Finally, luminescence characterization of the MLD grown Eu monolayer has been carried out for samples obtained at different MLD deposition temperatures (fig. 12). The emission bands in the visible range are assigned as the scheme of energy level in fig. 13 and are typical of the Eu^{3+} ion emission. In particular, the bands are assigned as following: the two bands in the green region centered at 580 nm and 590 nm are due to ${}^5\text{D}_0 \rightarrow {}^7\text{F}_0$ and ${}^5\text{D}_0 \rightarrow {}^7\text{F}_1$ electronic transitions, respectively. The bands in the red region, centered at around 615 nm, are due to the ${}^5\text{D}_0 \rightarrow {}^7\text{F}_2$ transition.

The ratio of the red (in the 610-630 nm range) and green (in the 590 nm range) integrated emissions for the present samples was estimated with the evaluation of the ratio R, defined as:

$$R = \frac{I({}^5\text{D}_0 \rightarrow {}^7\text{F}_2)}{I({}^5\text{D}_0 \rightarrow {}^7\text{F}_1)}$$

NiO-Eu(hfa)_xphen samples at T2 (fig. 12a) and T3 (fig. 12b) show different intensity value of these two emissions.

This behavior of the different intensity of the emission bands can be explained by emissions of Eu^{3+} ions located in different environments, which experience different distortions of the lanthanide ion coordination sphere.

In particular, lower R value of NiO-Eu(hfa)_xphen_T3 samples corresponds to Eu^{3+} ions located at the surface in more symmetry environments. On the contrary, higher R value of NiO-Eu(hfa)_xphen_T2 samples corresponds to Eu^{3+} ions located at the surface in more distorted environments. These spectra show that the luminescence properties of this hybrid material are useful to give additional information of the ions coordination.

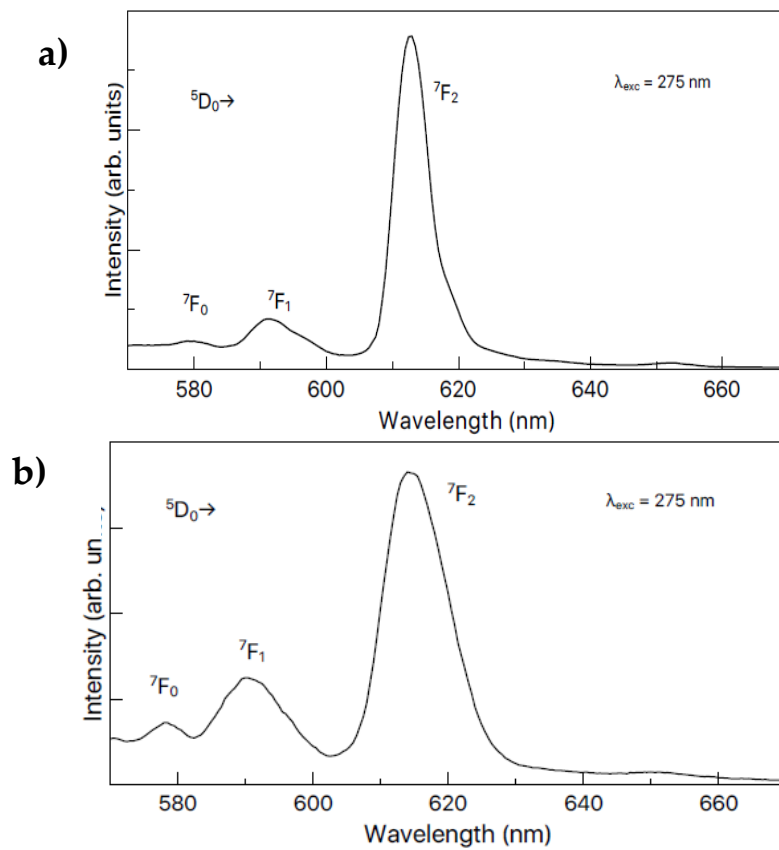


Fig. 12 Luminescent measures of NiO-Eu(hfa)₃phen at T2 (a) and T3 (b).

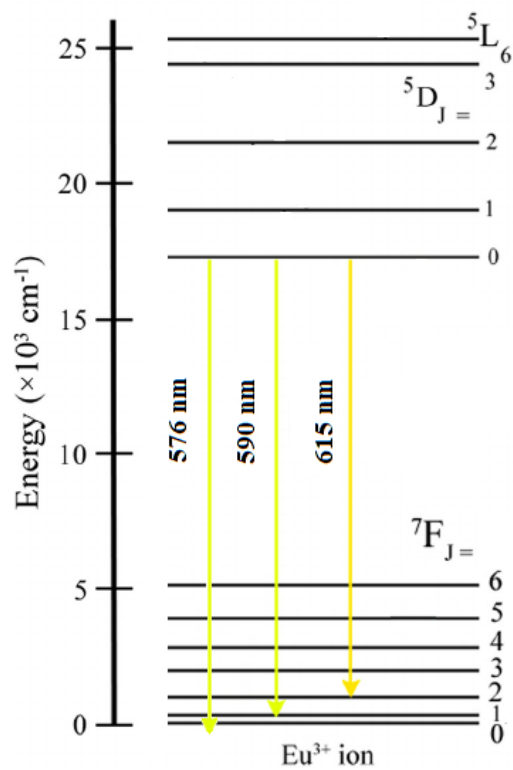


Fig. 13 Energy level scheme for the Eu^{3+} and main emissions mechanisms upon 275 nm excitation.

4.4 Conclusion

In the present study, we applied for the first time a full vapor phase approach for the synthesis of a hybrid metalorganic/inorganic system based on the sequential steps of:

- (i) MOCVD of the inorganic NiO thin films;
- (ii) activation of the surface of transparent NiO as-deposited layers using H₂O vapour;
- (iii) MLD at different temperatures to link on the activated surface in a covalent way an Eu(β -diket)₃L complex, where β -diket is a β -diketone and L is a Lewis base. Various Eu complexes have been tested through thermogravimetric measurement to assess their suitability for the MLD process. EuC₃ has been chosen because it shows a very wide range of thermal stability up to about 240 °C and has the advantage of the ligand antenna 1,10-phenanthroline useful to enhance the luminescent properties of the hybrid system.

The effects of the activation process and the best temperature for the MLD route yielding the chemisorption of Eu complex were evaluated through XPS measurements. An accurate X-ray photoelectron characterization confirmed that the best temperature for the EuC₃ chemisorption on the NiO surface is 100°C. Furthermore, the XPS analysis allows the study of the hybrid system in term of the stoichiometry of the Eu adduct on the surface.

Spectroscopy emission measurements in the visible range for the hybrid NiO/Eu(III) system show a correlation between the Eu(III) coordination sphere and the luminescence and energy conversion phenomena of the monolayers.

References

- [1] M. Mannini, F. Pineider, C. Danieli, F. Totti, L. Sorace, P. Saintavit, M. A. Arrio, E. Otero, L. Joly, J. C. Cezar, A. Cornia, R. Sessoli, *Nature* 2010, 468, 417–421.

- [2] S. Wang, Y. Kang, L. Wang, H. Zhang, Y. Wang, Y. Wang, *Sens. Actuators, B* 2013, 182, 467–481.
- [3] S. A. DiBenedetto, A. Facchetti, M. A. Ratner, T. J. Marks, *Adv. Mater.*, 21, (2009), 1407-1433.
- [4] S. Yaacoub, S. Calas-Etienne, J. Jabbour, K. Amro, R. Tauk, A. Khoury, A. Mehdi, P. Etienne, *RSC Adv.* 2014, 4, 17210– 17217.
- [5] A. P. Wight, M. E. Davis, *Chem. Rev.* 2002, 102, 3589–3614.
- [6] H.-J. Kim, J.-H. Lee, *Sens. Actuators, B* 2014, 192, 607–627.
- [7] J. Huang, G. Natu, Z. Q. Ji, P. Hasin, Y. Y. Lu, *J. Phys. Chem. C* 2011, 115, 25109–25114.
- [8] J. Fu, C. Zhao, J. Zhang, Y. Peng, E. Xie, *ACS Appl. Mater. Interfaces* 2013, 5, 7410–7416.
- [9] J.Y.Wen, G.L. Wilkes, *Chem. Mater.* 1996,8, 1667.
- [10] E. Coronado, C. Mingotaud, *Adv. Mater.* 1999, 11, 869-872.
- [11] E. Smecca, C. Tudisco, A. E. Giuffrida, M. R. Catalano, A. Speghini, G. Malandrino, G. G. Condorelli, *Eur. J. Inorg. Chem.*, 2015, 1261-1268.
- [12] J.Y.Wen, G.L. Wilkes, *Chem. Mater.* 1996,8, 1667
- [13] George, S. M. *Chem. Rev.* 2009, 110, 111–131
- [14] S. Battiato, M. M. Giangregorio, M. R. Catalano, R. Lo Nigro, M. Losurdo, G. Malandrino, *RSC Adv.*, 6, (2016), 30813–30823.
- [15] G. Malandrino, M. Bettinelli, A. Speghini, I. L. Fragalà, *Eur. J. Inorg. Chem.*, 2001, 2001, 1039-1044.
- [16] G. Malandrino, L. M. S. Perdicaro, G. Condorelli, I. L. Fragalà, P. Rossi, P. Dapporto, *Dalton Trans.* 2006, 1101–1106.
- [17] a) I. L. Swift, *Surf. Interface Anal.* 1982, 4, 47–51. b) D. Briggs, G. Beamson, *Anal. Chem.* 1992, 64, 1729–1736.
- [18] C. D. Wagner, L. E. Davis, M. V. Zeller, J. A. Taylor, R. H. Raymond, L. H. Gale, *Surf. Interface Anal.* 1981, 3, 211–225.

CHAPTER 5

Synthesis of inorganic perovskite CsPbBr₃: study of phase stability

The aim of the present study is the development of new active materials to improve the photovoltaic technologies. In the present study, it has been reported the successful fabrication of the all-inorganic halide perovskite CsPbBr₃ using the β -diketonate complexes [Pb(hfa)₂diglyme]₂ and Cs(hfa) (Hhfa = 1,1,1,5,5,5-hexafluoro-2,4-pentanedione; diglyme = 2-Methoxyethyl ether) through a precipitation method in ethanol and water solution with Br₂ as precipitating agent. The entire synthetic process has been operated in ambient environment without humidity control. The control of temperature and aging time for the formation of the pure CsPbBr₃ crystals have been deeply investigated.

Structural, morphological and compositional characterizations of the final product show the formation of microcrystals, with a very small distribution in grain size, of the pure perovskite CsPbBr₃ phase.

5.1 Introduction

The compounds belonging to the family of perovskites ABX₃ show a variety of mechanical, electrical, magnetic and optical properties [1,2], and for these reasons are nowadays key materials for many technologies [3]. In the last years, inorganic halide perovskite and organic-inorganic halide perovskite materials have been studied intensively for photovoltaic applications. Perovskite solar cells (PSCs) are considered

the most promising candidate for the next generation solar cell technology with the advantages of low-cost, low-temperature processing, flexible substrates, and large-area fabrication processes [4-5]. Although many perovskites are already known experimentally, considering the vast number of possible combinations of three chemical elements in the structure ABX_3 , the family of perovskites could be considerably larger and possibly interesting systems are still awaiting our discovery. The hybrid lead-based materials have excellent properties, anyway, the presence of lead causes problems due to its toxicity, and the organic component tends to partially decompose when exposed to air, water, light and heat [6]. The main route to improve the stability of PSCs is to replace the organic component. In this field, there was a growing development of all-inorganic PSCs. The all-inorganic PSCs do not have any labile or expensive components and the entire fabrication process can be operated in ambient atmosphere without humidity control. In particular, the cesium-based all-inorganic materials such as $CsPbBr_3$ show high stability and potentially achieve the creation of highly efficient and stable perovskite solar cells, also considering that no degradation product with lead are reported in literature [7].

In the present study, typical β -diketonate metalorganic compound, used for sol-gel and MOCVD approaches, has been used to obtain the pure phase $CsPbBr_3$ product by precipitation synthesis. Solution methods are simple and well established wet chemistry precipitation processes in which solutions of the different metal ions are mixed under controlled temperature and environment to form insoluble precipitates. The process consists in the preparation, adding a precipitating agent, of an insoluble solid product starting from soluble reagents in the reaction solvent. The choice of the agent depends on the nature of the desired reagents and products. In this case, the precipitating agent Br_2 acts as a real reagent, causing the formation of the insoluble product $CsPbBr_3$. The main steps of this process are: nucleation, crystalline growth and aggregation of the product. The final product is influenced by operative parameters such as temperature, molar ratio, nature of reagents and solvent and the stirring.

5.2 Experimental section

The Cs(hfa) and [Pb(hfa)₂•diglyme]₂ complexes have been prepared according to the procedure previously reported in ref. [8-9] and characterized by thermogravimetric analysis (TGA) and differential scanning calorimetry (DSC) to test purity and thermal stability. The precipitation reaction occurred in water/ethanol solution of Cs(hfa), [Pb(hfa)₂•diglyme]₂, liquid Br₂ was used as precipitating agent and trifluoroacetic acid (CF₃COOH) was used as catalyst. Solutions using different molar ratio of precursors, solvent and catalyst were tested. The mixture was aged at 60°C in a time range from 0h to 20h under stirring. The product was collected by filtration and was washed several times in ethanol. The crystals have been also annealed in a multistep process at 70°C for 20 min in air. The procedure has been repeated every 20 min to reach 40 min, 60 min, 80 min and 100min of annealing treatment. The crystals were deposited on Si (100) by drop-casting and analyzed by XRD in glancing incidence mode (0.5°) using a Bruker D5005 diffractometer and Smartlab Rigaku diffractometer (rotating anode of Cu K α radiation operating at 45 kV and 200 mA). The morphology was analyzed by FE-SEM using a ZEISS SUPRA 55 VP field emission microscope. The atomic composition of the sample was performed by energy dispersive X-Ray (EDX) analysis. The EDX spectra were recorded using an INCA-Oxford windowless detector, having a resolution of 127 eV as the full width half maximum (FWHM) of the Mn K α .

5.3 Results and discussion

Present data show that the phase of the final product is strictly dependent upon reaction time and thermal treatment. In addition, in a preliminary study, the molar ratios of the mixture and the choice of the precursors have been tested to be important parameters. The first procedure routes applied to obtain the CsPbBr₃ phase is the following:

0.5 [Pb(hfa)₂•diglyme]₂ : 1 Cs(hfa) : 1.5Br₂ : 87 C₂H₅OH : 3 H₂O : 0.8 CF₃COOH

The temperature has been set at 60°C under stirring, the metal precursors has been solubilized and subsequently liquid Br₂ added as precipitating agent. The insoluble pale yellow precipitates has been suspended in the stock solution and collected after different aging time intervals t: 0h, 5h, 10h, 15h and 20h, washed in ethanol and deposited on Si(100) substrates for the characterizations.

The XRD patterns recorded for CsPb_xBr_y crystals obtained at different aging time: 0h, 5h, 10h, 15h and 20h are reported in fig. 1. The XRD analysis shows for the sample t:0h the presence of very weak peaks associated with the CsPb₂Br₅ phase, while the main component is the CsPbBr₃ phase. For the sample at longer aging time t: 5h and 10h the intensity of peaks associated with the CsPb₂Br₅ phase increases gradually. Finally, upon increasing the time at 10h, 15h and 20h, the intensity of peaks associated with the CsPb₂Br₅ are predominant. No peaks associated with fluoride or oxide phases are present.

The related FE-SEM images for the samples obtained at t= 0h and t= 5h (fig. 2a,b) show a homogeneous morphology with squared grains of about 1-2 μm. Images obtained for longer aging time up to 20h (fig. 2c, d, e) show grains partially coalescent with irregular shapes and smaller dimensions ranging from 600 nm to about 1μm. This behavior could be explained considering that longer aging time lead to smaller and irregular crystals due to stirring and uncontrolled coalescence.

The energy dispersive X-Ray (EDX) analyses within the grains indicate the difference in composition of the samples, in which the crystals obtained at t= 0h present the Cs:Pb:Br ratio of about 1:0.9:3.1 correlated to the presence of the CsPbBr₃ phase (fig. 3a), while the crystals obtained at t= 5h present a ratio of about 1:2.2:4.6 due to the presence of the CsPb₂Br₅ phase (fig. 3b). These data are in accordance with the XRD data and point out the stability of the CsPbBr₃ perovskite phase at t= 0h.

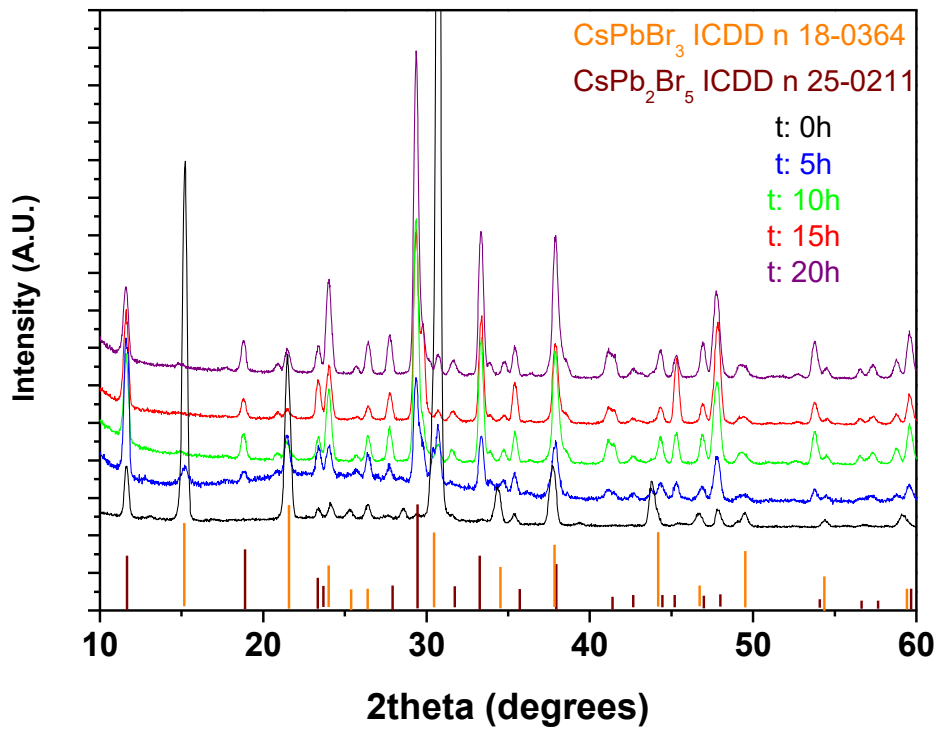


Fig. 1 XRD patterns of CsPbBr₃/CsPb₂Br₅ crystals obtained at aging time t: 0h, 5h, 10h, 15h and 20h.

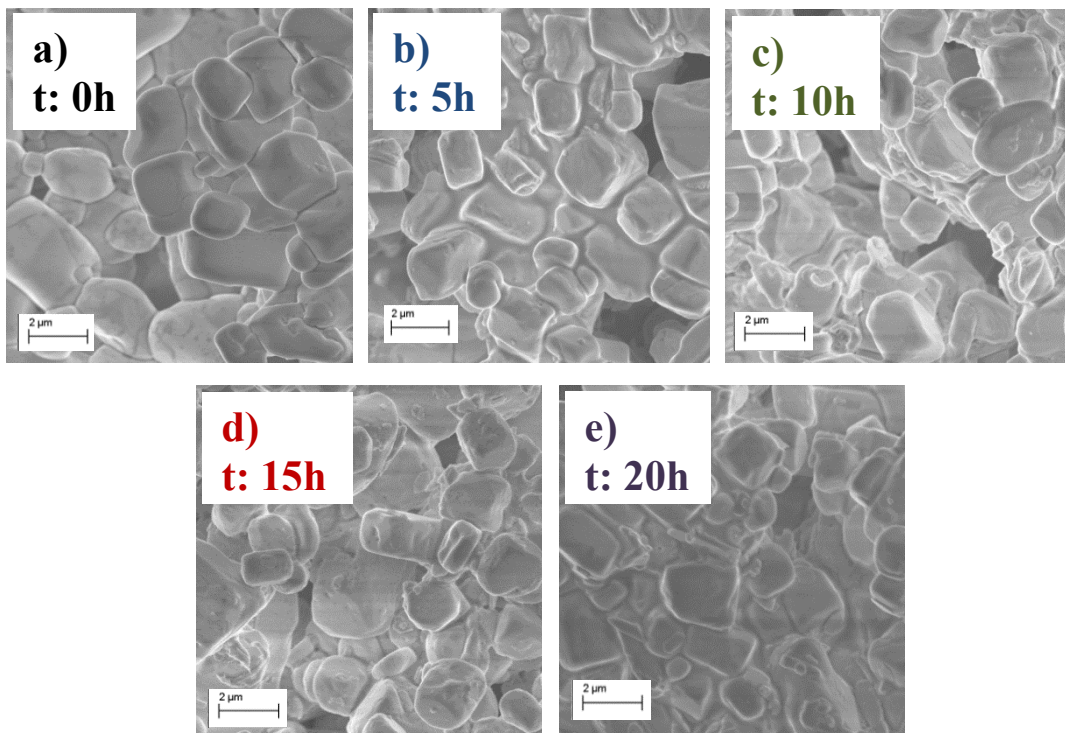


Fig.2 FE-SEM images of CsPbBr₃/CsPb₂Br₅ crystals obtained at aging time t: 0h (a), 5h (b), 10h (c), 15h (d) and 20h (e).

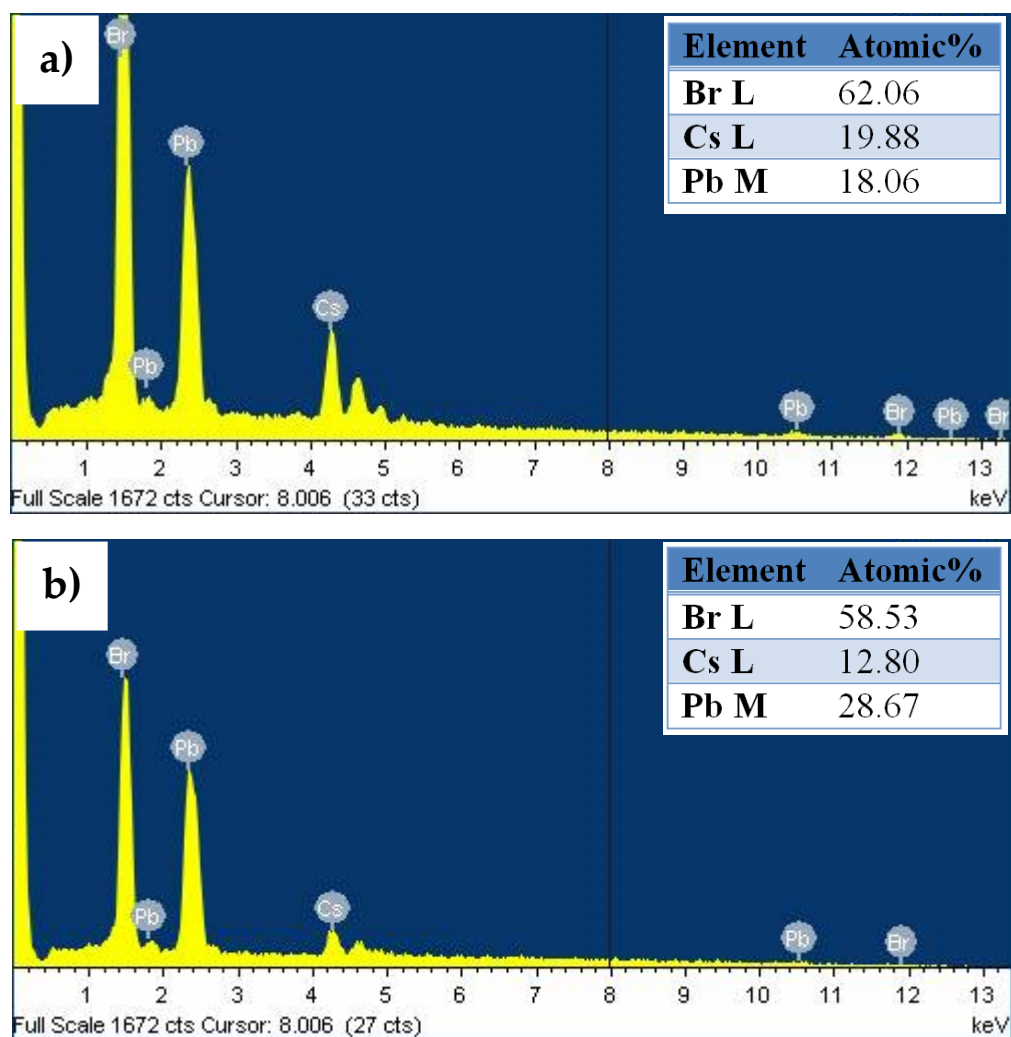


Fig. 3 EDX spectra of CsPbBr₃/CsPb₂Br₅ crystals obtained at aging time t: 0h (a), and 5h (b).

To better understand the stability of CsPbBr₃ versus CsPb₂Br₅ phase a second set of samples has been prepared by following the same molar concentration and experimental procedure previously reported and collecting the crystals at different aging time t:0h, 0.5h, 1h, 3h, 5h. The XRD patterns recorded for these samples are reported in fig. 4. The patterns confirm again that the perovskite CsPbBr₃ phase seems to be present only at the beginning of the precipitation process (t=0h), and then it gradually changes in the CsPb₂Br₅ phase already after 30 minutes of aging. The SEM images recorded for these samples show a morphology quite similar to the crystals reported in fig. 2a and 2b.

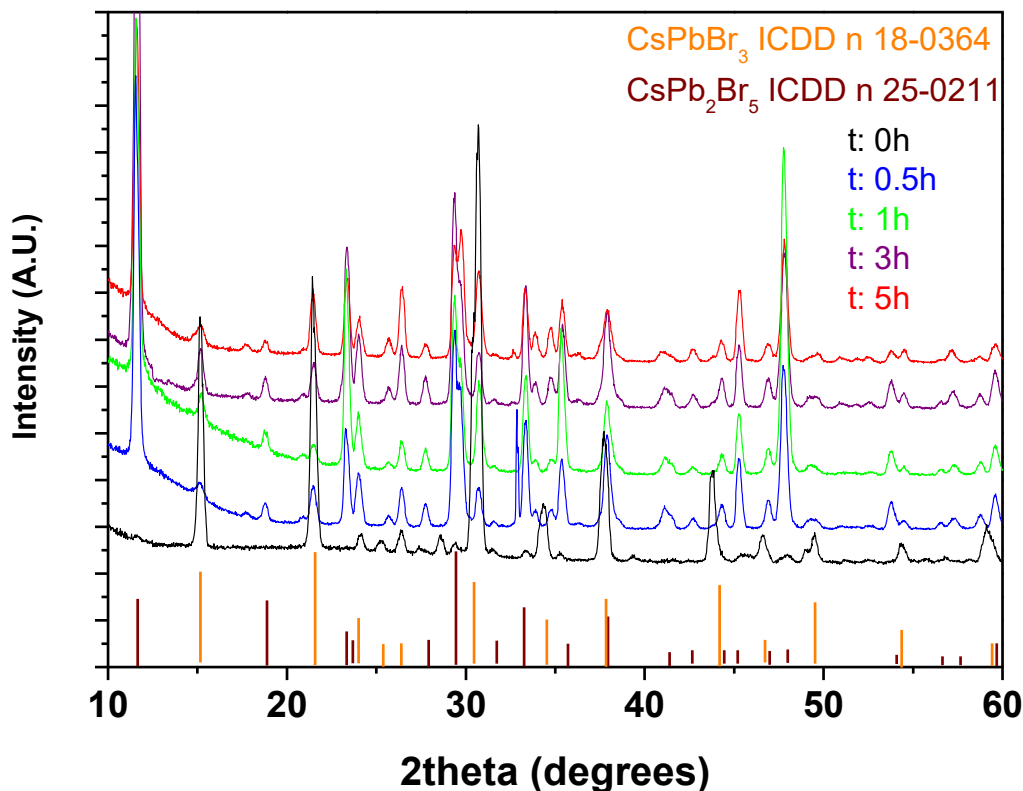


Fig. 4 XRD patterns of CsPbBr₃/CsPb₂Br₅ crystals obtained at aging time t: 0h, 0.5h, 1h, 3h and 5h.

Finally, in order to understand the stability of CsPbBr₃ versus CsPb₂Br₅ phase in relation to temperature, it has been prepared a new set of samples in which the synthesis has been carried out at room temperature and crystals collected at time 0h. Then, the crystals have been annealed at 70°C for 20 minutes in air and this procedure has been repeated every 20 min to reach 40 min, 60 min, 80 min and 100min of annealing treatment. This test allows to study the stability of the material under conditions that simulate those sustained by typical photovoltaic panels under solar irradiation. The different XRD patterns recorded at sequential annealing treatments (fig. 5) show a new correlation between perovskite phase stability and temperature.

The first XRD pattern obtained at time 0h is associated with the CsPbBr₃ phase with traces of CsPb₂Br₅. At longer annealing time processes $t_{\text{annealing}}$: 20min, 40min and 60min the peaks associated with the CsPb₂Br₅ phase increase gradually, while at annealing times $t_{\text{annealing}}$ of 80min, 100min a prevalence of the CsPbBr₃ phase occurs. By comparing these data with those obtained from the previous syntheses, it can be hypothesized that while the permanence of the product within the reaction mixture seems to stabilize the CsPb₂Br₅ phase compared to the CsPbBr₃, the annealing treatment processes do not promote this exchange, and tend to stabilize the CsPbBr₃ phase.

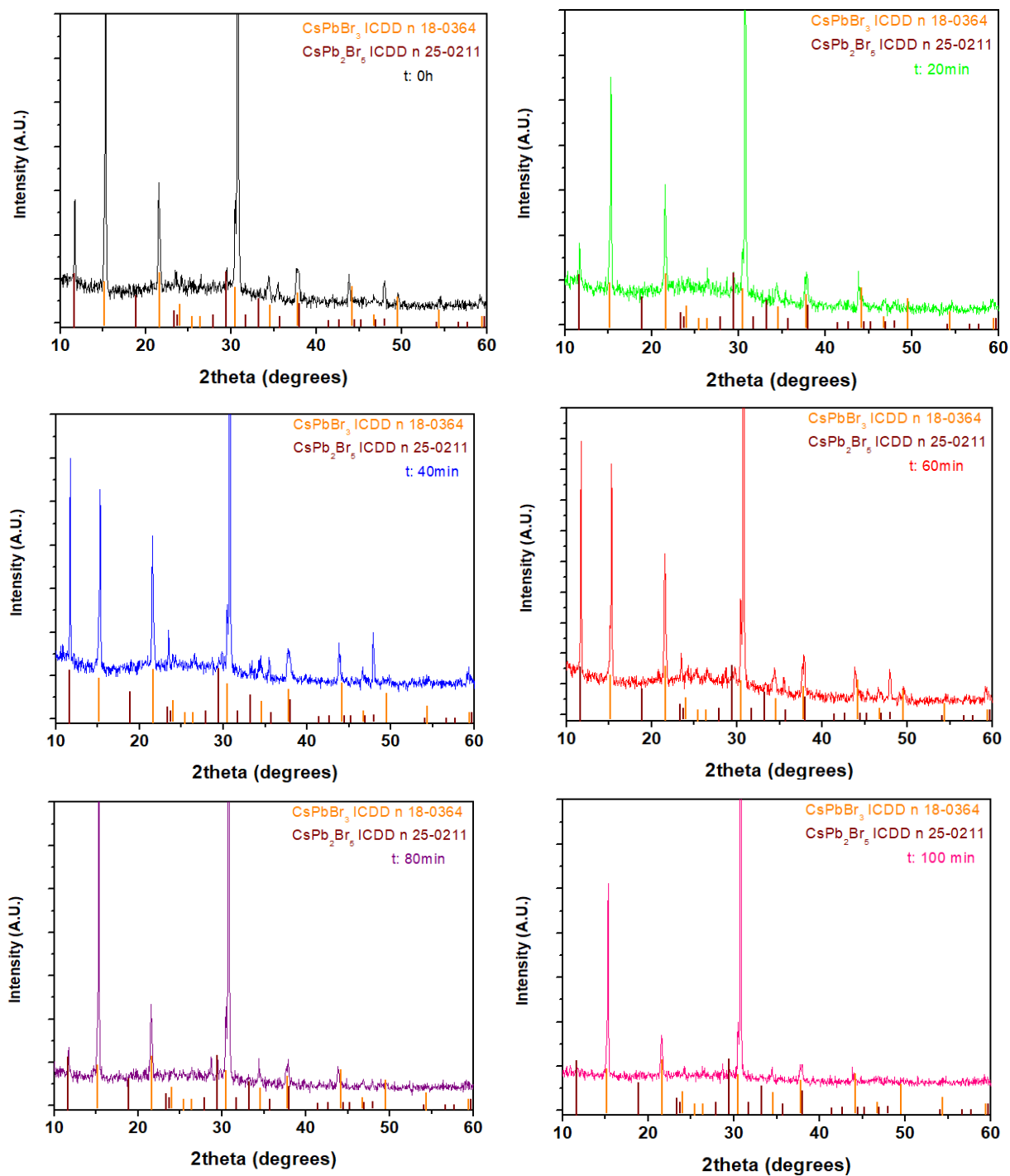


Fig. 5 XRD patterns of CsPbBr₃/CsPb₂Br₅ crystals obtained at aging time t: 0h, annealing temperature 70°C for: 20 min, 40 min, 60min, 80min, 100min.

5.4 Conclusion

In summary, the aim of the present work is the development of a novel and simple precipitation method for the fabrication of perovskite CsPbBr_3 phase using the metal β -diketonate complexes $[\text{Pb}(\text{hfa})_2\text{diglyme}]_2$ and $\text{Cs}(\text{hfa})$ and Br_2 as precipitating agent in ethanol and water solution. The precipitation process takes place very rapidly after the addition of bromine in the reagents solution, and does not require high temperatures and humidity control. The product has been washed with ethanol before being collected and characterized. The work on CsPbBr_3 phase involved an accurate study of the effect of process parameters such as aging time and annealing treatment on the evolution of material composition and morphology.

The CsPbBr_3 - CsPb_2Br_5 crystals have been deeply investigated through XRD, FE-SEM and EDX measurements. Upon increasing the aging time, the intensity of peaks associated with the CsPb_2Br_5 increases gradually. The set of CsPbBr_3 - CsPb_2Br_5 crystals obtained with the same operating conditions at room temperature and with annealing treatment at 70°C for different time shows the stability of the perovskite phase under these operative parameters. Quantitative EDX analysis confirms the correct stoichiometry for the two different phases.

Finally, the FE-SEM images indicate that morphology, grain dimensions and shapes are strongly related to the processing parameters: with squared grains of about $1\text{-}2\mu\text{m}$ at time 0h and grains with irregular shapes and smaller dimensions ($600\text{ nm-}1\mu\text{m}$) at longer aging time.

References

- [1] B. Jaffe, *Piezoelectric ceramics*, Elsevier, 2012, vol. 3.
- [2] A. Kojima, K. Teshima, Y. Shirai and T. Miyasaka, *J. Am. Chem. Soc.*, 2009, 131, 6050–6051.
- [3] a) J. Wang, J. B. Neaton, H. Zheng, V. Nagarajan, S. B. Ogale, B. Liu, D. Viehland, V. Vaithyanathan, D. G. Schlom, U. V. Waghmare, N. A. Spaldin, K. M. Rabe, M. Wuttig and R. Ramesh, *Science*, 2003, 299, 1719–1722; b) S. Aharon, A. Dymshits, A. Rotem and L. Etgar, *J. Mater. Chem. A*, 2015, 3, 9171–9178.
- [4] a) J. Bisquert, Y.B. Qi, T. Ma, Y. Yan, *ACS Energy Lett.*, 2017, 2, 520–523. b) N. G. Park, M. Gratzel, T. Miyasaka, K. Zhu, K. Emery, *Nat. Energy* 2016, 1, 16152; b) P. Docampo, T. Bein, *Acc. Chem. Res.* 2016, 49, 339–346.
- [5] a) M. Remeika, S.R. Raga, S. Zhang, Y.B. Qi, *J. Mater. Chem., A* 2017, 5, 5709–5718; b) M.R. Leyden, Y. Jiang, Y.B. Qi, *J. Mater. Chem. A*, 2016, 4, 13125–13132.
- [6] Y.-Y. Zhang, S. Chen, P. Xu, H. Xiang, X.-G. Gong, A. Walsh and S.-H. Wei, *AIP Adv.*, 2015, 01301.
- [7] A. F. Akbulatov, S. Y. Luchkin, L. A. Frolova, N. N. Dremova, K.L. Gerasimov, I. S. Zhidkov, D. V. Anokhin, E. Z. Kurmaev, K.J. Stevenson, and P. Troshin, *J. Phys. Chem. Lett.* 2017, 8, 1211–1218.
- [8] G. Malandrino, R. Lo Nigro, P. Rossi, P. Dapporto, I. L. Fragalà, *Inorganica Chimica Acta*, 2004, 356, 3927–3933.
- [9] E. S. Vikulova, K. V. Zherikova, N. V. Kuratieva, N. B. Morozova, I. K. Igumenov, *Journal of Coordination Chemistry*, 2013, 66, 2235–2249.

Conclusion

The aim of the present PhD thesis has been the synthesis of novel materials for photovoltaic applications. As reported in the overview of chapter 1, the attention has been devoted to some hot topics in the field of photovoltaic technologies. In particular, the study has been focused on three different kind of materials: i) lanthanide doped fluorides films for energy conversion application in Si solar cell; ii) hybrid metalorganic/inorganic systems Eu-complex/NiO for the DSSC technology; iii) the all-inorganic halide perovskite CsPbBr₃ as a semiconductor active material in the PSCs technology.

Different synthetic strategies have been tested and optimized, namely MOCVD, sol-gel and MLD, depending on the kind of materials to synthesize.

i) Lanthanide doped fluoride phases have been synthesized through MOCVD and sol-gel approaches.

A simple MOCVD process has been applied to the fabrication of single component fluoride thin films Yb³⁺/Er³⁺ and Yb³⁺/Tm³⁺ doped CaF₂, and multicomponent fluoride thin films NaYF₄ and KYF₄.

The Yb³⁺/Er³⁺ and Yb³⁺/Tm³⁺ doped CaF₂ films have been synthesized using the M(hfa)_n•diglyme complexes, which act as single-source precursors. A comprehensive characterization of the films shows the formation of pure and polycrystalline thin films with a very uniform surface, depending on the choice of the substrate and a suitable doping ions combination. The Ln³⁺ doped CaF₂ films show promising up-conversion properties in the visible and near infrared regions upon laser excitation for the different doping mixtures.

The β-NaYF₄ thin films have been synthesized using a Na-Y precursor Na[Y(hfa)₄]⁻[Na•tetraglyme]⁺. An accurate selection of the operative parameters has

allowed the optimization of the process to stabilize selectively and reproducibly either the cubic or the hexagonal phase. The study has proven that both deposition temperature and substrate position in the reactor play a crucial role in stabilizing the NaYF₄ phase.

MOCVD method has been successfully applied for the fabrication of KYF₄ nanostructured thin films as well. For this purpose, the novel fluorinated “third-generation” bimetallic precursor KY(hfa)₄•tetraglyme has been for the first time synthesized through a one-step reaction with a high yield and the experimental results confirm a good thermal behavior for the MOCVD application. An accurate optimization of the deposition parameters, such as the deposition temperature and the vaporization temperature of the precursors, has been conducted and allows reproducibly and selectively the synthesis of pure KYF₄ thin films.

The field-emission scanning electron microscopy images of the single and multicomponent fluoride thin films indicate that morphology surfaces, grain dimensions and thickness are strongly related to the processing parameters.

A further comment deserves the MOCVD approach presently applied, that is very challenging also in view of its easy scalability, which makes it very attractive for industrial scaling up.

A novel sol-gel process has been developed for the fabrication of the lanthanide doped β -NaREF₄ (RE: Y, Gd) and YOF thin films, paying attention to the effects of experimental parameters, such as precursors' molar ratios, aging time, annealing temperature and spin-coating deposition procedure is described. Through this approach, the hexagonal NaREF₄ phase films have been selectively and reproducibly prepared using combined sol-gel/spin-coating approach employing the fluorinated β -diketonate compounds, previously applied in the MOCVD approach. In addition, a novel Na(hfa)•tetraglyme compound has been synthesized through a one-pot strategy and together with Y(hfa)₃•diglyme act as sources of all the required ions, namely sodium, yttrium and fluorine. Structural, morphological, and compositional characterization of the films shows the formation of pure phases and polycrystalline

thin films with a very uniform surface and suitable doping. Luminescent measurements under laser excitation at 980 nm confirmed promising up-conversion properties for the Ln^{3+} co-doped $\beta\text{-NaYF}_4$ films.

It is worth to mention that, the sol-gel method combined with a spraying depositing approach may represent a facile mass production method for synthesizing $\beta\text{-NaYF}_4$ in high yield with an inexpensive equipment, low environment loads and high crystallinity. Finally, this synthetic strategy paves the way for the synthesis of other fluoride phases in thin film forms for up- or also downconversion luminescence.

ii) Concerning the hybrid metalorganic/inorganic systems for the first time a full vapor phase approach has been applied involving MOCVD for the deposition of inorganic NiO thin films and MLD for the chemisorption of the $\text{Eu}(\text{hfa})_3\cdot\text{phen}$ complex. The effects of the NiO surface activation process, needed to generate $-\text{OH}$ groups, and of the temperatures used for the MLD step of the Eu complex chemisorption were evaluated through X-ray photoelectron spectroscopy measurements. XPS characterization established for MLD procedure the optimal parameter conditions of the activation step and of the covalent anchoring process. Furthermore, XPS analysis allowed to investigate the nature of the hybrid system in term of stoichiometry of the Eu adduct on the surface. The spectroscopy emission measurements, also due to the ligand antenna effect of 1,10-phenanthroline, show the relationship between the Eu(III)coordination sphere and the luminescence phenomena of the monolayer.

This study represents the first report of MLD of a metalorganic complex on inorganic substrate.

iii) A novel and simple precipitation method for the fabrication of perovskite CsPbBr_3 phase using $[\text{Pb}(\text{hfa})_2\text{diglyme}]_2$ and $\text{Cs}(\text{hfa})$ complexes and Br_2 as precipitating agent has been carried out. The precipitation process takes place very rapidly, does not require high temperatures and humidity control. The effect of aging time, annealing

treatment and stoichiometry of the reagents on the evolution of material composition has been deeply investigated through XRD, FE-SEM and EDX measurements. XRD measurements show the stabilization of two phases, CsPbBr_3 and CsPb_2Br_5 , in relation with the reaction temperature and the annealing treatment. This investigation has allowed to test the material under conditions similar to those experienced by typical photovoltaic panels when exposed to solar irradiation. Different kind of crystals have been obtained and FE-SEM images indicate that morphology, grain dimensions and shapes are strongly related to the processing parameters.

Curriculum, publications and conferences

Curriculum vitae

Personal information

Last name Pellegrino
First name Anna Lucia
Nationality Italian
Date of birth 12/08/1989

Education

- 2008:** Scientific High School (95/100) Liceo Scientifico E. Fermi Paternò (CT), Italy.
- 2012:** Bachelor's Degrees in Industrial Chemistry (110/110 cum laude) at University of Catania, Italy. Thesis: "Sintesi di Nanoparticelle di Oro-Silicio mediante Ablazione Laser in Liquido" Supervisor: Prof. Orazio Puglisi.
- 2014:** Master's Degrees in Chemistry of Material (110/110 cum laude) at University of Catania, Italy. Thesis: "Up-conversion in dispositivi fotovoltaici: Sintesi sol-gel di film NaYF₄ come matrici ospiti di ioni lantanidi luminescenti" Supervisor: Prof. Graziella Malandrino.
- 2018:** Ph.D. in Material Science and Nanotechnology at University of Catania, Italy. Thesis: "Synthesis of hybrid metalorganic/inorganic systems and doped halide thin films for energy-conversion in photovoltaics" Supervisor: Prof. Graziella Malandrino; coordinator: Prof. Maria Grazia Grimaldi.

List of Papers on the PhD topics:

- Anna L. Pellegrino, P. Cortelletti, M. Pedroni, A. Speghini, G. Malandrino "Nanostructured CaF₂:Ln³⁺ (Ln³⁺=Yb³⁺/Er³⁺, Yb³⁺/Tm³⁺) thin films: MOCVD fabrication and their upconversion properties", Adv. Mater. Interfaces, **2017**, 4(18), 1700245/1-1700245-6.

- M. R. Catalano, Anna L. Pellegrino, P. Rossi, P. Paoli, P. Cortelletti, M. Pedroni, A. Speghini, G. Malandrino "Upconverting Er^{3+} , Yb^{3+} activated β - $NaYF_4$ thin films: a solution route using a novel sodium β -diketonate polyether adduct", *New Journal of Chemistry*, **2017**, 41, 4771-4775.
- A.L. Pellegrino, M. R. Catalano, P. Cortelletti, G. Lucchini, A. Speghini, G. Malandrino, "Novel sol-gel fabrication of Yb^{3+}/Tm^{3+} co-doped β - $NaYF_4$ thin films and investigation of their upconversion properties", *Photochemical & Photobiological Sciences*, **2018**, DOI 10.1039/C8PP00295A.
- Anna L. Pellegrino, C. Tudisco, G. G. Condorelli, A. Speghini, G. Malandrino, "Hybrid metalorganic-inorganic systems: Molecular Layer Deposition of luminescent europium complex on NiO thin", manuscript to be submitted.
- Anna L. Pellegrino, Adolfo Speghini, Graziella Malandrino, "Fabrication of Ln^{3+} doped binary and multicomponent fluoride thin films for energy-conversion in photovoltaics: pros and cons of MOCVD and sol-gel approaches", manuscript to be submitted.

List of other publications:

- H. Liu, S. Battiato, A. L. Pellegrino, P. Paoli, P. Rossi, C. Jimenez, G. Malandrino, D. Munoz-Rojas "Deposition of metallic silver coatings by Aerosol Assisted MOCVD using two new silver β -diketonate adduct metalorganic precursors", *Dalton Transactions*, **2017**, 46(33), 10986-10995.
- P. Ghamgosar, F. Rigoni, S. You, I. Dobryden, M. G. Kohan, A. L. Pellegrino, I. Concina, N. Almqvist, G. Malandrino, A. Vomiero, "ZnO-Cu₂O core-shell nanowires as stable and fast response photodetectors", *Nano Energy*, **2018**, 51, 308-316.
- C. Tudisco, A. L. Pellegrino, G. Malandrino, G.G. Condorelli, "Surface anchoring of bi-functional organic linkers on piezoelectric BiFeO₃ films and particles: Comparison between carboxylic and phosphonic tethering groups", *Surface & Coatings Technology*, **2018**, 343, 75-82.

Collaborations:

- Prof. Adolfo Speghini, Dipartimento di Biotecnologie, Università di Verona, Strada Le Grazie 15– Verona (Italy): Luminescence characterization.
- Prof.ssa Patrizia Rossi, Dip. di Ingegneria Industriale, Università degli Studi di Firenze, via Santa Marta 3 - Firenze (Italy): X-Ray single crystal structures.
- Prof. Guido G. Condorelli, Dr. Cristina Tudisco and Francesca Monforte, Dip. Scienze Chimiche, Università degli Studi di Catania, viale A. Doria 6 – Catania (Italy): XPS characterization and XRD - FE-SEM characterization of BFO films for Surface & Coatings Technology 2018, 343, 75-82.
- Dr. Carmen Jimenez, Laboratoire des Matériaux et du Génie Physique (LMGP) – Grenoble – France: Ag precursor synthesis for Dalton Transactions 2017, 46(33), 10986-10995.
- Prof. Alberto Vomiero, Department of Engineering Sciences and Mathematics, Division of Materials Science, University of Technology Luleå, Luleå – Sweden: MOCVD synthesis of Cu₂O for Nano Energy, 2018, 51, 308-316.

Conferences and workshop:

1. A.L. Pellegrino, C. Tudisco, G.G. Condorelli, P. Cortelletti, A. Speghini, G. Malandrino “MLD approach for hybrid metalorganic-inorganic systems: NiO thin films functionalized with a luminescent Eu complex monolayer”
SYMPOSIUM S, E MRS 2018 SPRING MEETING, 18-22 June 2018, Strasbourg – France. **Oral presentation.**
2. A.L. Pellegrino, P. Cortelletti, A. Speghini, G. Malandrino “Pros and cons of MOCVD and sol-gel approach in the synthesis of Ln³⁺ doped fluoride thin films for energy-conversion in photovoltaics”
SYMPOSIUM T, E MRS 2018 SPRING MEETING, 18-22 June 2018, Strasbourg – France. **Oral presentation.**
3. ENHANCE SUMMER SCHOOL, *Multidisciplinary Introductory School to Energy Harvesting Microsystems*, 16-18May 2018, Besançon – France.

4. A.L. Pellegrino, M.R. Catalano, P. Cortelletti, M. Pedroni, A. Speghini, G. Malandrino “*New sol gel approach for the synthesis of Ln³⁺ doped NaYF₄ thin films: analysis of phase stability and luminescence properties*”
MATERIA 2020- XI conv. naz. sulla scienza e tecn. dei materiali, 12-15 July 2017, Ischia (NA)– Italy. **Oral presentation.**
5. A.L. Pellegrino, P. Cortelletti, M. Pedroni, A. Speghini, G. Malandrino “*Ln³⁺ activated CaF₂ thin films: MOCVD synthesis and their energy conversion properties*”
euroCVD- balticALD 2017, 11-14 June 2017, Linkoping – Sweden. **Poster presentation.**
6. A.L. Pellegrino, M.R. Catalano, P. Cortelletti, M. Pedroni, A. Speghini, G. Malandrino “*MOCVD fabrication of luminescent nanostructured CaF₂ thin films*”
MATERIALS.IT 2016, 12-16 December 2016, Aci Castello (Catania)– Italy. **Poster presentation.**
7. R. Cairone, A.L. Pellegrino, G. Malandrino “*Novel complexes for the sol-gel synthesis of perovskite CsCaF₃ thin films*”
MATERIALS.IT 2016, 12-16 December 2016, Aci Castello (Catania)– Italy. **Poster presentation.**
8. A.L. Pellegrino, M.R. Catalano, P. Cortelletti, M. Pedroni, A. Speghini, G. Malandrino, “*Nanostructured NaYF₄:Yb³⁺, Er³⁺ thin films: preparation and upconverting properties*”
EUCHEMS2016 CHEMISTRY CONGRESS, 11-15 September 2016, Seville – Spain. **Poster presentation.**
9. A.L. Pellegrino, M. R. Catalano, P. Cortelletti, M. Pedroni, A. Speghini, G. Malandrino “*Fabrication of luminescent nanostructured NaYF₄ thin films through a new sol-gel approach*”
INTERNATIONAL CONFERENCE ON NANOSTRUCTURES AND NANOMATERIALS SELFASSEMBLY, 3-8 July 2016, Giardini Naxos – Italy. **Poster presentation.**
10. M. R. Catalano, A. L. Pellegrino, P. Cortelletti, A. Speghini, G. Malandrino “*Er³⁺/Yb³⁺ doped hexagonal NaYF₄ thin films: structural, morphological and functional characterization*”

SYMPOSIUM C, E-MRS 2015 SPRING MEETING 11-15 May 2015, Lille Grand Palais – France. *Poster presentation.*

Co-tutor activities:

CO-TUTOR with Prof. G. Malandrino for Bachelor's Degrees in Industrial Chemistry:

- *"Film fluoruro di calcio drogati itterbio e tulio: studio del processo MOCVD"*, Valentina Petralia, February - July 2016;
- *"Studio di processi MOCVD per deposizione di film di ossido di rame (I)"*, Vincenza Avellina, March-June 2016;
- *"Ottimizzazione del processo sol-gel di film fluoruro di calcio drogati con europio per down-conversion"*, Giuseppa Cristaldi, June-September 2016;
- *"Sintesi di sistemi multistrato fluoruro di calcio drogati con Er e Yb per upconversion"*, Silvestro Lucio Treccarichi, June -September 2016.

CO-TUTOR with Prof. G. Malandrino for Bachelor's Degrees in Chemistry:

- *"Deposizione chimica da fase vapore di film fluoruro di calcio per downconversion"*, Erica Leanza, November 2015-March 2016;
- *"Sintesi e caratterizzazione di complessi eteronucleari contenenti zinco e lantanidi"*, Salvatore Sambataro, April- July 2016;
- *"Sintesi dei complessi Li(hfa)glyme: effetto delle lunghezze del polietere sulle proprietà dei complessi"*, Francesco Palmeri, June- September 2016;
- *"Deposizione di film di CaF₂ drogati con itterbio, tulio, ed erbio"*, Salvo La Manna, March - July 2017;
- *"Deposizione sistemi ibridi inorganico–metallorganico: funzionalizzazione di film NiO con complesso luminescente di Eu"*, Fabiana Maria Pennisi, April - September 2017;
- *"Deposizione MOCVD di film NaYF₄: ottimizzazione dei parametri di processo per l'ottenimento della fase esagonale"*, Sebastiano Greco, September 2017 -April 2018;
- *"Sintesi di addotti β -dichetonati polietere Li-Y per la deposizione di film LiYF₄"*, Ilenia Scardino, September 2017 -April 2018;

- *“Down Conversion in dispositivi fotovoltaici: sintesi sol-gel di NaGdF₄”*, Sara Bonanno March 2017 - September 2018;

- *“Sintesi MOCVD di film misti Fe₂O₃-Cr₂O₃: ottimizzazione del processo e studio delle proprietà ottiche”*, Alfio Enrico Romano, November 2017- July 2018.

CO-TUTOR with Prof. G. Malandrino for Master’s Degrees in Organic Chemistry and Bio organics:

- *“Sintesi e caratterizzazione di nuovi complessi di cesio Cs(hfa)polietere, loro applicazione per la preparazione di fasi fluoruro”*, Carmen Tamaio, November 2015-July 2016.

CO-TUTOR with Prof. G. Malandrino for Master’s Degrees in Material Chemistry:

- *“Perovskiti alogenuri per applicazioni in optoelettronica e fotovoltaico: dalla sintesi di nuovi precursori alla deposizione di film tramite sol-gel”*, Roberto Cairone, January -November 2016;

- *“Nucleazione, crescita e trasformazioni strutturali di cristalli di perovskite inorganica CsPbBr₃”*, Giovanni Giuffrida, June 2017- July 2018;

- *“Metal-Organic Framework di Ittrio con leganti tritopici: effetto della natura del legante sulle loro proprietà”*, Claudia Buscemi, November 2017 -July 2018;

- *“Sistemi ibridi inorganico–metallorganico: molecular layer deposition per la funzionalizzazione di film NiO con complesso luminescente di Eu”*, Maria Rosa Raciti, October 2017-September 2018;

- *“Sintesi di un nuovo precursore bimetallico potassio-ittrio e ottimizzazione del processo MOCVD per l’ottenimento di film KYF₄”*, Andrea Annese, April- September 2018;

- *“Sintesi MOCVD di film sottili di ossido di manganese: ottimizzazione del processo e studio del processo di crescita”*, Fabiana Sgrò, May – September 2018.